ELECTROMAGNETIC BACKSCATTERING STUDIES OF NONLINEAR OCEAN SURFACES

DISSERTATION

Presented in Partial Fulfillment of the Requirements for

the Degree Doctor of Philosophy in the

Graduate School of The Ohio State University

By

Guangdong Pan, B.E., M.S.

* * * * *

The Ohio State University

2008

Dissertation Committee:

Prof. Joel T. Johnson, Adviser

Prof. Robert J. Burkholder

Prof. Roberto G. Rojas-Teran

Approved by

Adviser

Graduate Program in
Electrical and Computer
Engineering

ABSTRACT

The spatial/time spectrum of short sea waves and radar observed signals are locally modulated by the presence of longer waves or currents. There are two different modulations: tilt modulation and hydrodynamic modulation. Variations in the short sea waves spectrum are described by the "hydrodynamic modulation transfer function" (HMTF). The nonlinear interaction between short sea waves and longer waves makes such modulation. Variations of radar signals are described by the "radar modulation transfer function" (RMTF). In this study, new numerical methods based on numerical nonlinear hydrodynamics and computational electromagnetics are developed to examine modulation in sea surface scattering and to examine the accuracy of existing analytical models.

Electromagnetic scattering from sea surface at low-grazing-angles (LGA) is studied by comparing analytical scattering models. The two-scale model (TSM) is found to yield the most reasonable performance among these models. Ocean surface profile retrieval based on the TSM is also shown to have an acceptable accuracy.

Numerical methods are developed to calculate the HMTF, and RMTF by use of the fast nonlinear hydrodynamics, and by use of the fast computational electromagnetics techniques. These techniques allow us to study the scattering from a stochastic "Pierson-Moskowitz" like surface with Monte-Carlo simulation.

HMTF values obtained from the simulations are compared to those from a first order wave action solution, and found to be in reasonable agreement, although differences on the order of 10% are observed. A numerical evaluation of long wave effects on the short wave dispersion relation is also provided.

The numerical method provides a quantitative way to examine the "third- scale" effect in the two-scale model. The results demonstrate that the intermediate waves influence the RMTF and are modulated by longer waves. This effect explains the RHMTF polarization dependence. Numerical results of the "third-scale" effect match well with empirical and analytical results.

A new analytical Doppler formula is derived from the nonlinear hydrodynamics. The solution is validated by numerical solutions and supported by radar Doppler simulation. Ocean surface profile retrieval based on Doppler information is shown to have a very good accuracy.

To my family

ACKNOWLEDGMENTS

First and foremost, I would like to thank my advisor, Professor Joel T. Johnson, for his immeasurable guidance, encouragement, and support through this Ph.D study. He is an excellent researcher and keeps high standards for himself and his students. I am very grateful to his insights and suggestions that helped me to shape my research skills. Without him, this work could never be completed.

I am also very grateful to the other Ph.D committee members, Dr. Robert Burkholder, and Prof. Roberto Rojas-Teran. I would like to thank them for serving on my candidacy and dissertation examine committees and providing valuable suggestions and other efforts throughout my dissertation study. I would also thank Prof. Jinfa Lee, Prof. Randolph Moses, and Prof. Ashok Krishnamurthy for serving on my qualify and candidacy committees. I feel extremely fortunate to have them on my committee.

I would like to sincerely thank Prof. Gregory Baker of The Ohio State Department of Mathematics. I learn a lot hydrodynamics from him in our group meeting. I also learned a lot applied mathematics from his excellent courses. I would also like to give special thanks Dr. David Lyzenga of the University of Michigan and Prof. Woo-Young Choi of the New Jersey Institute of Technology, for their helpful discussion and for providing their report of the current modulation.

Special thanks to my colleagues, Bo He, Yijun Zhou, Demir Metin, Noppasin Niamsuwan, Baris Gűner, and Prophum Naenna for their valuable discussions and their friendship.

As always, the greatest debt owes to my family, specially my mother and my wife for their support and love.

VITA

February 15, 1969	Born - Anqing, China
1992	B.E. Chengdu University of Technology, China
1992-1995	Engineer, Bureau of Geology and Mineral Resources Exploration, Anhui Province, China
1998	M.S. Cartography and Remote Sensing, Chinese Academy of Sciences, China
1998-2001	Research Associate, Research Assistant Professor since 2000, Institute of Remote Sensing Applications, Chinese Academy of Sciences, China
2003	M.S. Electrical Engineering, University of Nebraska-Lincoln, USA
2003-present	Graduate Research Associate, The Ohio State University, USA

PUBLICATIONS

Research Publications

G. D. Pan and J. T. Johnson. Studies of ocean wave-radar modulation mechanisms in sea backscattering: Inclusion of the third-scale effect. In preparation

G. D. Pan and J. T. Johnson. A numerical study of the modulation mechanisms in sea backscattering. *URSI2007*, Ottawa, Canada, July 22-26, 2007.

G. D. Pan and J. T. Johnson. A numerical study of the modulation of short sea waves by longer waves. *IEEE Trans. Geosci. Remote Sens.*, 44(10):2880–2889, 2006.

G. D. Pan, R. Burkholder, J. T. Johnson, T. Toporkiv, and M. Sletten. Studies of ocean surface retrieval from simulated LGA radar. In *Proceedings of IEEE IGARSS06*, pages 1335–1337, Denver, USA, July 31-Aug. 4, 2006.

G. D. Pan and J. T. Johnson. A numerical study of the modulation of short sea waves by longer waves. In *Proceedings of IEEE IGARSS06*, pages 1304–1307, Denver, USA, July 31-Aug. 4, 2006.

FIELDS OF STUDY

Major Field: Electrical and Computer Engineering

Studies in Electromagnetics

TABLE OF CONTENTS

Page

LIST OF TABLES

LIST OF FIGURES

Figure **Page**

CHAPTER 1

INTRODUCTION

1.1 Background and motivation

The ocean occupies over 70 percent of the total Earth surface, and it plays an important role in many areas. Remote sensing is an important technique to monitor the ocean surface parameters. In particular, microwave remote sensing techniques play a key function to detect ocean surface parameters, due to the "transparency" of clouds to microwaves. Both active microwave remote sensing instruments (radar, scatterometer, altimeter) and passive instruments (radiometer) have been widely utilized to monitor the ocean surface.

To better understand and interpret observed signals, we need to develop electromagnetic (EM) models. The EM scattering from ocean surfaces involves both electromagnetics and hydrodynamics. Some scattering phenomena are highly dependent on the latter, for example, sea surface radar cross section (RCS) variations over time/space, observed Doppler frequency properties, and polarization abnormalities of RCS and Doppler, especially at low grazing angles (LGA) of observation. The purpose of this thesis is to investigate scattering from ocean surfaces by combining both hydrodynamics and electromagnetics.

In the past two decades, electromagnetic scattering at LGA has been of interest in the ocean remote sensing community. Numerous experiments have been conducted to investigate how to quantitatively interpret scattering signals [1, 2, 3, 4, 5, 6, 7]. Several phenomena that are difficult to explain by classical scattering models [8, 9] have been encountered. The small slope approximation (SSA) is a promising scattering method [10, 11] along with its extension, the nonlocal SSA (NLSSA) [12], which attempts to include multiple scattering. Although the original SSA has limitations in modeling LGA scattering [13], some studies have demonstrated that the SSA and NLSSA have good accuracy compared with the exact integral equation solution [14]. In addition, Kim et al's study [15] further supports that SSA and NLSSA capture multiple scattering at LGA. Therefore, a further study of RCS by comparison among those analytical scattering models is of interest in this thesis.

Predicting polarized RCS and Doppler frequency properties at LGA involve both hydrodynamics and electromagnetics. The hydrodynamics relates to surface dynamics, which produce scattering abnormalities [1, 5, 7, 16, 17, 18]. Furthermore, "bound waves" may contribute to abnormal Doppler frequencies [19]. Non-Bragg scattering mechanisms may also make appreciable contributions at LGA, for example, multiple scattering [4, 17, 20], and shadowing [8, 21]. Abnormal Doppler behaviors have been captured somewhat by Monte-Carlo simulations without considering wave breaking [22, 23], although most studies demonstrate that wave breaking is a possible major mechanism for the abnormality of polarization intensity ratio and polarization Doppler frequency [1, 16, 5, 17, 18, 7]. Overall, these results indicate that hydrodynamics is very important in ocean scattering. For example, bounded waves are related to wave dynamics, i.e., the nonlinear hydrodynamics. A key influence is that

of "long" ocean waves on short Bragg waves, generally described by the hydrodynamic modulation transfer function (HMTF).

Existing models for the HMTF are based on asymptotic approaches [24, 25, 26, 27, 28], whose accuracy had never been numerically evaluated. Efficient numerical methods in hydrodynamics allow us to simulate nonlinear hydrodynamics [29, 30], and have been used in radar remote sensing for prediction of Doppler frequency with different incidence angles [31], even at LGA [22, 23, 32]. This progress enables us to study the HMTF using numerical hydrodynamic codes, and further to study the radar modulation transfer function (RMTF) with efficient electromagnetic codes as well.

Numerous scatterometer/radar ocean experiments have indicated that the radar cross section (RCS) of ocean surfaces is modulated by the presence of the underlying long waves or currents [33, 34, 24, 35, 36, 37]. Such modulation is described by the RMTF, including the radar HMTF (RHMTF) and tilt modulation transfer function (TMTF) [38, 39, 24]. The latter is simply due to the local tilted geometry effect of the illuminated facet, which changes the local incidence angle. The RHMTF is the radar measurement of the HMTF. Although it is common to assume that the RHMTF and HMTF are the same, the HMTF is in fact the modulation due to hydrodynamics, and the RHMTF involves both hydrodynamics and electromagnetics. It was reported that the RHMTF of HH polarization is greater than that of VV polarization [40, 24, 36]. These observations are contrary to those of [38], since the observed RHMTF depends on polarization. Furthermore, it has been reported by simulations that the RHMTF also depends on incidence angles and frequencies [41]. In particular, it was recognized that the intermediate waves contribute to this dependency [42, 40, 19]. These observed

discrepancies motivate us to quantitatively understand the RHMTF, its relationship to the HMTF, and a "three-scale" (long waves, intermediate waves, and short Bragg waves) influence on the RMTF.

Long-short sea wave interactions also influence the ocean Doppler spectrum. The ocean Doppler bandwidth depends on such modulation, as determined by the long wave slope [42]. This modulation is produced by nonlinear hydrodynamics, and increases the Doppler bandwidth [31, 22]. Most existing Doppler studies are based either on measurements or on numerical simulations [31, 22, 23, 43]. No analytical studies based on the nonlinear hydrodynamics have been reported. This motivates an analytically modulated Doppler analysis based on nonlinear hydrodynamics.

The ocean surface profile retrieval is one application example of these results. Recently, researchers have achieved reasonable retrieval results from data acquired from an X-band radar at LGA [44, 45]. The HMTF effect was neglected in these retrieval processes. In these studies, it was assumed that the tilted Bragg scattering mechanism (i.e. TMTF) dominates at LGA. In fact, electromagnetic scattering at LGA is complicated by non-Bragg scattering (for example, multiple scattering, and shadowing effects). A numerical method - the method of moments (MOM) [46, 47] has been applied to predict scattering at LGA. It does not have an simple analytical formula. Therefore, it is of interest to study an analytically simple physical scattering model at LGA that is also analytically invertible.

1.2 Organization

The remainder of this dissertation is organized as follows.

In Chapter 2, several analytical electromagnetic scattering models (SPM, KA, SSA, NLSSA, TSM) are examined at LGA. We further explore the scattering mechanisms based on different iterations from the integral equation solution, i.e., MOM. It turns out that the two-scale model (TSM), while exhibiting apparently errors, is the most reasonable approximate scattering model at LGA, and that at least one forward iteration and one backward iteration are necessary for computing backscattering at LGA.

Ocean surface profile retrievals from the LGA radar data using the physical scattering model (TSM) is studied in Chapter 3. Due to its mathematical simplicity, only the HH polarization data are used. The result indicates that the physical model-based retrieval is acceptable at LGA. The influence to the retrieval accuracy of range resolution, incidence angles, radar frequency, and ocean roughness are further discussed.

In Chapter 4, a method for providing direct insight into the hydrodynamic modulation of short sea waves by longer waves is described, through the use of numerical non-linear hydrodynamic codes for sea surface evolution. The codes applied are reviewed, and a Monte Carlo simulation process based on a stochastic spectrum of short waves propagating over a single deterministic long wave is described, including the data analysis techniques developed to extract a numerical HMTF from the simulated surfaces. HMTF values obtained from the simulations are compared to those from a first order wave action solution and are found to be in reasonable agreement, although differences on the order of 10% are observed. A numerical evaluation of long wave effects on the short wave dispersion relation is also provided. In addition, a numerical study of HMTF for currents is presented in Appendix A, and our numerical HMTF results match very well with analytical predictions.

A method to investigate radar modulation mechanisms is described in Chapter 5, through use of numerical nonlinear hydrodynamic codes and the fast numerical electromagnetic integral equation method for a perfectly conducting time-evolving sea surface. This surface is generated by a stochastic spectrum of short waves propagating over a single deterministic long wave. A narrow Gaussian-like tapered incident wave is chosen to calculate the local scattering. Polarized RCS datasets from the long and short waves surface and short waves only surface are used to numerically extract the RMTF and RHMTF, respectively. The mean square slope of the intermediate waves is also studied. Our numerical results demonstrate that the numerical polarized RTMTFs match with those predicted by the TSM, and the slope of intermediate waves performs a linear contribution to the MTF mechanism as that of the long wave slope. The third-scale modulation is further investigated and validated with a stochastic "two-scale" model.

An analytical formula for the modulation of short waves based on the "Watson-West" (WW) equations [29] is derived in Chapter 6. Firstly, a simplified ordinary differential equation system is obtained after some mathematical manipulations. Then, the analytical solution to this system is presented, which gives the analytical form of the complex amplitude of the modulated short waves. Further Doppler analysis based on this analytical solution is discussed. Finally, some comparisons between this simplified method and the original WW method are presented. In particular, the radar Doppler from the simplified WW surfaces are shown. Our results demonstrate that the simplified method works well under small long wave steepness.

Chapter 7 concludes this thesis with a discussion of major contributions and future work.

CHAPTER 2

STUDIES OF LOW GRAZING BACKSCATTERING FROM OCEAN SURFACES

2.1 Introduction

Recently, the scattering at LGA has been of great interest to the ocean microwave remote sensing community [1, 2, 3, 4, 5, 6, 7]. Several scattering phenomena that are difficult to explain by classical scattering models [8, 9] have been encountered. This motivates us to study some classical scattering models further to find what causes the difficulty and what the main scattering mechanisms at LGA are. For this reason, the study of the range-resolved RCS from ocean-like controlled rough surfaces is conducted here. In order to further quantitatively understand the physical mechanisms between the range-resolved RCS and the local slope, both physical and numerical scattering models are also studied here.

The remainder of this chapter is organized as follows. Electromagnetic backscattering from a given deterministic rough surface is modeled by both analytical and numerical methods in Section 2.2. Several well-known analytical methods are introduced in Section 2.2.1. The approximated numerical solutions are described in Section 2.2.2, and the range-resolved RCS comparison among all selected models are

discussed and analyzed in Section 2.3. Finally, a brief summary is given in Section 2.4.

2.2 Methodology

The study described in this chapter is based on one-dimensional (1-D) simulations of radar backscattering from ocean-like surfaces [22, 23]. The surface profiles are produced linearly and nonlinearly using a "Pierson-Moskowitz" (PM) spectrum.

Electromagnetic backscattering from a 1-D random, rough, perfectly electrically conducting (PEC) surface $f(x)$ is illustrated in Figure 2.1, where the incidence and scattering wave directions are denoted by $\hat{k}_i$ and $\hat{k}_s$, and associated angles are denoted by θ_i and θ_s, respectively.

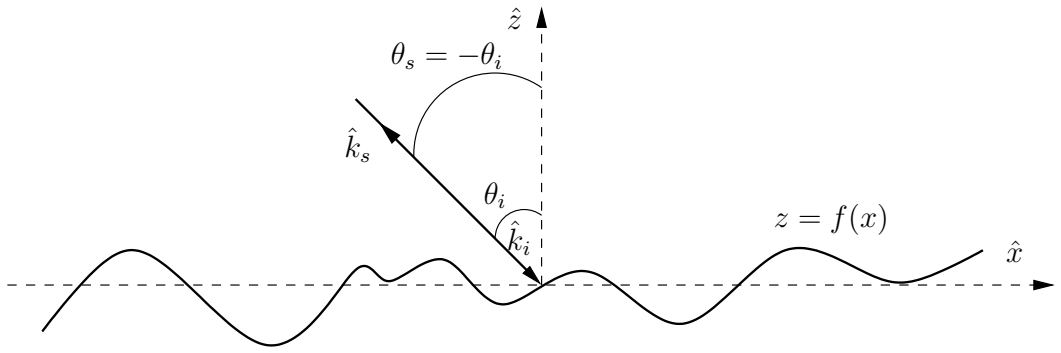

Figure 2.1: An illustration of scattering from a one-dimensional PEC random rough surface

The backscattering field at a given frequency is an integration over the entire illuminated surface. In order to resolve the local property of the entire surface, we need to know the local scattering information. If the entire surface is discretized into N elements, we need N distinct backscattering fields to resolve the information of

those N elements. A step-frequency radar provides a practical way to recognize the local surface characteristics [48]. In this study, the step-frequency radar technique is applied to generate the local scattering fields, and used to determine the range-resolved RCS.

The scattering from the rough surface $f(x)$ can be solved either by analytical or numerical methods. Several analytical approaches based on the Rayleigh hypothesis will be presented and applied to analyze the range-resolved RCS. Several numerical iteration techniques are also discussed based on the integral equation formulation of electromagnetic backscattering.

2.2.1 Analytical scattering models

Based on the Rayleigh hypothesis [10], the scattering fields consist of the outgoing propagation waves. Mathematically, the scattering field $\phi^s(k, \mathbf{r})$ at the far field $\mathbf{r}$ is written by

$$\phi^s(k, \mathbf{r}) = \int dk_{sx} T(k_{sx}, k_{ix}) e^{i\mathbf{k}_s \cdot \mathbf{r}}, \tag{2.1}$$

where $k_{ix} = k\sin(\theta_i)$, $k_s = k\sin(\theta_s)$, and T is called the spectral scattering coefficient. In the far field, equation (2.1) can be further approximated by a stationary phase approach as

$$\phi^s(k, \mathbf{r}) = \sqrt{\frac{2\pi}{kr_0}} e^{i(\kappa r_0 - \pi/4)} \frac{1}{2\pi} k\cos(\theta_i) \int dx \Phi e^{i2k(\sin(\theta_i)x - \cos(\theta_i)z)}, \tag{2.2}$$

where Φ is the expansion coefficient. It can be expanded as [11]

$$\Phi = \Phi^0 + \int dK e^{iKx} \Phi^1(K) F(K) + ... \tag{2.3}$$

where Φ^0 and Φ^1 denote the first order and the second order kernel, respectively, and $F(K)$ denotes the Fourier coefficient of the surface $f(x)$. Table 2.1 shows the

polarization Φ^0 for three different analytical models, including the first order small perturbation model (SPM-1 or SPM) [49], the first order Kirchhoff approach (KA-1 or KA) [49], and the first order small slope approach (SSA-1) [10, 11].

Models	HH	VV
SPM-1	$2ik\cos(\theta_i)f(x)$	$-2ik\frac{1+\sin^2(\theta_i)}{\cos(\theta_i)}f(x)$
KA-1	$-i[1+f'(x)\tan(\theta_i)]$	$-i[1-f'(x)\tan(\theta_i)]$
SSA-1	-1	$\frac{1+\sin^2(\theta_i)}{\cos^2(\theta_i)}$

Table 2.1: Φ_0 in three analytical models (SPM-1, KA-1, SSA-1)

In this work, scattering predictions of the SPM, KA, SSA, NLSSA, and TSM are considered. The backscattering fields given by the SPM are different from those represented by equation (2.1) for both polarizations. The difference is that there is no $z = f(x)$ component in the exponential part for the exact SPM. Due to $k_{iz}f(x) << 1$, we add this exponential part $e^{ik_{iz}f(x)}$ to the SPM for convenience of the comparison between the SPM and the SSA. In reality, the ocean surface consists of multiple scales. The SPM-1 can be applied only to very smooth (with respect to the electromagnetic wavelength) surfaces. The well-known TSM [50, 51] has been successfully applied in the ocean remote sensing community over several decades. The TSM is similar to a local SPM in treating both incident and scattering angles with respect to local normal directions. Following is the TSM treatment used in this study:

- Suppose that the entire surface $f(x)$ is discretized equally along the horizontal direction $\hat{x}$ with N elements, and it is divided into M sub-surfaces with the total element number Nw.
- Each adjacent sub-surface has overlap elements Nw/4.
- The length of total Nw elements is chosen as about 8 electromagnetic wavelengths.
- The local slope of each sub-surface is averaged over all points (or elements) of this sub-surface. Prior to averaging the local scopes of all points, a low-pass filter is used to filter out those high oscillation frequency components. The cutoff frequency is normally chosen between $[\frac{k}{3}, \frac{k}{2}]$ [52]. It is set as $\frac{k}{3}$ in this study.
- Once the local slope is obtained, the local incidence angle θ_{il} can be easily determined.
- The local Bragg-Fourier spectral coefficient of the i^{th} sub-surface, $F_i(k_B)$, is obtained from the zero-padded windowed surface (with an element size N), where $k_B = -2k\sin(\theta_{il}(i))$ is the Bragg wavenumber of this sub-surface.
- The horizontal coordinate of each sub-surface center, x_c, is chosen as its geometrical center, and its vertical coordinate z_c is chosen as its elevation average.

Finally, the polarized backscattering fields given by the TSM are written as

$$\phi_p^s = \frac{A}{M}\sum_{i=1}^{M} C_{pp}(i)F_i(k_B)P(i)W \tag{2.4}$$

where $A = -4j\pi k^{1.5}$, $P(i) = e^{i2k(\sin(\theta_i)x_c(i)-\cos(\theta_i)z_c(i))}$, C_{pp} is the polarization coefficient with $C_{HH} = \cos^2(\theta_{il}(i))$ and $C_{VV} = 1 + \sin^2(\theta_{il}(i))$, and W is a Gaussian tapering window function over the entire surface [53]. For each sub-surface, the values of W

in equation (2.4) will be chosen as the only M local values corresponding to its local M points.

The second order SSA (SSA-2) is given by [11, 54]

$$\Phi_{HH}^{(1)}(K_1) = -\frac{j}{2}[\sqrt{k^2-(k_{ix}+K_1)^2}+\sqrt{k^2-(k_{sx}-K_1)^2}+(k_{iz}-k_{sz})], \tag{2.5}$$

$$\Phi_{VV}^{(1)}(K_1) = -\frac{j}{2}[B_2(k_{sx}-K_1)+B_2(k_{ix}+K_1)+(k_{iz}-k_{sz})\Phi_0], \tag{2.6}$$

where $B_2(K_1) = \frac{1}{k_{iz}k_{sz}\sqrt{k^2-K_1^2}}(k^2-k_{ix}K_1)(k^2-k_{sx}K_1)$.

The first order NLSSA is given in [12], and is close to a combination of SSA-1 and SSA-2.

2.2.2 Numerical scattering models

The integral equation starts from the Huygens' principle, and the total field $\phi(\mathbf{r}', t)$ above the surface point $\mathbf{r}$ can be written as [49]

$$\phi(\mathbf{r}') = \phi^{inc}(\mathbf{r}') + \int_\Gamma ds[\phi(\mathbf{r})\hat{n}\cdot\nabla g(\mathbf{r},\mathbf{r}') - g(\mathbf{r},\mathbf{r}')\hat{n}\cdot\nabla\phi(\mathbf{r})], \tag{2.7}$$

where ϕ^{inc} is the incident field, Γ denotes the illuminated rough surface, $\hat{n}$ is the surface normal vector toward $\hat{z}$, and $g(\mathbf{r},\mathbf{r}') = \frac{i}{4}H_0^{(1)}(k|\mathbf{r}-\mathbf{r}'|)$ is the Green's function with time dependence $e^{-j\omega t}$ suppressed. $H_0^{(1)}$ is the zeroth order Hankel function of the first kind. Equation (2.7) can be further simplified with the associated boundary conditions and will be used to derive the scattering field under the Kirchhoff approach (KA) in this chapter. Mathematically, the scattering field $\phi^s = \phi - \phi^{inc}$.

The collocation method is a popular and effective numerical method to solve the integral equation (2.7). In order to perform iterative solving methods, equation (2.7) can be written with a generalized form as [46, 55]

$$\mathbf{J}(x) = \mathbf{J}^i(x) + \int_{-\infty}^{x} dx' G(x',x)\mathbf{J}(x') + \int_{x}^{\infty} dx' G(x',x)\mathbf{J}(x'), \tag{2.8}$$

where $G(x', x)$ is the generalized Green function which can be derived from equation (2.7) given the boundary condition (BC), and $\mathbf{J}$ is the generalized surface-induced current. The $G(x', x)$ is written by [56]

$$G(x', x) = \begin{cases} -\frac{ik}{4}\frac{H_1^{(1)}(kd)}{d}\sqrt{\frac{1+f'(x')^2}{1+f'(x)^2}}[-f'(x)(x-x') + f(x) - f(x')], & \text{for HH pol.} \\ \frac{ik}{4}\frac{H_1^{(1)}(kd)}{d}[-f'(x')(x'-x) + f(x') - f(x)], & \text{for VV pol.,} \end{cases}$$

where $d = \sqrt{(x-x')^2 + (f(x) - f(x'))^2}$ and $H_1^{(1)}$ is the first order Hankel function of the first kind. In particular, the integral equation given by the original equation (2.7) associated with the Dirichlet boundary condition (the HH polarization) is a Fredholm integral equation of the first kind. It can be converted into a Fredholm integral equation of the second kind after a transformation [56]. The purpose of this transformation is to achieve a better matrix condition number to accelerate the iterative convergence rate. Thus, equation (2.8) can be applied for both polarizations. It can be further rewritten as an operator form

$$\mathbf{J} = \mathbf{J}^i + \mathbf{L}\mathbf{J} + \mathbf{U}\mathbf{J}, \tag{2.9}$$

where $\mathbf{L}$ is a lower triangle matrix, and $\mathbf{U}$ is an upper triangle matrix. Equation (2.9) can be solved by a method called "Forward-Backward" (FB) [55] or a method called the method of multiple interaction (MOMI) [46]. Below are six steps to perform the MOMI:

(1) $\mathbf{J}_1 = (\mathbf{I} - \mathbf{L})^{-1}\mathbf{J}_i$;

(2) $\mathbf{J}_2 = (\mathbf{I} - \mathbf{U})^{-1}\mathbf{J}_1 - \mathbf{J}_1$;

(3) $\mathbf{J}_3 = (\mathbf{I} - \mathbf{L})^{-1}\mathbf{J}_2 - \mathbf{J}_2$;

(4) set $\mathbf{J}_3 = \mathbf{J}_1$;

(5) repeat (2)-(4) steps until desired accuracy;

(6) $\mathbf{J} = (\mathbf{I} - \mathbf{U})^{-1}\mathbf{J}_1$,

where $\mathbf{I}$ is the identity matrix. The operators $\mathbf{L}$ and $\mathbf{U}$ can be effectively implemented by the spectral acceleration (SA) method [47, 57]. With this acceleration technique, the integration limit is decomposed with two parts: the strong part and the weak part, and the SA technique only applies to the weak part.

The whole six iteration steps above are denoted by *MOM* here. Several variations based on the above iterations are listed as follows:

- if iteration involves only two steps: step (1) and (6), it is called *Born* iteration;
- if iteration involves only step (1), it is called *Forward* iteration;
- if iteration involves only step (1) and $\mathbf{L} = 0$, it is called *Diagonal* iteration;
- if iteration involves whole six steps and zero weak-weak terms [47] of $\mathbf{L}$ and $\mathbf{U}$, it is called *Strong* iteration.

If equation (2.9) is rewritten as

$$\mathbf{J} = (\mathbf{I} - \mathbf{L} - \mathbf{U})^{-1}\mathbf{J}_i \approx (\mathbf{I} + \mathbf{L} + \mathbf{U})\mathbf{J}_i. \tag{2.10}$$

This iteration is called the modified second order Kirchhoff approach (EKA-2) [58].

2.2.3 Range-resolved RCS

A finite surface consists of N distinct adjacent scatterers. It is obvious that the backscattering field with a specific frequency (or k) is an integration over the entire illumination surface from either equation (2.1) or equation (2.7), i.e., it is an average over each scatterer. Therefore, each individual scatterer can not be identified from a single frequency scattering field. The sweep radar technique provides a practical way to distinguish each scatterer property [48]. Assuming the central radar frequency f_0 and a discrete equally increment frequency Δf with a total bandwidth B (B=NΔf),

we compute the backscattering field for both polarizations at each frequency. Then, we have a dataset of backscattering fields varying over frequencies. Through a scattering field transformation from the frequency domain to the spatial domain, the range-resolved backscattering field for both polarizations (or its modulus square - RCS) can be obtained. The down-range resolution Δr satisfies

$$\Delta r = \frac{c}{2B}, \tag{2.11}$$

where c is the speed of an electromagnetic wave in vacuum.

Most analytical scattering models predict accurate RCS for both polarizations at near normal incidence angles to moderate incidence angles. Figure 2.2 shows RCS predicted by SSA, EKA-2 and MOM. This figure shows good accuracies of these three models at near normal incidence angles to moderate incidence angles. However, as mentioned previously, the RCS presented in Figure 2.2 is an average over the entire surface, which means that it cannot be used to identify details of the local surface. Therefore, the range-resolved RCS is adapted to detect the local property. Since the down-range resolution is related to the incidence angle, the small incidence angle θ_i has large (or poor) horizontal range resolution Δx (see Figure 2.3) . Therefore, the polarized range-resolved RCS given by both analytical and numerical methods is only investigated at two different incidence angles: a moderate angle (50^0) and a low grazing angle (LGA) (80^0).

2.3 Results and discussions

Three deterministic (with one specific realization) linear "Pierson-Moskowitz" ocean-like surfaces are studied. The smooth one has a band-limited wavenumber $[20, 200]$ rad/m, and two rough surfaces have a band-limited wavenumber $[1, 300]$

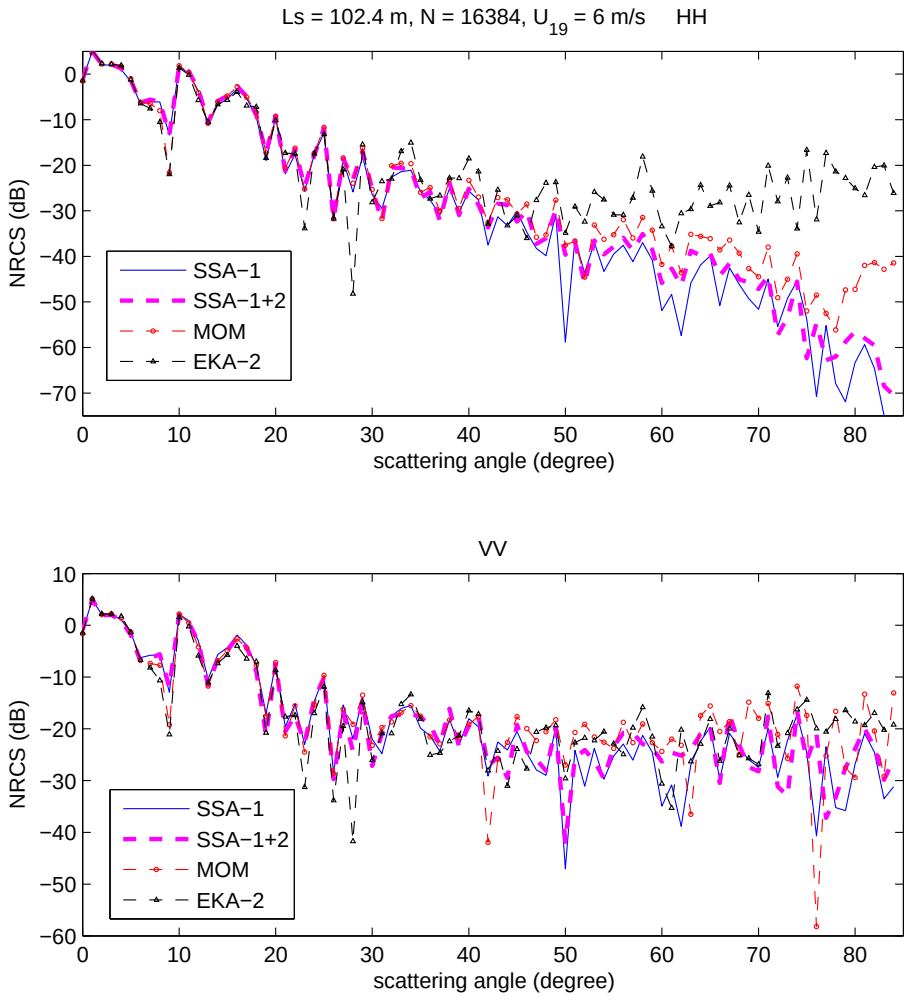

Figure 2.2: Backscattering coefficients vs. scattering angles among SSA-1, SSA-1+2, EKA-2, MOM [Simulated parameters: PM surface band-limited wavenumber [1,200] rad/m, the wind speed at 19.5 m is 6 m/s, the surface length is 102.4 m with discretization number 16384, and the radar frequency is 3 GHz]

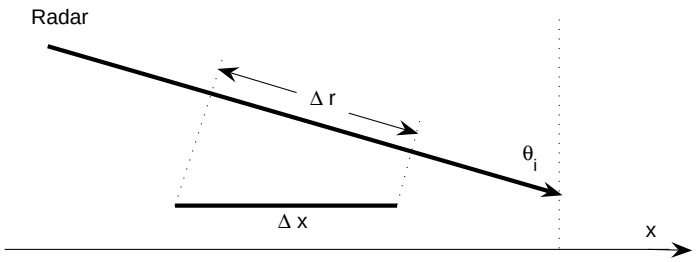

Figure 2.3: The illustration between down range resolution Δr and horizontal range resolution Δx

rad/m with 19.5 m wind speed 6 m/s and 10 m/s, respectively. In addition, a non-linear surface generated by [30] with 19.5 m wind speed 5 m/s is studied. All those surfaces are shown in Figure 2.4, where the η denotes the surface height. From top to bottom in Figure 2.4, the four surfaces are called *smooth, PM-6, PM-10*, and *Creamer*, respectively, in this study.

The length of the *Creamer* surface is 122.88 m with a spatial discretization number 65536, and the others are 102.4 m with a spatial discretization number 16384. The sweep radar central frequency at 10 GHz (X-band) with 256 frequency steps and a bandwidth 312.5 MHz is applied to the *Creamer* surface. Another sweep radar at the central frequency 3 GHz (S-band) with 256 (or 128 for a different iteration comparison) frequency steps and a bandwidth 375 MHz is applied to the other three surfaces. Such discretizations yield about 16 points per electromagnetic wavelength both for the *Creamer* surface at X-band and for the others at S-band.

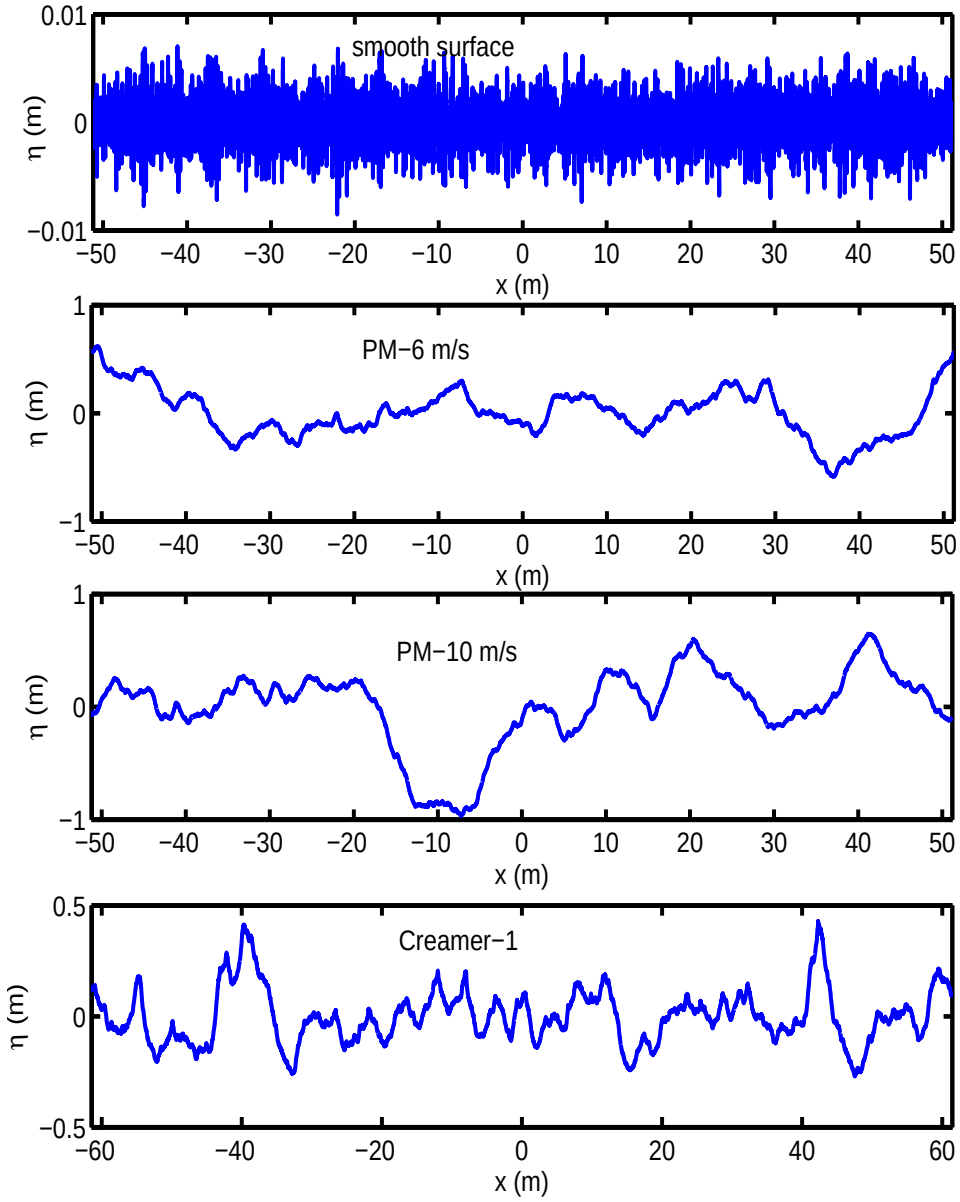

Figure 2.4: Four simulated surfaces with different roughness and linearity in this LGA scattering study

In order to minimize the finite surface truncation effect, a tapered plane incidence is used [53] in all analytical models, and a similar tapered wave [59] is used in all numerical methods. The difference in the backscattering field due to these two tapering functions is negligible. Therefore, there is no additional correction between those analytical solutions and the MOM results. Due to the Gaussian tapering, only the central region (half of the surface length) of the entire surface is shown in the following comparison results in Section 2.3.1 and Section 2.3.2. The down (or slant) range resolution Δr is shown at the bottom of each figure.

For each specific surface, the polarized backscattering fields are computed at each discretized sweep frequency by the MOM. Then, the Discrete Fourier transform (implemented by FFT) is performed to compute the range-resolved RCS from those backscattering field data in the frequency domain. Prior to the FFT computation, a Gaussian windowed function is multiplied with the backscattering data in order to suppress the range sidelobe effect.

2.3.1 Comparisons of analytical models

Smooth surface

The polarized range-resolved RCS of the *smooth* surface at $\theta_i = 50^0$ by the three analytical models are given in Figure 2.5. This figure shows that the HH and VV range-resolved RCS given by those analytical models match perfectly with those given by the MOM. The same agreement is shown in Figure 2.6 at $\theta_i = 80^0$.

PM-6 surface

Figure 2.7 shows the polarization range-resolved RCS of the *PM-6* surface at $\theta_i = 50^0$ predicted by these analytical models. SSA-1, SSA-1+2, and NLSSA predict

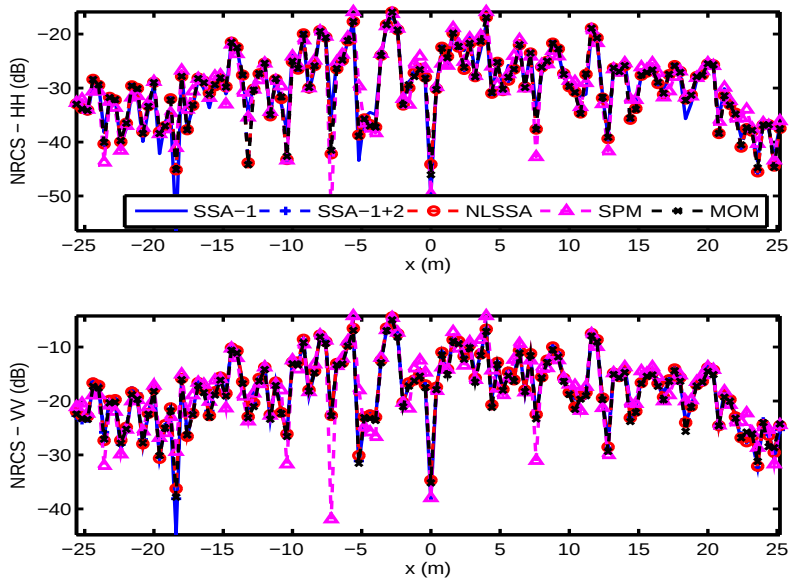

Figure 2.5: Range-resolved RCS of the *smooth* surface by selected analytical models ($\theta_i = 50^0$ and $\Delta r = 0.4$ m)

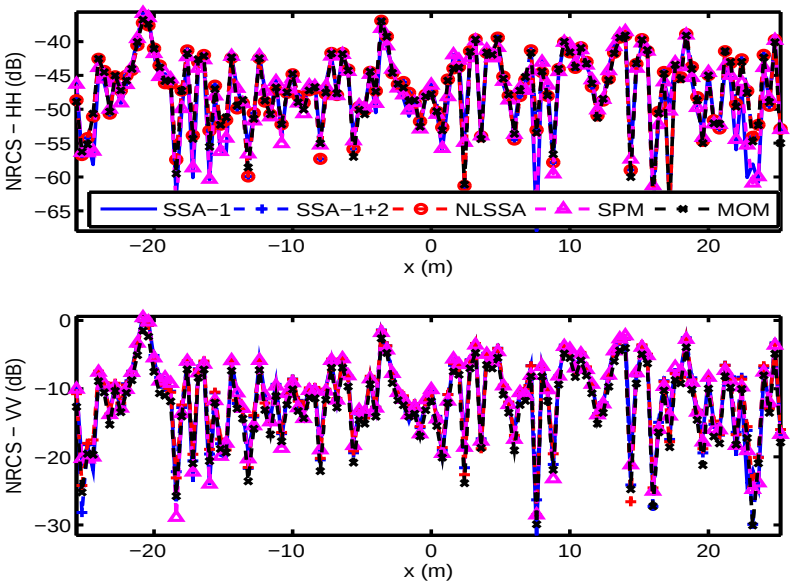

Figure 2.6: Range-resolved RCS of the *smooth* surface by selected analytical models ($\theta_i = 80^0$ and $\Delta r = 0.4$ m)

accurate HH polarization range-resolved RCS, and their analytical predictions of VV polarization have an acceptable accuracy. However, the range-resolved RCS predicted by the TSM deviates slightly from the exact value. Figure 2.8 shows the prediction results at $\theta_i = 80^0$. Both polarized range-resolved RCS predicted by the analytical models deviates from the exact values. However, their RCS envelopes are close to those of the exact values. In particular, for HH polarization, the TSM has a better accuracy than the other analytical models, and the VV range-resolved RCS given by the SSA-1+2 deviates too much at two edge regions at $\theta_i = 80^0$ due to the singularity of its kernel.

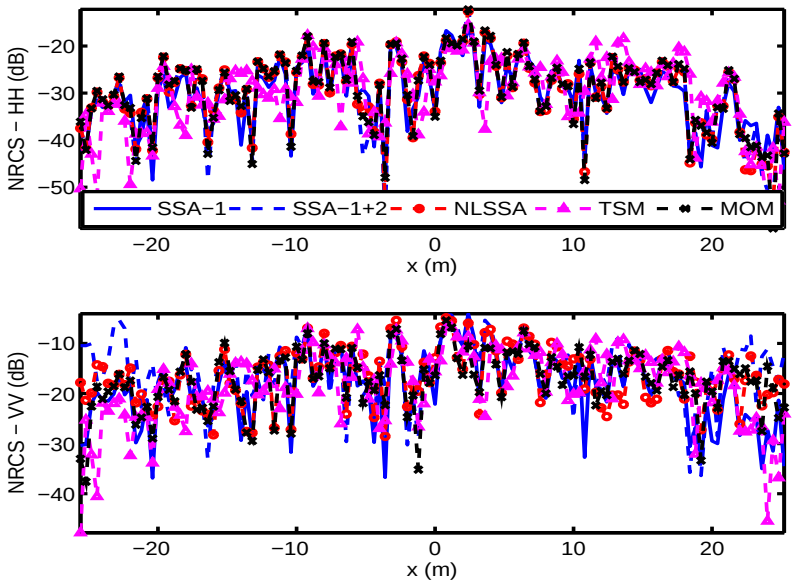

Figure 2.7: Range-resolved RCS of the *PM-6* surface by selected analytical models ($\theta_i = 50^0$ and $\Delta r = 0.4$ m)

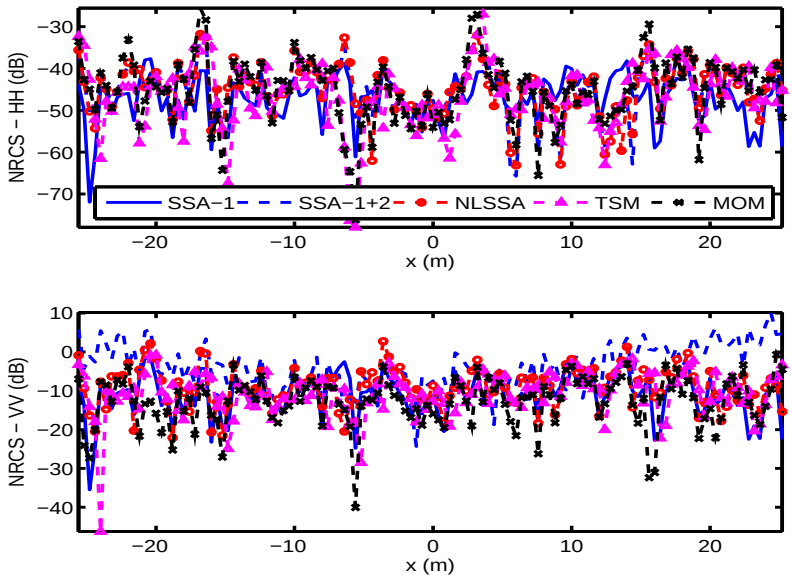

Figure 2.8: Range-resolved RCS of the *PM-6* surface by selected analytical models ($\theta_i = 80^0$ and $\Delta r = 0.4$ m)

PM-10 **surface**

For further analysis, a rougher surface, *PM-10*, than *PM-6* is studied at the same frequency. Figure 2.9 and 2.10 show the prediction results by these analytical models. Due to the similarity of range-resolved RCS among SSA-1, SSA-1+2, and NLSSA, only the results predicted by NLSSA are shown here. The results are similar to those presented in the case for *PM-6*. Again, the range-resolved RCS of HH polarization predicted by the TSM is the closest to that predicted by the MOM among results by the analytical models employed, but has only limited angle at 80^0.

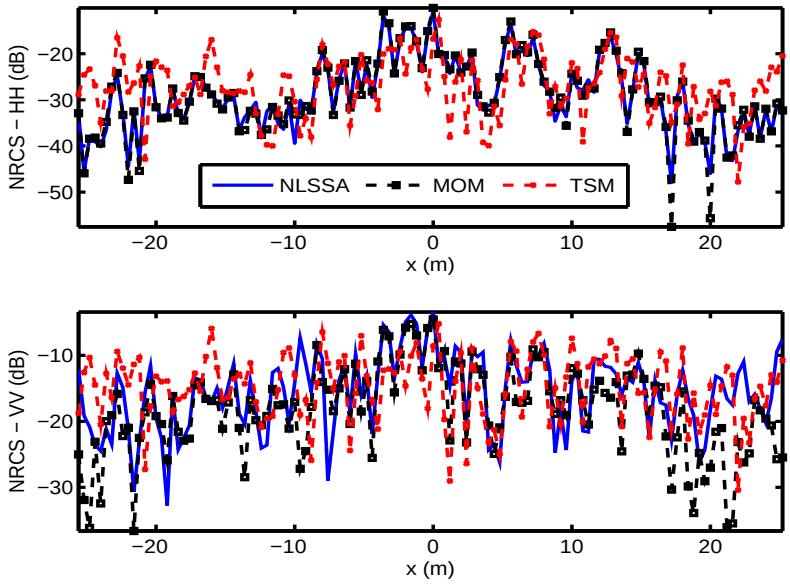

Figure 2.9: Range-resolved RCS of the *PM-10* surface by selected analytical models ($\theta_i = 50^0$ and $\Delta r = 0.4$ m)

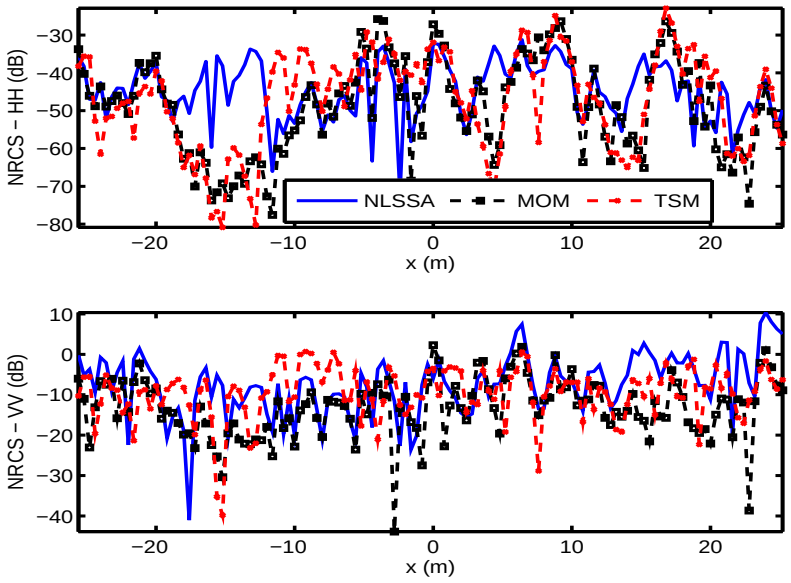

Figure 2.10: Range-resolved RCS of the *PM-10* surface by selected analytical models ($\theta_i = 80^0$ and $\Delta r = 0.4$ m)

Creamer surface

The *Creamer* surface shown in Figure 2.4 is nonlinear. In this section, we want to study the nonlinearity effect on the range resolved RCS. Figure 2.11 shows the range-resolved RCS of HH polarization at S-band predicted by selected analytical models. The conclusion indicated by this figure is still similar to those presented for linear surfaces. Figures 2.12 and 2.13 show the results from different models at $\theta_i = 50^0$ and $\theta_i = 80^0$, respectively. Again, we can draw a conclusion similar those given in previous linear surfaces. In particular, we can see that the TSM has the best, but limited, accuracy among these analytical models for HH polarization at $\theta_i = 80^0$.

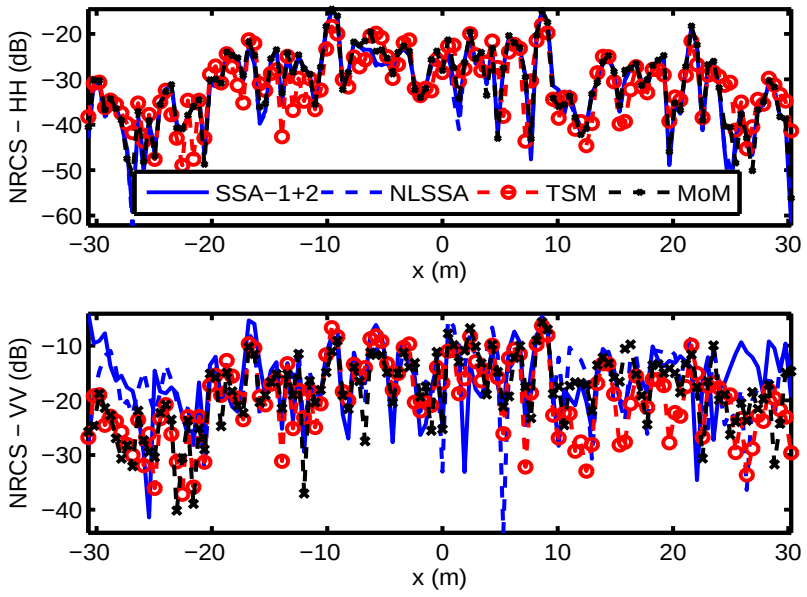

Figure 2.11: Range-resolved RCS of the *Creamer* surface at S-band by selected analytical models ($\theta_i = 50^0$ and $\Delta r = 0.48$ m)

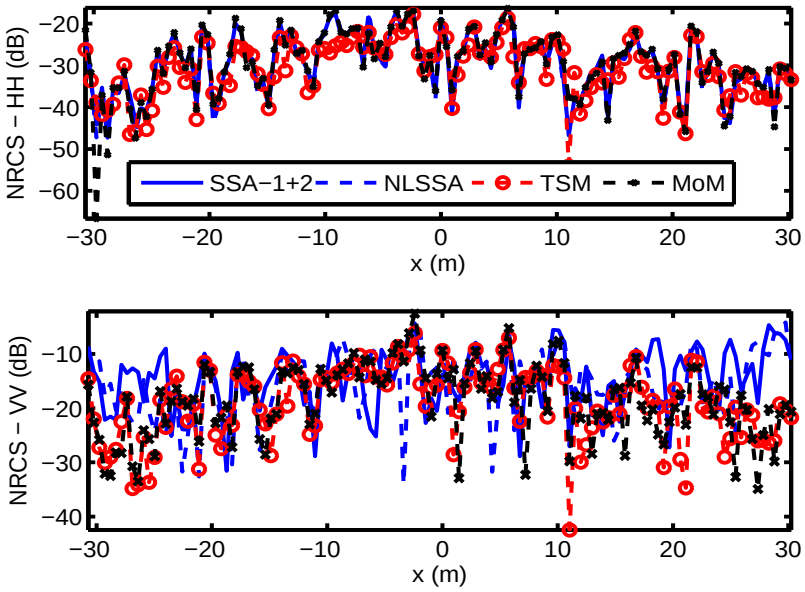

Figure 2.12: Range-resolved RCS of the *Creamer* surface at X-band by selected analytical models ($\theta_i = 50^0$ and $\Delta r = 0.48$ m)

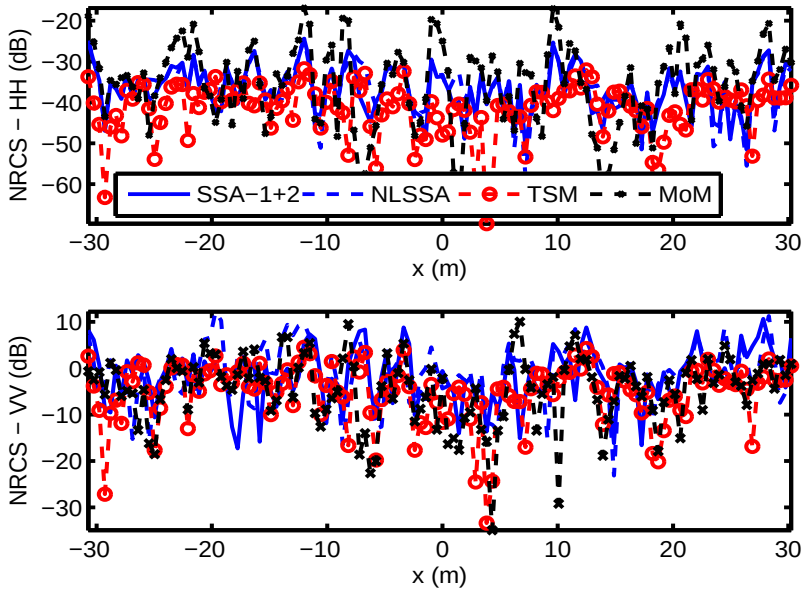

Figure 2.13: Range-resolved RCS of the *Creamer* surface at X-band by selected analytical models ($\theta_i = 80^0$ and $\Delta r = 0.48$ m)

2.3.2 Comparisons of numerical methods

To explore the physical scattering mechanisms at LGA, we study the range resolved RCS for both polarizations with the different numerical iteration procedures in Section 2.2.2.

Figures 2.14 and 2.15 show the polarized range-resolved RCS computed by different numerical iteration methods for the *smooth* surface at $\theta_i = 50^0$ and $\theta_i = 80^0$, respectively. The polarized range-resolved RCS given by all these different iteration methods have similar envelopes. The range-resolved RCS differences of VV polarization among all methods are much less than those of HH polarization. The differences indicate that the multiple scatterings make a larger contribution to the HH polarization than to the VV polarization. In particular, when $\theta_i = 80^0$ tends to LGA, the differences are larger than those at $\theta_i = 50^0$. In addition, the range-resolved RCS of both polarizations given by the *MOM* and the *Born* iteration in Figure 2.15 is smaller than that predicted by the others. One possible interpretation is that the multiple scattering might reduce some energy due to the interference between multiple scatterings. We can also see that the *Born* iteration method predicts almost the same result as that by the *MOM*, although the latter requires two or three additional iteration steps. The additional iteration steps depend on the convergence criterion which we initially set.

As the surface height increases, the result difference between the *MOM* and the other iterations also increases. Figures 2.16 and 2.17 show such differences for the *PM-6* surface. This figure shows that the difference at $\theta_i = 50^0$ is smaller than that at $\theta_i = 80^0$. In particular, the envelope of range-resolved RCS of HH polarization at $\theta_i = 80^0$ given by the *MOM* or *Born* iteration deviates far from that given by any

of the others. Only the envelope given by the *Forward* iteration has a trend close to that given by the *MOM*. As the surface height increases, the multiple scattering effect also increases. In addition, the possible shadowing may have an effect on the backscattering. Both multiple scattering and possible shadowing contribute to the large deviations.

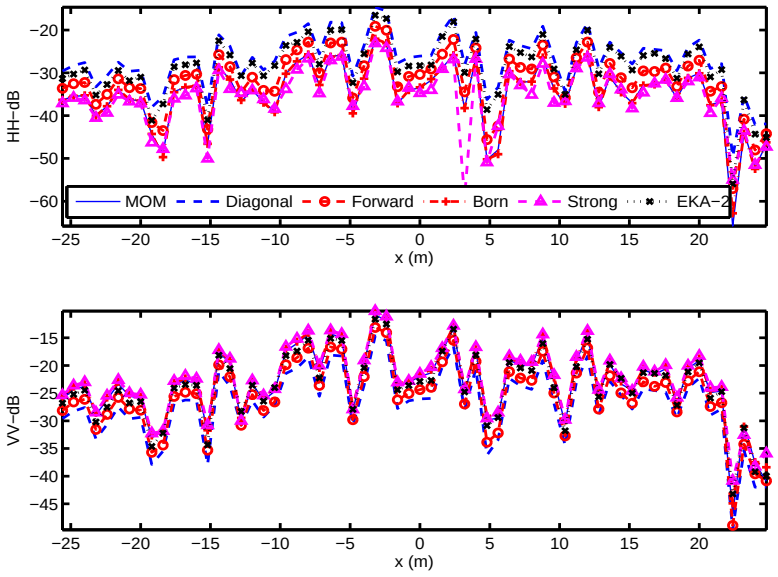

Figure 2.14: Range-resolved RCS of the *smooth* surface computed by different numerical iteration methods ($\theta_i = 50^0$ and $\Delta r = 0.8$ m)

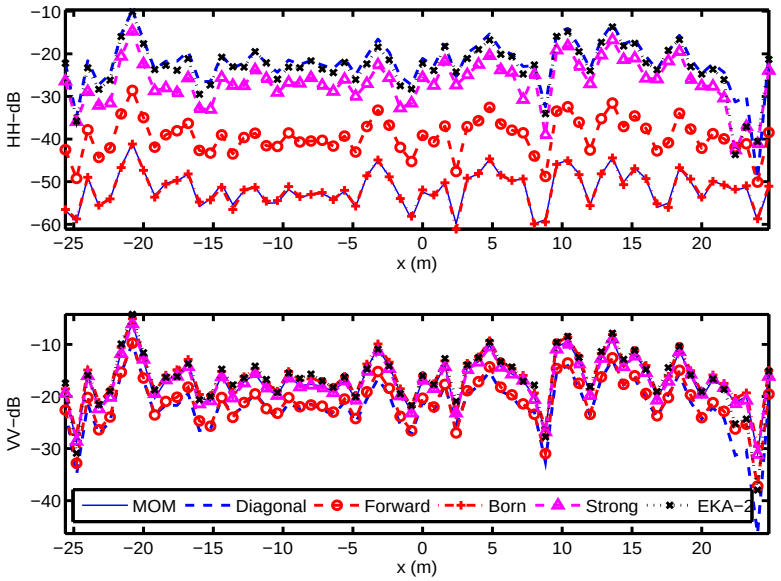

Figure 2.15: Range-resolved RCS of the *smooth* surface computed by different numerical iteration methods ($\theta_i = 80^0$ and $\Delta r = 0.8$ m)

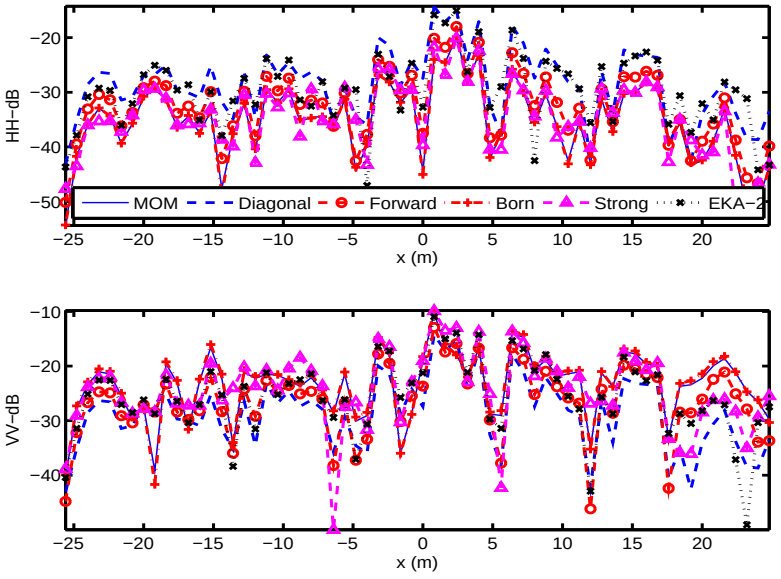

Figure 2.16: Range-resolved RCS of the *PM-6* surface computed by different numerical iteration methods ($\theta_i = 50^0$ and $\Delta r = 0.8$ m)

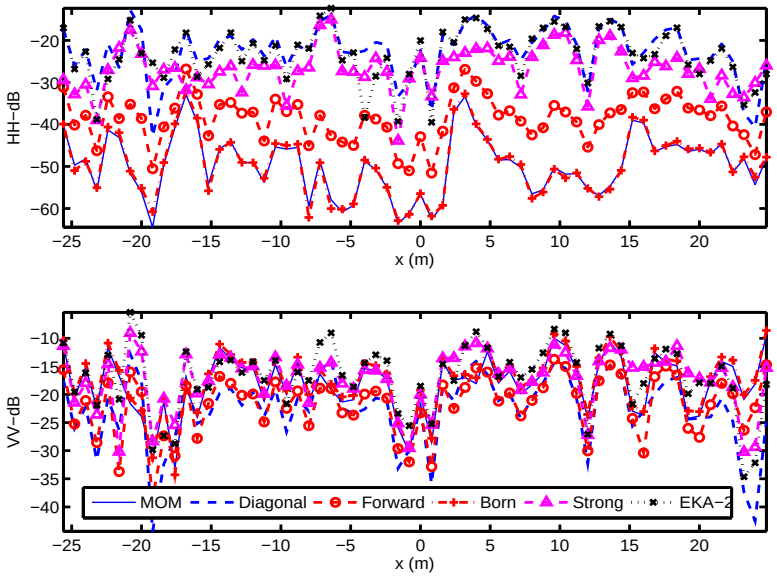

Figure 2.17: Range-resolved RCS of the *PM-6* surface computed by different numerical iteration methods ($\theta_i = 80^0$ and $\Delta r = 0.8$ m)

2.4 Conclusion

The concluding remarks, which are based on the polarized range-resolved RCS studies for four characteristic rough surfaces, are summarized as follows.

The analytical approaches (SPM-1, SSA, NLSSA) predict accurate polarized range-resolved RCS for a smooth surface at moderate angles, even at LGA. As the surface height increases, the range-resolved RCS given by SSA-1+2 and NLSSA match closely to the RCS that given by the MOM only at moderate incidence angles. While in the LGA case, only the TSM predicts a moderately accurate range-resolved RCS of HH polarization compared with the RCS that predicted by NLSSA and SSA-1+2 for HH

polarization. To obtain more accurate RCS, the development of analytical models which can include multiple scattering and shadowing are necessary at LGA.

In order to further analyze the scattering mechanisms that make significant contribution to range-resolved RCS, we perform detailed comparisons among different numerical iteration procedures. The comparisons demonstrate that the *Born* iteration achieves an enough accuracy with respect to the "exact" solution. The *Forward* iteration predicts an envelope of the range-resolved RCS close to that given by the "exact" solution. However, its prediction for HH polarization is lower than that by the "exact" solution. This is due to the multiple scattering. Therefore, at least one forward and one backward iteration is needed to obtain accurate backscattering field at LGA. The results are used in next chapter.

CHAPTER 3

PHYSICAL MODEL-BASED SURFACE RETRIEVAL FROM LGA RADAR DATA

3.1 Introduction

The retrieval of ocean surface profile information is of interest in the remote sensing community as well as in ship control and path planning applications. Recent research has qualitatively demonstrated profile retrievals using range-resolved radar cross section data from an oil-platform mounted X-band radar [44]. Profile retrievals in that work were produced under the assumption that the RCS depends only on the local surface slope. No "hydrodynamic modulation", non-Bragg scattering, or shadowing effects were explicitly included. In addition, an empirical relationship between the range-resolved RCS and the local slope is assumed in that study. While those results are encouraging, the numerous assumptions required leave uncertainty as to the accuracy of the retrievals obtained as well as to methods for improving those retrievals. For this reason, controlled simulations of scattering from time evolving surface profiles combined with assessments of profile retrievals are of interest.

The study described in this chapter, which has been reported in [60], is based on one-dimensional simulations of radar backscattering from ocean-like surfaces [22, 23,

61]. The surface profiles used are produced using a "Pierson-Moskowitz" spectrum, and modified to include approximate nonlinear effects in some cases through use of a weakly nonlinear approach [30]. Using ideas similar to those of Dankert and Rosenthal [44], an initial physical retrieval method is considered based on a tilted Bragg scattering model. Under this model, the range-resolved RCS can be written as an explicit function of the local surface tilt angle and the local short wave spectrum near the Bragg wavenumber. For simplicity, the short wave spectrum is assumed to be uniform along the entire surface, i.e., hydrodynamic modulation effects are neglected. In this case, the local incidence angle within a given radar range cell can be retrieved from RCS information alone. This local incidence angle can then be converted into the mean long-wave surface slope in the range bin, and ultimately integrated to obtain surface profile information. While the results reported here consider retrievals only for fixed surface profiles, the approach can be expanded to the time evolving case by passing profiles retrieved at multiple time steps through a filter in space-time in an attempt to ensure that surface features propagate in a manner similar to that expected for long gravity waves. Overall issues in the retrieval process involve quantifying the accuracy achieved, as well as the investigation of the influence of varying sensors (i.e. incidence angle, polarization, center frequency, bandwidth, etc.) and surface (linear or nonlinear, winds peed, etc.) parameters. Only initial results are reported here, and only HH polarization results are utilized due to the larger impact of "tilting" effects on HH cross sections as compared to those on VV cross sections .

The influence of incidence angles, varying range resolutions, and use of linear and non-linear approachs for surface evolution on retrieval accuracy are described. In

addition, descriptions of continued studies using an S-band center frequency as well as other surface configurations are provided.

3.2 Methodology

3.2.1 Simulated ocean surface

Ocean surface profiles in the simulation are generated assuming a Gaussian random process surface with a "Pierson-Moskowitz" power spectrum, as described in [22, 23]. Non-linear effects are incorporated using Creamer et al's improved linear representation [30], which provides a transformation of the linear surface to capture first-order non-linear gravity wave-wave interactions. Surface profile properties are parametrized only by the ocean surface wind speed at 19.5 m. Results are shown using values of 5, 6, and 10 m/sec. The profiles generated have a horizontal length $L = 122.88$ m and $L = 102.4$ m (approximately 4096 electromagnetic wavelength at 10 GHz, and 1024 electromagnetic wavelength at 3 GHz), respectively for 10 GHz and 3 GHz. Surfaces are assumed to be PEC again in this chapter.

3.2.2 Numerical electromagnetic scattering model

Backscattered fields computed at 60^0, 80^0, and 85^0 incidence angles are used in this study, and those data at 80^0 are only used for retrieval. The "tapered-beam" of [53] with taper parameter $g = L/6$ is utilized to reduce edge scattering effects. This choice combined with the surface profile length used is sufficient to provide reasonable computations at 80 degrees incidence. Note that the "tapered wave" illumination utilized is not a complete model of a true ship-mounted radar, due to the variation of incidence angle with range that occurs for a true radiating source. More realistic source models will be considered in future work. The numerical model

applied is based on the solution of the magnetic field integral equation (MFIE) formulation [56]. Due to the large surface length at X-band (4096 wavelengths sampled into 65536 unknowns), the iterative MOMI solution [46] combined with the novel spectral acceleration technique [47, 57] is used to improve computational efficiency. Frequency-swept data at X-band are computed using a center frequency of 10 GHz and a bandwidth 1.25 GHz, sampled into 1024 frequency steps; these parameters yield a maximum range resolution of around 0.12 m. Further detailed information on the dataset and numerical simulations is given in [61]. Similar computations were performed at S-band (center frequency 3.0 GHz, bandwidth 1.5 GHz) using identical surface profiles but sub-sampled to 16384 points only due to the reduced center frequency.

Retrieval procedures

The plots of Figure 3.1 provide a basic illustration of typically observed relationships between the surface profile (upper plot), the RCS versus range (middle plot), and the surface slope. The slope plot shown was obtained by filtering out short waves in the surface spectra above a threshold based on the electromagnetic wavelength. This threshold was chosen in order to improve the match between variations of the slope and the downrange RCS. There are three different down-range RCS curves in the middle plot of Figure 3.1, and the range-resolved RCS at 60^0 does not show good consistency with the surface profile. The other data, given incidence angles at 80^0 and 85^0, are very close to each other. However, the data at 80^0 are chosen in this study in order to neglect the multiple scattering and possible shadowing effects compared to the data at 85^0. In addition, the data at other time steps show phenomena similar to those demonstrated in Figure 3.1. The results in Figure 3.1 show some correlation of

surface slope and X-band RCS, although the relationship is not always consistent. In addition, the fairly low wind speed considered results in fairly small height surfaces (as is apparent in the upper plot) so that tilting effects are smaller than they would be at larger wind speeds.

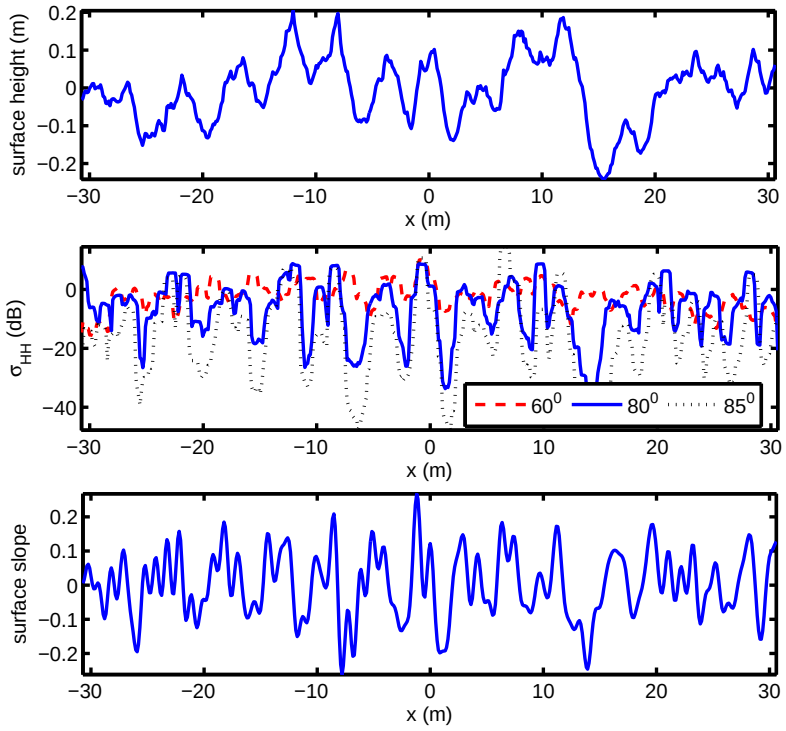

Figure 3.1: Comparison of surface profile, surface slope, and down-range RCS at X-band for a sample surface

The first-order small perturbation model (SPM) states that the scattered field is a function of the local incidence angle, radar frequency, and the Bragg spectrum of the illuminated range cell. Although the Bragg spectrum for realistic sea surface is locally affected by hydrodynamic modulation effects [25], we again follow the approach of [44] and explore profile retrievals neglecting these effects. A simplified form of the

SPM model for the range-resolved RCS is then

$$\sigma_{HH} \approx C_0 \cos^3(\theta_{il}) W \approx A \cot^3(\theta_{il}), \tag{3.1}$$

where $W \approx \frac{C_1}{\sin^3(\theta_{il})}$ is the sea surface spectrum evaluated at the Bragg wavenumber of the given range cell under the assumption of a k^{-3} power-law spectrum, θ_{il} is the local incidence angle in a given range cell, and C_0 and C_1 are constants. This equation can be solved to determine a simple relationship between the RCS measured and the local incidence angle:

$$\theta_{il} = \cot^{-1}\left[\left(\frac{\sigma_{HH}}{A}\right)^{1/3},\right] \tag{3.2}$$

where σ_{HH} is the RCS of a given range cell, and A is estimated using equation (3.1) with the RCS averaged over all range bins and assuming θ_{il} is the nominal incidence angle.

Once the local incidence angle is known, the local slope is determined given the deviation from the global incidence angle. If equation (3.2) is further linearized, and expressed in terms of surface slope through a transformation of θ_{il}, it can be shown that this approach predicts a surface slope that is proportional to the cube root of the normalized RCS (i.e. σ_{HH}/A) value (see Figure 3.2). Finally, an integration of the surface slope is evaluated to obtain the surface profile [44]. This integration is implemented by an FFT, and a low-pass filter is applied so that the retrieved profile contains only frequency components lower than a specified cutoff. This is reasonable for ship control applications given the dominant influence of long gravity waves. Unlike [44], retrievals in this chapter are performed at individual time steps, without use of information at other time steps. Retrievals for time evolving surfaces will be

explored in future work. Due to the tapered illumination, retrievals are performed only for the central portion (length as 61.44 m) of the surface.

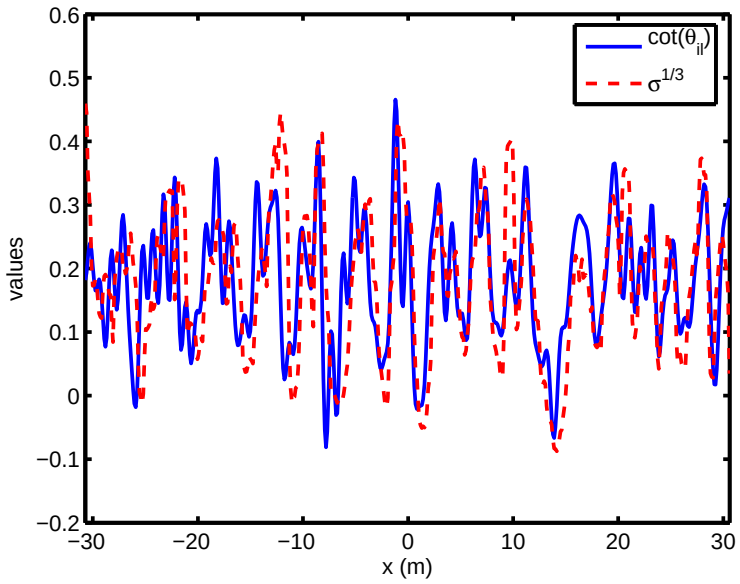

Figure 3.2: Comparison of surface slope and cubic root of RCS at X-band for a sample surface

3.3 Results and discussions

Figure 3.3 plots the surface profile retrieved from the X-band data of Figure 3.1 following the process described above. The results show that many surface features are captured by the retrieval, but significant errors are also achieved. However a strong correlation of the true and retrieved profiles overall is evident.

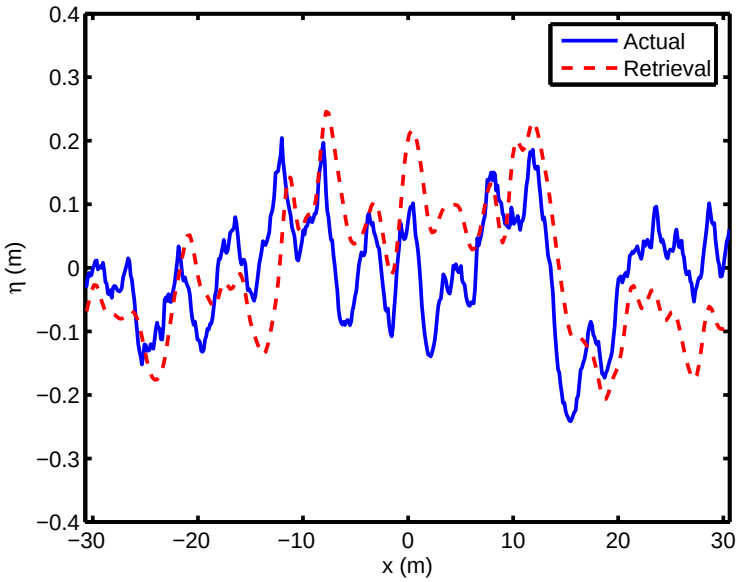

Figure 3.3: Comparison of true and retrieved surface profile using X-band data

3.3.1 Sidelobe window effect

Figure 3.4 shows the retrieval results with two different Gaussian windows which are added to suppress the sidelobe effect prior to the IFFT step, where dr denotes the 3 dB width of the window. It turns out that the window effect is small in generating the range-solved RCS given the same scattering data (it is 1024 sweep frequencies data in this simulation). All major slopes of the surface are recovered from the retrieval result. However, there are some systematic deviations between the retrieval and the original, which may be caused by the error in retrieval phase information due to the actual multiple scattering. The hydrodynamic modulation effect may also contribute to the retrieval discrepancy.

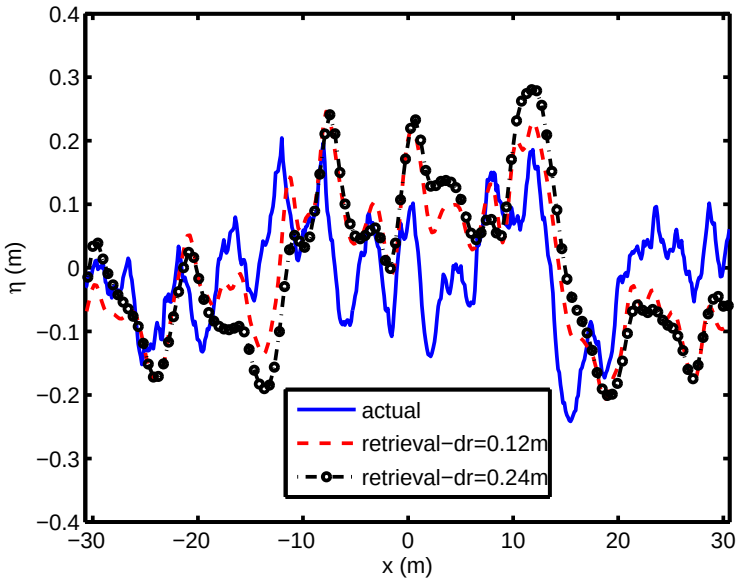

Figure 3.4: The surface retrieval from 80^0 scattering data at X-band

3.3.2 Surface roughness effect

One issue in the case considered above involves the low wind speed, which may result in only moderate tilting effects and therefore reduce retrieval accuracy. A further analysis was performed for linearly generated (i.e. neglecting the Creamer transformation) surfaces at 19.5 m wind speed 6 m/s (Figure 3.5) and 10 m/s (Figure 3.6), using S-band data. Results show a dramatic improvement in this case, at least for large scale surface features, due to the increased level of the tilting effects at higher wind speeds.

In order to examine the surface roughness effect and minimize the hydrodynamic modulation effect, a relatively "rough" surface whose length is 102.4 m with electromagnetic unknowns 16384 is retrieved at S-band (central frequency 3 GHz with

bandwidth 1.5 GHz). The retrieval result is shown in Figure 3.5. Obviously, the result is close to the original surface at each major slope change, as well as the relative height. However, we notice that the retrieval results have larger differences close to surface edges, which may be addressed by the tapered illumination. These retrievals from two different surfaces (linear and nonlinear) demonstrate that the Bragg scattering model at HH polarization does have a reasonable accuracy for keeping the phase variation. Actually, the first-order SPM inherently ignores multiple scattering. In order to achieve a better retrieval result, we may need to improve the scattering model, which should account for the hydrodynamic modulation, multiple scattering, and possible shadowing effects.

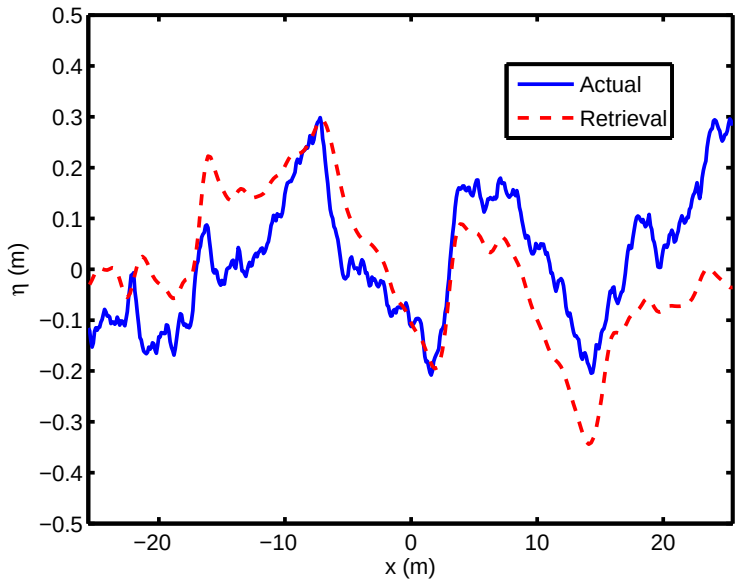

Figure 3.5: Comparison of true and retrieved surface profile using S-band data for wind speed 6 m/sec

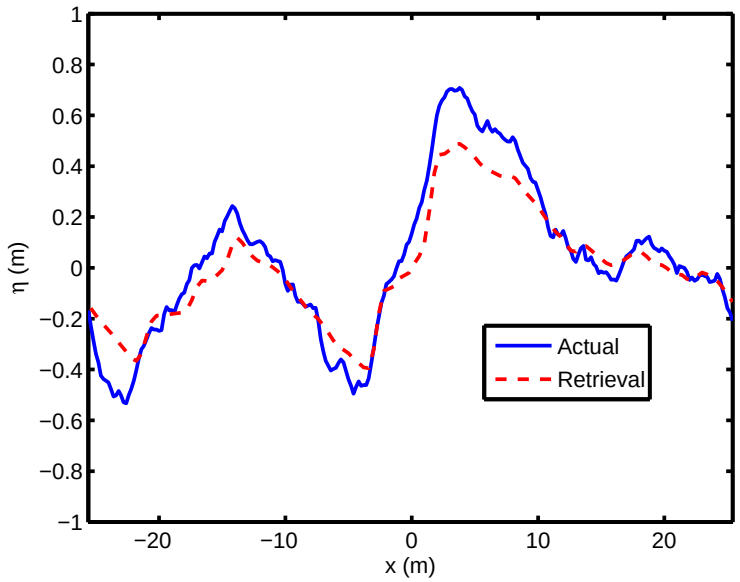

Figure 3.6: Comparison of true and retrieved surface profile using S-band data for wind speed 10 m/sec

Nonlinear effect

In order to numerically evaluate the nonlinear effect on the scattering and its retrieval at LGA, the Creamer's surface and regular PM surface are studied. This nonlinearity accounts for the hydrodynamic modulation. Figure 3.7 indicates that the nonlinearity have a small effect on the retrieval in this case.

3.4 Conclusion

Results from this initial study show that sea surface profile retrievals using range-resolved RCS measurements indeed appear to be feasible. The results shown demonstrate the limitations of a simple "tilted Bragg" retrieval method at low wind speeds, and typically show the S-band to provide improved performance over the X-band.

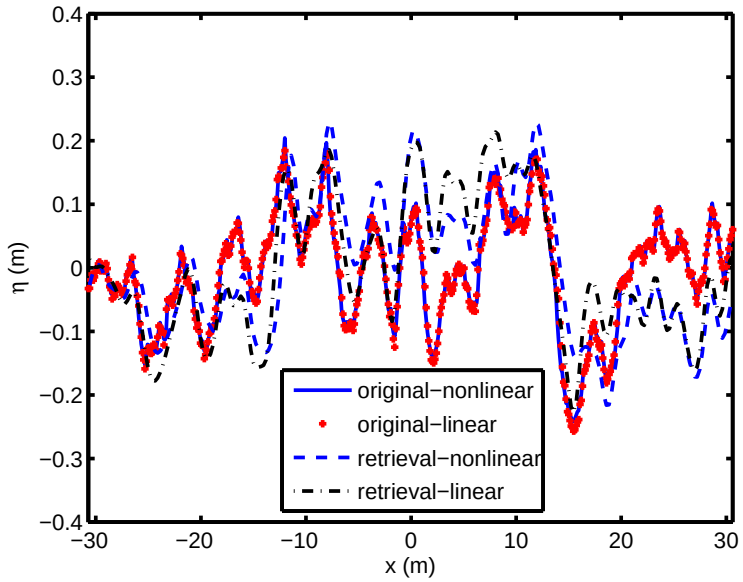

Figure 3.7: The surface retrieval from 80^0 scattering data at S-band with/without MTF

Further studies also consider retrievals that utilize multiple surface time steps, as well as Doppler frequency information (see Chapter 6).

By use of the tilted small perturbation model as the inverse electromagnetic scattering model, the local surface slope and surface profile can be retrieved reasonably from the range-resolved RCS data. However, there are still some systematic discrepancies between the retrieval and the original surfaces, which may be attributed to the inaccuracy of the first SPM model. The hydrodynamic modulation effect on this retrieval is also studied, and our preliminary result shows its effect is small; however, this small difference may have two possibilities: a true small effect of HMTF, or a

SPM model accuracy issue which does not include the HMTF. A more rigorous hydrodynamic model which inherently include the HMTF is needed for the analysis of the HMTF influence on the model based retrieval.

CHAPTER 4

A NUMERICAL STUDY OF THE MODULATION OF SHORT SEA WAVES BY LONGER WAVES

4.1 Introduction

It is well known that the amplitudes and wavenumbers of short water waves are modulated when propagating over an underlying long water wave or current [62, 63]. These modulations represent a non-linear hydrodynamic interaction between sea waves; such interactions however are typically not resonant interactions, so that no secular change of the short wave spectrum occurs with time. Thus these effects are typically ignored in attempts to model and forecast the sea surface spectrum using an energy balance approach.

Modulations of short waves by longer ocean waves do play an important role however in radar imaging of the sea surface. In this case, the commonly applied "two-scale" model of sea backscatter states that radar returns with a specific range cell are produced by short waves (or Bragg waves) within the range cell, observed at the local incidence angle of the range cell. When sea waves of wavelengths larger than the radar range cell are present within a radar image, the resulting changes in the local incidence angle ("tilt modulations") across the larger sea waves produce

variations in the measured radar cross section image, typically allowing the sea waves to be observed. In addition to the tilt modulation effect, variation in the Bragg wave amplitudes along the long waves through hydrodynamic modulations also produce variations in the radar cross section with range. It is generally assumed in sea radar imaging that the tilt modulation effect is well understood, so that remaining variations are produced by hydrodynamic effects. This process allows empirical studies of the "hydrodynamic modulation transfer function" (HMTF) (as in [24]) to be performed through analysis of measured radar images. However the modulations obtained are influenced by numerous geophysical factors at the time and location of the measurements, so that validating any hydrodynamic theories of the HMTF can be difficult.

Existing analytical theories of the HMTF are primarily based the concept of conservation of wave action [24, 25, 26, 27, 28]. In these theories, the basic equations state that the wave action of the short waves is conserved except for the presence of a set of source and dissipation terms. The former include effects such as short wave generation by either wind forcing, non-linear interactions, or wave breaking, while the latter includes viscous damping and other dissipative effects. Empirical models are utilized to describe most of these contributions. Although it is possible to numerically solve the resulting wave action equations through the method of characteristics, an approximation to first order is typically used in the remote sensing literature to determine the HMTF. At this order, long wave effects appear near identical to those from currents, with the current amplitude equal to the horizontal component of the long wave orbital velocity.

While this first order HMTF analysis has been applied in numerous remote sensing studies, significant evidence exists in the literature that this model under-predicts the actual modulations observed [24, 64]. While such under-prediction can be corrected by modifying or adding new source and dissipation terms in the wave action equations, it is difficult to separate the accuracy of the hydrodynamic model from accuracy in description of source and dissipation terms.

To address this issue, a study of the HMTF is described in this paper based on the use of numerical algorithms for sea surface hydrodynamics. The hydrodynamic algorithm applied is based on the pseudo-spectral method [29], hereinafter denoted as the "Watson-West" or WW approach. This algorithm has been applied previously in studies of gravity wave evolution [29, 65, 66, 67] as well as radar scattering from the sea surface [23, 32]. Although the pseudo-spectral method is not exact, it has been shown in numerous studies [29, 65, 67] to provide high fidelity hydrodynamic simulations so long as the order of the algorithm is sufficiently high and so long as steep features are avoided in the surface evolution. The numerical approach involves Monte Carlo simulation of the hydrodynamic evolution of a spectrum of short sea waves in the presence of either one or two deterministic long waves. Because no wind, wave breaking, or viscous dissipation effects are included in the simulation, the results of this simulation allow assessment of the accuracy of the first order HMTF often used in practice.

In Section 4.2, the WW algorithm is described, along with the simulation procedure utilized. A method for extracting a "numerical HMTF" from the simulated data is presented in Section 4.3, and results obtained are presented in Section 4.4. A numerical study of the short wave dispersion relation is described in Section 4.5.

Section 4.6 provides a review of the analytical first order HMTF for comparison with the numerical results. Tests show that the numerical HMTF values are in reasonable agreement with those from the analytical theory, although small differences are observed that indicate that improved formulations of the first order theory may be desirable. Final remarks are provided in Section 4.7.

4.2 Numerical hydrodynamic simulations

4.2.1 Formulation

The studies of this paper utilize a one dimensional fluid surface of infinite depth, and assume that the fluid is incompressible and inviscid; surface tension effects are also neglected. The surface elevation is denoted as $z = \eta(x,t)$ and the surface velocity potential as $\phi(x,t)$, where (x,z) are the horizontal and vertical space coordinates, respectively, and t represents time. The evolution of these two quantities is determined by the following equations [29]

$$\phi_t = -g\eta - \frac{1}{2}\phi_x^2 + \frac{1}{2}\phi_z^2[1+\eta_x^2] \tag{4.1}$$

$$\eta_t = -\phi_x\eta_x + \phi_z[1+\eta_x^2], \tag{4.2}$$

where the subscript denotes the associated derivative and g is the gravitational acceleration (9.8 m/s^{-2}). We solve equations (4.1-4.2) using the pseudo-spectral method of [29], and retain terms up to 4th order in the slope expansion.

4.2.2 Initial conditions

Initial conditions for the simulations include one or two deterministic "long" wave(s) and a stochastic spectrum of "short waves", in order to study modulation of

the short wave spectrum. The specific initial condition with one long wave is

$$\eta(x, t = 0) = a_1 \sin(k_1 x) + \eta_s(x), \tag{4.3}$$

$$\phi(x, t = 0) = -a_1 \sqrt{g/k_1} \cos(k_1 x) + \phi_s(x) \tag{4.4}$$

where the long wave has wavenumber k_1 and amplitude a_1. It is assumed that the long wave lies in the gravity wave region, and the initial conditions are developed to produce a long wave traveling in the $\hat{x}$ direction in the linear hydrodynamic limit. Previous work with such initial conditions [29, 67] shows the tendency of the long wave to approach a Stokes' wave form for moderate $k_1 a_1$ values. The computational domain is set to 2π meters, and the long wave wavenumber is set to $k_1 = 1$ rad/m in the majority of the results to be shown. Note that a scale transformation is possible for surface composed only of gravity waves, so that these simulations also represent hydrodynamic effects for gravity wave surfaces with the length and height dimensions scaled by a constant.

The initial short wave surface η_s is a realization of a Gaussian random process surface with a Pierson-Moskowitz spectrum [23]:

$$S(k_s) = \frac{0.0081}{4} k_s^{-3} \exp(-\frac{0.74 g^2}{k_s^2 U_{19.5}^4}), \tag{4.5}$$

where $U_{19.5}$ denotes the surface wind speed at height 19.5 m. This spectrum essentially is a k_s^{-3} spectrum for one dimensional surfaces, with a low frequency roll-off controlled by a windspeed parameter $U_{19.5}$. The initial short wave spectrum is truncated to exist between wavenumbers 30 rads/m and 170 rads/m only. The lower limit of 30 rads/m ensures that the short waves are indeed "short" compared to the long wave, while the upper limit is chosen based on surface sampling requirements. Although the parameter $U_{19.5}$ was set to 3 m/s, the portion of the P-M spectrum influenced

by $U_{19.5}$ has wavenumbers much less than 30 rads/m, so that $U_{19.5}$ has virtually no effect. The short wave velocity potential $\phi_s(x)$ was generated again through a linear, $\hat{x}$, traveling assumption for each spectral component of $\eta_s(x)$. The generated surface was sampled into 1024 points, providing sufficient resolution to resolve the short wave spectrum while retaining fourth order computations in the WW method.

Because the linear assumption of the initial conditions does not match the non-linear nature of equations (4.1-4.2), we utilize a "ramp-up" procedure [29], [23] to reduce any discontinuities that may be introduced. In this procedure, all non-linear terms in the evolution equations (4.1-4.2) are multiplied by a ramp-up factor

$$W_R(t) = e^{-(\frac{t-a}{b})^2} \tag{4.6}$$

for $t < a$, and by unity for $t \geq a$. Note for $t << a$ this term is zero, while it approaches unity for $t = a$ at a rate determined by b. We have tested several combinations of a and b, and found $a = 2$ sec and $b = 0.5$ sec in equation (4.6) to yield reasonable predictions; this approach is similar to that described in [68]. Here 2 sec is approximately one period of the long wave.

As the surface evolves in time, short waves have only a minimal effect on the evolution of the long wave, given their much smaller amplitude. The short wave spectrum, however, broadens from the truncated spectrum provided initially and exhibits some interactions among short waves. However the dominant effect to be examined here is the variation in the local short wave spectrum with position on the long wave. For this purpose, localized short wave spectra will be introduced in Section 4.3 so that the variation of these localized spectra with position on the long wave can be observed.

4.2.3 Other information

The simulation was time stepped at $\Delta t = 0.001$ sec for a duration of 5000 time steps (5 sec) [1] following the ramp-up period. Surface profiles were recorded every 0.1 seconds, providing 50 profiles per realization. The simulation was repeated using 1200 distinct short wave surface realizations so that average spectra could be computed. Tests with larger numbers of realizations showed this choice to provide reasonable convergence for the results illustrated. Figure 4.1 compares the initial input spectrum and final ensemble averaged spectrum of short waves in the presence of a long wave with $k_1 a_1 = 0.05$. The result shows that the short wave spectrum remains relatively constant during its evolution. The dataset produced by the simulation consists of surface profile information $\eta(x_q, t_i, M_j)$, where x_q and t_i refer to the discretized horizontal and time coordinates, and M_j provides an index to the set of realizations generated.

4.3 Determination of the numerical HMTF

The configuration of this simulation allows long-short wave hydrodynamic modulations to be examined in detail. For this purpose, the computational domain in x is divided into sub-regions, and local Fourier transforms (using a Fast Fourier Transform (FFT) algorithm) are utilized to compute the spatially localized short-wave spectrum for each region. The specific procedure is as follows:

1. Begin a loop over time t_i;

2. Begin a loop over realizations M_j;

[1] The optimum time duration should be an integer of long wave period, i.e., 2n sec (n - an integer). However, our simulations shows there is negligible effect on numerical MTF between 4 sec and 5 sec.

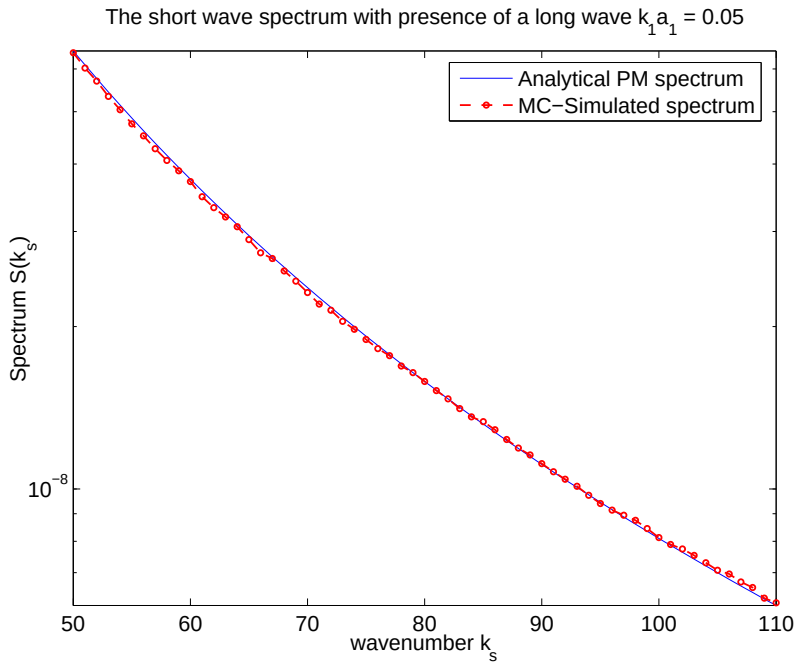

Figure 4.1: Comparison of initial and final short wave spectra with $k_1 a_1 = 0.05$

3. Filter out all long wave components by passing the $\eta(x_q, t_i, M_j)$ surface through a spatial rectangular high pass filter with cutoff $k_s = 30$ rads/m: call the resulting short wave surface $\eta_s(x_q, t_i, M_j)$;

4. Divide the x range into 31 spatial sub-regions, each sub-region has a half overlap to its preceding one; label these sub-regions by their central x-values X_n;

5. Begin a loop over sub-regions X_n;

6. Multiply $\eta_s(x_q, t_i, M_j)$ by a Gaussian window centered at X_n, and perform an FFT zero padded to the length of the original profile on the result; denote FFT output as $\eta_{sn}(k_s, X_n, t_i, M_j)$

7. Take $|\eta_{sn}(k_s, X_n, t_i, M_j)|^2$ to obtain the spectrum $S(k_s, X_n, t_i, M_j)$;

8. End loop over sub-regions;

9. End loop over realizations;

10. End loop over time.

In the above, the Gaussian window length is chosen as 64 points ($\sim$ 40 cm) with overlap 32 points, which results in 31 spatial sub-regions; a plot of the first several Gaussian windows is illustrated in Figure 4.2. Parameters of the Gaussian function are chosen so that the Gaussian is at e^{-1} at 18.1 points from the center of the filter. Tests varying these parameters within a reasonable range show only minor effects on the obtained MTF values.

Figure 4.3 shows the localized $S(k_s, X_n, t_i, M_j)$ variation both in time and spatial sub-region. $S(k_s, X_n, t_i, M_j)$ can then be averaged over realizations to obtain the ensemble average localized spectrum $S_a(k_s, X_n, t_i)$, which describes the average evolution of the spectrum with time in a given sub-region. This can be correlated to the approximate long wave phase versus time in that sub region:

$$\Phi_l = k_1 X_n - \omega_1 t_i, \tag{4.7}$$

where $\omega_1 = \sqrt{gk_1}$; it is also possible to determine the long wave phase numerically if desired. Because tests showed only minimal differences between these two methods, the former approach is utilized in the results shown. Finally, an additional average over time can be performed to obtain $\bar{S}(k_s, X_n)$, the ensemble and time average spectrum in a given sub-region.

Figure 4.4 illustrates the normalized quantity $S_a(k_s, X_n, t_i)/\bar{S}(k_s, X_n)$ for sub-regions 1, 5, 10, and 15 (relative initial long wave phases of $\pi/16$, $5\pi/16$, $10\pi/16$, and

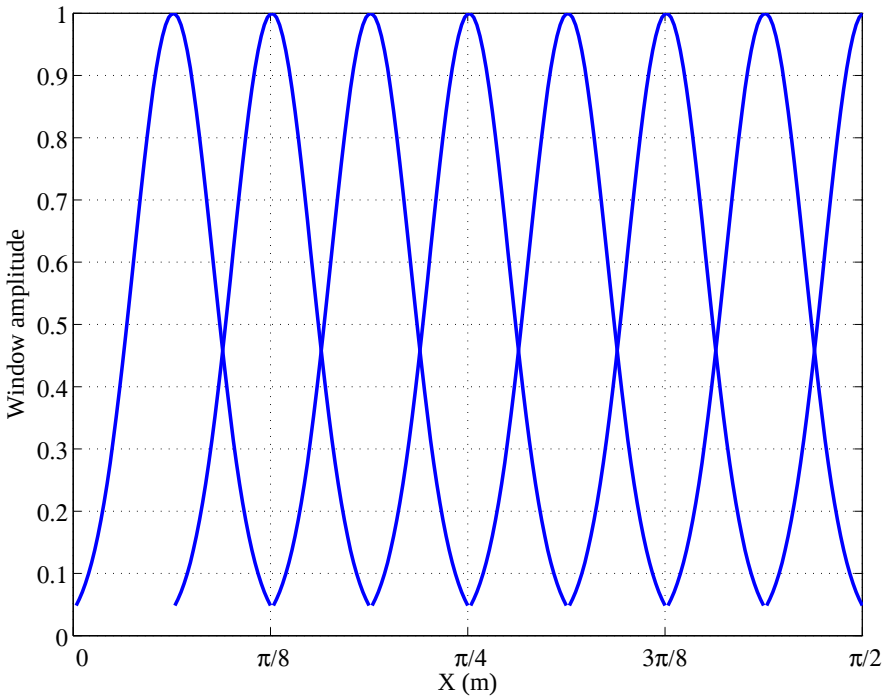

Figure 4.2: Illustration of the first 8 Gaussian windows used in defining spatial sub-regions

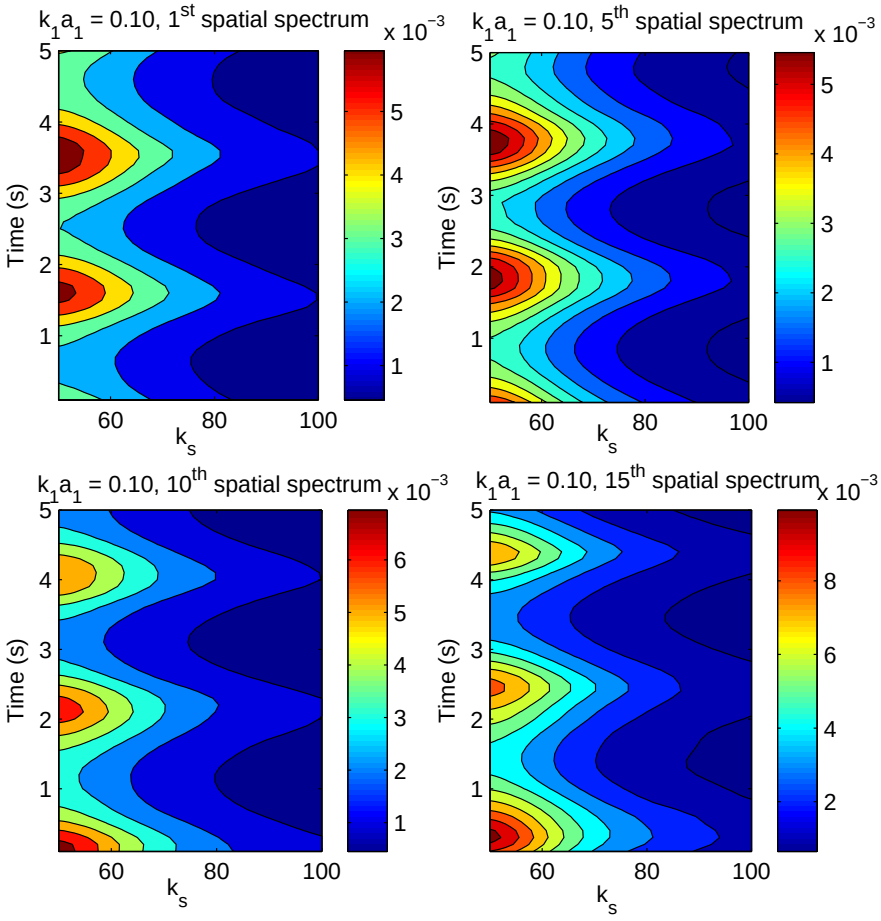

Figure 4.3: The localized spectrum of $k_1 a_1 = 0.10$

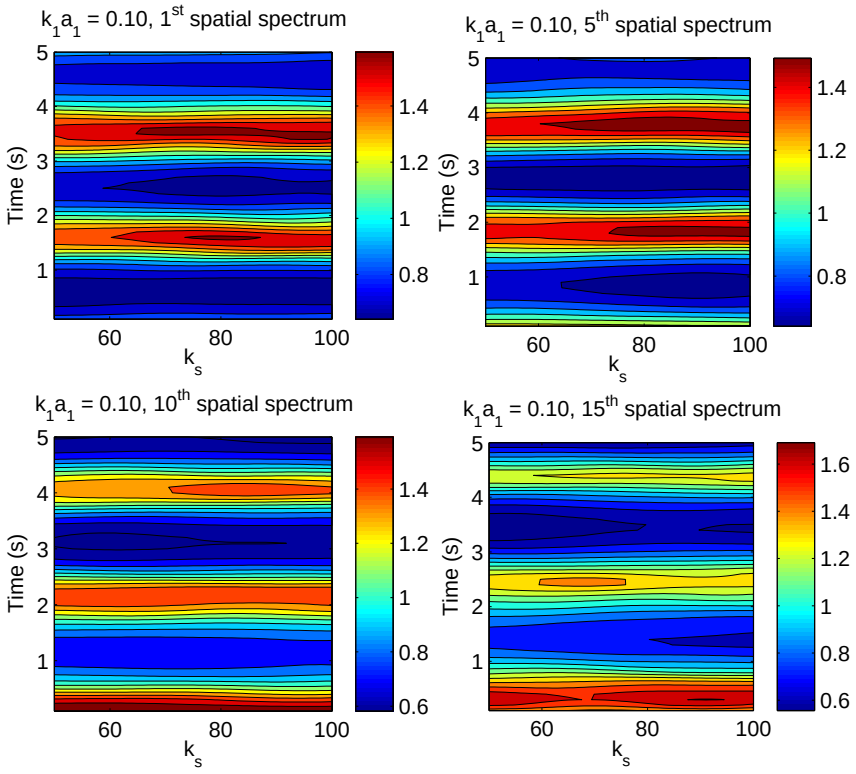

Figure 4.4: The normalized-localized spectrum of $k_1 a_1 = 0.10$

$15\pi/16$, radians, respectively) and for k_s values ranging from 50 to 100 rads/m, with $k_1 a_1 = 0.10$. The influence of the long wave is clearly visible in these plots through the periodic variation in the normalized-localized spectra obtained; the period of the oscillation observed is consistent with that of the long wave. Although some variations from simple oscillations are obtained, the basic spectrum modulations are clearly correlated to the long wave phase in a given sub-region.

Given this behavior, we define the numerical modulation $\mathfrak{R}(k_s, X_n, t_i)$ as follows:

$$\mathfrak{R}(k_s, X_n, t_i) = \frac{S_a(k_s, X_n, t_i) - \bar{S}(k_s, X_n)}{\bar{S}(k_s, X_n)}. \tag{4.8}$$

Note the spectrum in the denominator could be further averaged over sub-regions, but again this modification does not yield significant variations in the obtained MTF values.

Figure 4.5 plots an example value of $\mathfrak{R}$ versus time ($k_s = 70$ rads/m in the 10th sub-region). The oscillation of the spectrum is obvious, although an additional slow amplitude decay in time is observed that is not directly related to the long wave phase. We performed several tests of this slow decay, and found it to be a much slower periodic function, evolving at a time rate involving the group velocity of the short wave spectrum (see Figure 4.6). While such effects do play a role in the evolution of the surface, and could likely be captured by a full simulation of the wave action equations, they are not of interest in studying first-order MTF effects, and therefore a procedure for removing these slow time variations in extracting a numerical MTF value was developed.

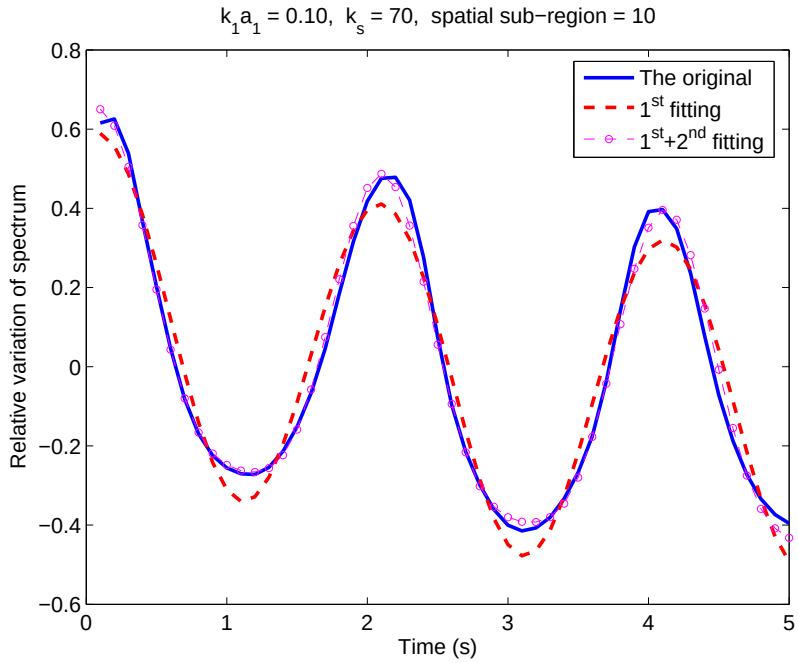

Figure 4.5: The envelope of the total numerical HMTF versus time with $k_1 a_1 = 0.10$

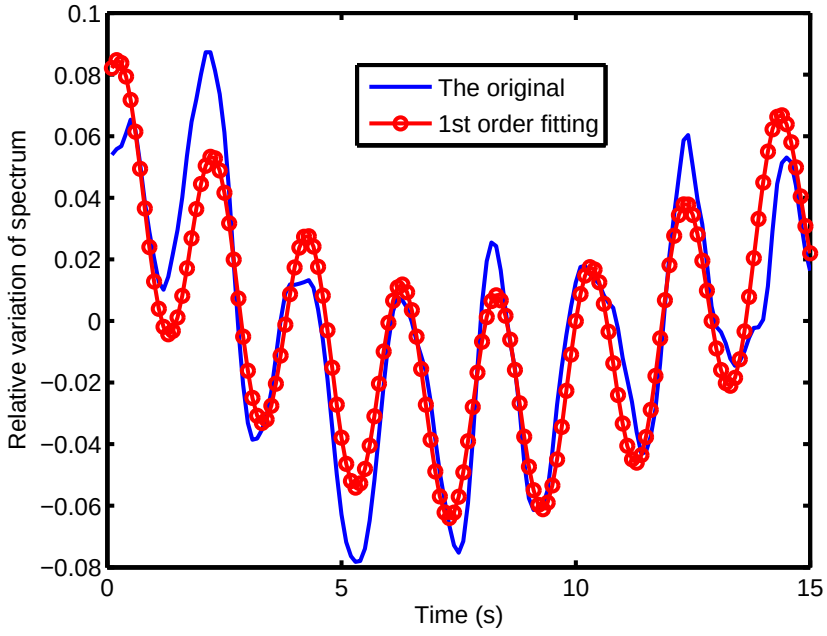

Figure 4.6: The group velocity effect on the numerical HMTF envelope with $k_1 a_1 = 0.01$

Specifically, the following functional form was used to describe the short wave spectrum at a specified wave number and sub-region:

$$\begin{aligned}\mathfrak{R}(k_s, X_n, t_i) \approx\ & b_{c0}(k_s, X_n) + b_{c1}(k_s, X_n)\sin(c_g(k_s)t_i) \\ & + b_1(k_s, X_n)\sin(k_1 X_n - \omega_1 t_i + \Phi_{01}(k_s, X_n)) \\ & + b_2(k_s, X_n)\sin(2k_1 X_n - 2\omega_1 t_i + \Phi_{02}(k_s, X_n)),\end{aligned} \tag{4.9}$$

where c_g denotes the group velocity of the short wave at wavenumber k_s. In equation (4.9), the real valued coefficients b_1 and Φ_{01} describe the amplitude and phase of a "first order" numerical MTF, while the coefficients b_2 and Φ_{02} are included to allow some description of "second order" effects. The coefficients b_{c0} and b_{c1} model an additive correction to account for the slow time evolution described previously. Other forms could be proposed as well, but the above definition appears to provide a reasonable means for extracting the portion of the spectrum modulation due to the long wave influence in the dataset utilized. Unknown coefficients were determined using a least-squares fitting procedure to the $\mathfrak{R}$ dataset; results were then averaged over sub-regions to obtain a final numerical value of the MTF (i.e. $\bar{b}_1(k_s)$). An alternative procedure involving a simultaneous fit to the data in all subregions was also considered; again the results were practically identical to those using the procedure described and are therefore not discussed further.

4.4 Numerical HMTF results

4.4.1 One long wave

According to the wave action HMTF theory, the first order coefficient $\bar{b}_1(k_s)$ should be directly proportional to $k_1 a_1$, and reference [28] shows that the second order coefficients should be proportional to $(k_1 a_1)^2$. Therefore the results illustrated will be normalized by these quantities.

Figure 4.7 plots normalized first and second order HMTF values ($\frac{\bar{b}_1(k_s)}{(k_1 a_1)}$ and $\frac{\bar{b}_2(k_s)}{(k_1 a_1)^2}$) obtained using $k_1 a_1 = 0.05$ and $k_1 a_1 = 0.10$. Results in the upper plot show the numerical $\bar{b}_1$ values to be approximately 4 in both long wave cases, with a difference from the value 4 on the order of 1% that depends weakly on k_s. The second order coefficient is in the range 7.-8.5, and shows a small decreasing trend as the long wave amplitude is increased.

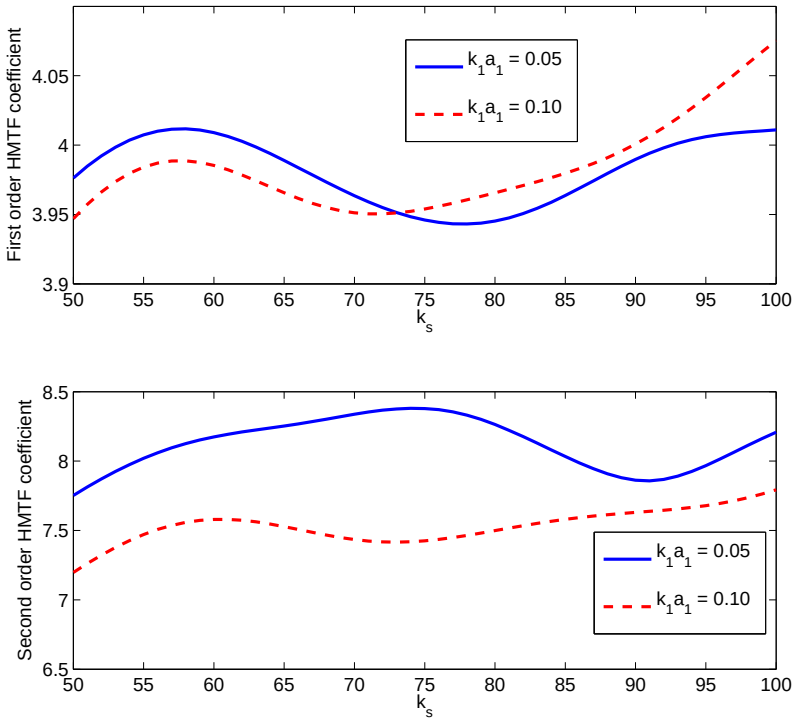

Figure 4.7: Numerically obtained normalized HMTF amplitudes

HMTF phases averaged over sub-regions ($\bar{\Phi}_{01}$ and $\bar{\Phi}_{02}$) are plotted in Figure 4.8. First order phase results in the upper plot show values near 0 degrees, with a very

weak dependence on k_s and a slight trend (to -2 degrees) versus the long wave amplitude. Second order phases are near -90 degrees, although the first order values obtained are in the range -92 to -94 degrees for the smaller long wave case, and near -98 degrees for the larger long wave case.

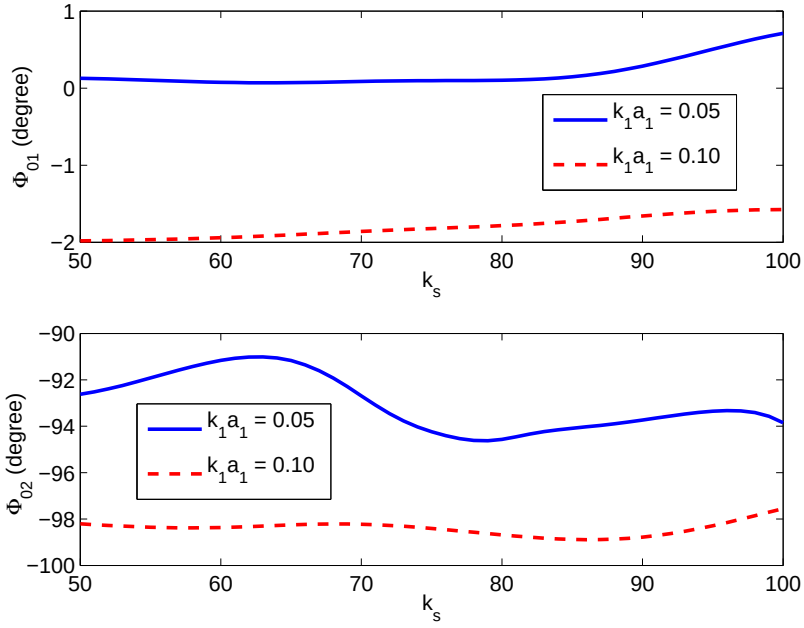

Figure 4.8: Numerically obtained HMTF phase

Although several potential sources of small errors exist in the values obtained, overall the numerical results indicate that the first order HMTF amplitude and phase are reasonably approximated as $4(k_1a_1)$ and 0 degrees in the data obtained, while the second order coefficient ($\bar{b}_2$) is reasonably (but less reasonably than the first order coefficient) approximated as $7.5(k_1a_1)^2$ with a phase of -90 degrees. While more detailed analyses could be conducted to increase confidence in the prediction of any

small deviations from these values, this basic information is sufficient for comparison with the first order wave action theory, as will be performed in Section 4.6.

4.4.2 Two long waves

Additional numerical simulations were performed for initial conditions with two deterministic long waves, using $(k_1, a_1) = (1, 0.07)$ and $(k_2 = 5, a_2 = 0.008)$. Figure 4.9 plots an example $\mathfrak{R}$, for $k_s = 60$ rads/m and in sub-region 18, and shows that more complicated trends versus time are observed due to the presence of multiple long waves. The wave action theory at first order predicts that these trends should be due to a simple summation of the first order effects from each long wave. Accordingly, the fitting function (equation (4.9)) was modified to include separate first and second order coefficients for the two long waves. Plots of the fit curves in Figure 4.9 show that the fit accuracy is somewhat improved when second order terms are included. The two obtained normalized first order MTF values averaged over spatial sub-regions are plotted in Figure 4.10, and again are found to be near 4. However the observed deviations from 4 are larger than those observed in the single long wave case, particularly for the k_2 wave. Again detailed numerical studies could be conducted to assess these small deviations, but the basic conclusion from this analysis is that the linear summation of first order contributions from each long wave in computing combined modulation effects appears reasonable.

4.5 A numerical study of the short wave dispersion relation

Modeling the effect of long waves on the dispersion relation of short waves is implicit in any wave action theory analysis of the HMTF. When short waves propagate over a slowly varying long wave or current, the short wave radian frequency ω is

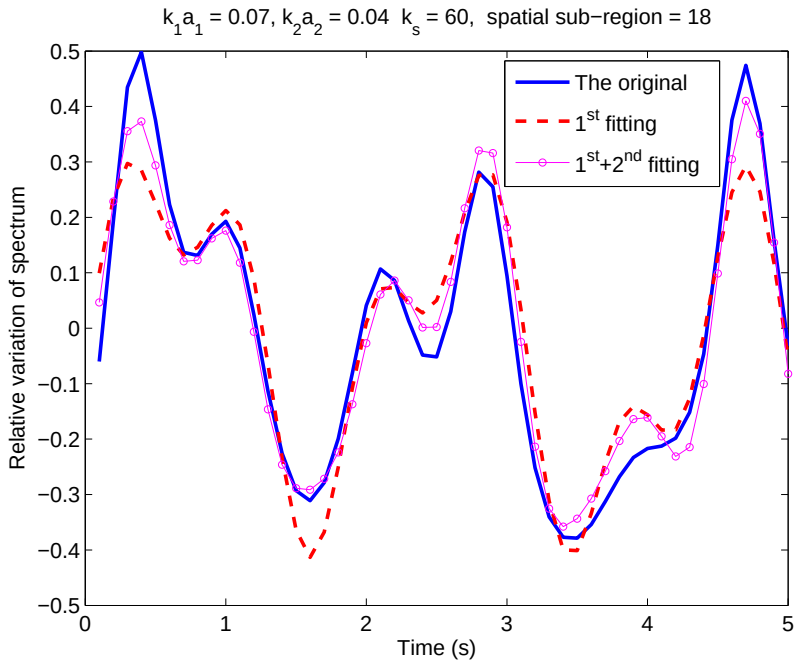

Figure 4.9: The fitting of HMTF versus k_s with $k_1a_1 = 0.07$ and $k_2a_2 = 0.04$

expected to undergo a Doppler shift [69, 70]:

$$\omega = \omega_s + \mathbf{k_s} \cdot \mathbf{U}, \tag{4.10}$$

where ω_s is the short wave frequency in the absence of Doppler shift effects and $\mathbf{U}$ is the underlying medium horizontal velocity with respect to the observer. Here the dot product describes the relationship between the direction of the orbital velocity and the short wave propagation direction.

To study this Doppler shift, a new dataset $\eta(x_q, t_i, M_j)$ was generated using $k_1 = 0.0625$ rads/m (wavelength and computational domain size 32π m). The long wave wavelength was extended in this case due to a desire to perform an additional temporal Fourier analysis of the short wave spectrum within a given sub-region; use of longer long-wave wavelengths results in an increased amount of time during which the long

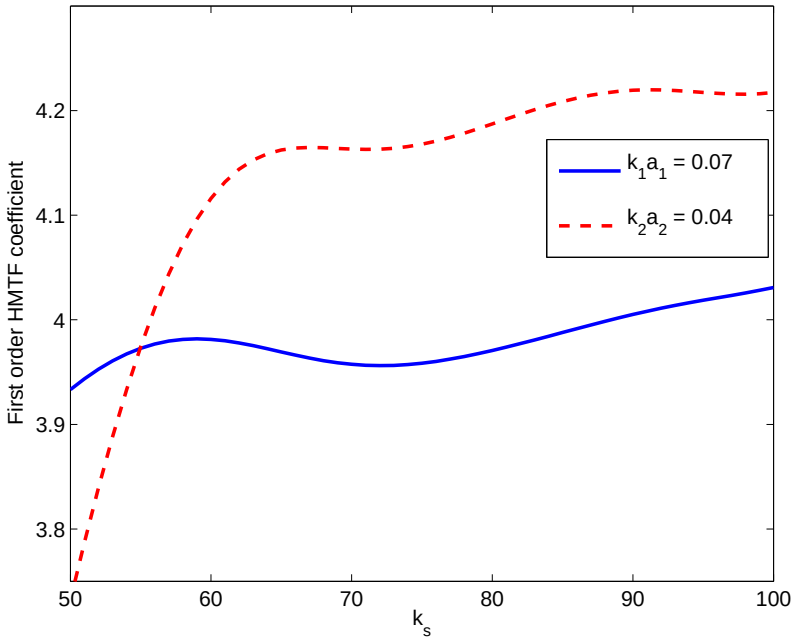

Figure 4.10: Numerically obtained normalized HMTF amplitudes with $k_1a_1 = 0.07$ and $k_2a_2 = 0.04$

wave phase remains relatively constant in a given spatial sub-region, so that the temporal Fourier analysis is more reasonable.

A time step of 0.002 sec was used in the hydrodynamic simulations, with a total time duration of 20.48 sec. The surface profile was discretized into 4096 points, and surface profile information was recorded every 0.04 sec so that 512 temporal samples are available during the time evolution. This time resolution is sufficient to capture the short wave temporal frequencies of interest. The short wave spectral range utilized in the simulations was $k_s \in [5, 15]$ rads/m. Other simulation parameters are similar to those described previously.

Analysis of the dataset is similar to that used previously, with the exception that only 15 spatial sub-regions were used. In addition, the complete time history of FFT outputs of the surface within each spatial sub-region were stored as the quantity $a(k_s, X_n, t_i, M_j)$; these are complex valued Fourier coefficients versus time in each sub-region. The 512 point time history of these Fourier coefficients was then divided into 15 overlapping time intervals labeled T_m through the use of Gaussian windows in time. An FFT of these localized time histories was then performed; the amplitude squared of this FFT output is then denoted as $\Omega(k_s, X_n, \omega_s, T_m, M_j)$, and includes the time history (on a long time scale T_m) of the radian frequency (ω_s) spectrum for the surface spectrum at wavenumber k_s in spatial subregion X_n. As in the previous analysis, this function can be ensemble averaged to eliminate the M_j dependence. Figure 4.11 shows the spatial variation of ensembled $\Omega(k_s, X_n, \omega_s, T_m)$ over realizations at given time sub-region.

Figure 4.12 illustrates ensemble averaged ω_s spectra versus time subregion T_m for the case $k_1 a_1 = 0.02$, $k_s = 10$ rads/m, and in several spatial sub-regions. The results

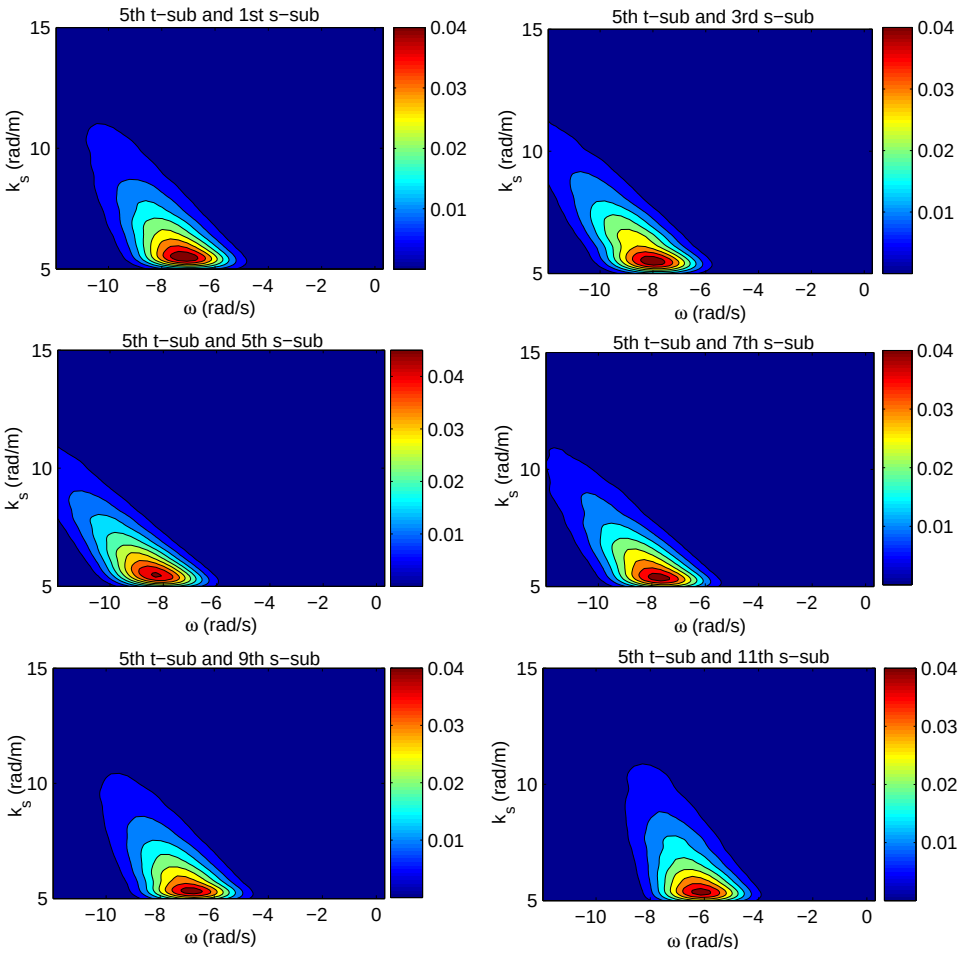

Figure 4.11: Variations of ensembled $\Omega(k_s, X_n, \omega_s, T_m)$ with $k_1 = 1/16$ and $k_1 a_1 = 0.02$

appear consistent with a modulation in the short wave dispersion relation due to currents produced by the long wave orbital velocity. However the observed ω_s spectra have non-zero width in frequency and also show variations in amplitude that are more complex than equation (4.10) alone.

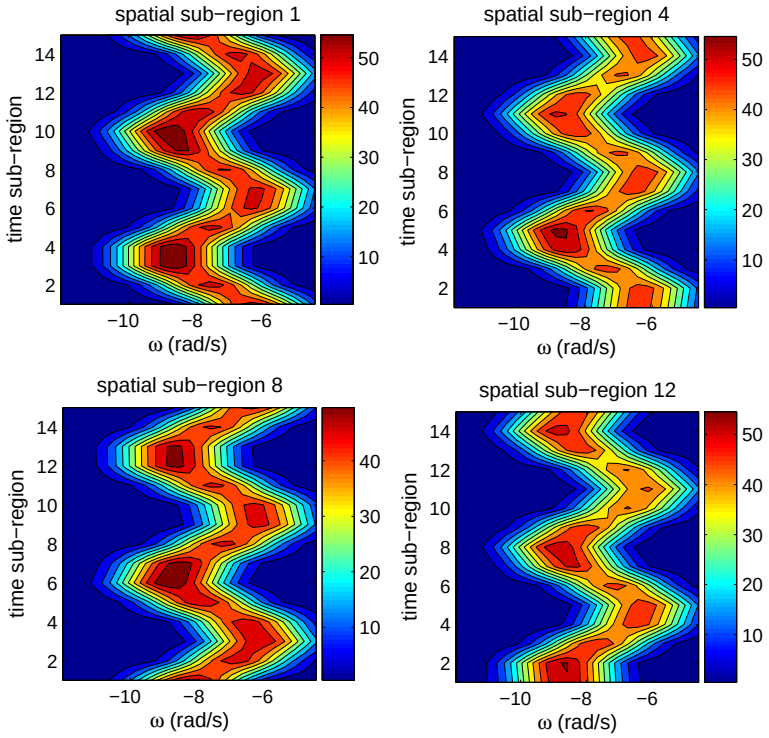

Figure 4.12: The trajectories of ω_s with $k_1 = 1/16$ and $k_1 a_1 = 0.02$

Using the ensemble averaged dataset $\bar{\Omega}(k_s, X_n, \omega_s, T_m)$, we identify the value of ω_s that maximizes $\bar{\Omega}(k_s, X_n, \omega_s, T_m)$ for all other parameters fixed as $P(k_s, X_n, T_m)$. A least squares fit to the obtained $P(k_s, X_n, T_m)$ values is then performed using

$$P(k_s, X_n, T_m) = a_0(k_s, X_n) + c_0(k_s, X_n)\sin(k_1 X_n - \omega_1 T_m), \tag{4.11}$$

where a_0 should be approximately ω_s from equation (4.10), and c_0 represents the amplitude of the modulation due to long waves. Results for the a_0 and c_0 coefficients are then averaged over spatial sub-regions (X_n) to obtain $\bar{a}_0(k_s)$ and $\bar{c}_0(k_s)$.

Assuming that the current in the dispersion relation can be represented by the first-order horizontal component of the long wave orbital velocity, the predicted value of ω can be written as

$$\omega \approx \omega_s + k_s \omega_1 a_1 \sin(k_1 x - \omega_1 t). \tag{4.12}$$

with $\omega_s = \sqrt{g k_s}$. Figure 4.13 plots the obtained coefficients normalized by their expected values (i.e. $\bar{a}_0(k_s)/\omega_s$ and $\bar{c}_0(k_s)/(k_s \omega_1 a_1)$); values near unity would indicate that the approximation of equation (4.12) is accurate. Results show the $\bar{a}_0$ term indeed to be well predicted by the theory, although the numerical results are slightly larger (by a factor less than 1%) than the prediction. The first order modulation however is significantly less (around 0.88) than the predicted unity value, indicating that equation (4.12) may neglect some important effects. Numerically obtained coefficients show a slight increasing trend versus k_s in both cases. Further dispersion studies were performed in an attempt to determine the source of the reduced numerical modulation compared to the first order theory. Results shows the offset between predictions to be near independent of $k_1 a_1$, so that the error is clearly at first order. To simplify the problem, simulations were also performed using a deterministic single-frequency short wave packet, localized spatially on the long wave in the initial conditions; results again showed a similar offset in obtained frequency modulations. Consideration of the analytical theory suggests that corrections to the ω_s term may be relevant, involving either modulations of the wavenumber or local acceleration effects [28] involved in the definition of ω_s. Further investigation of these differences will be performed in

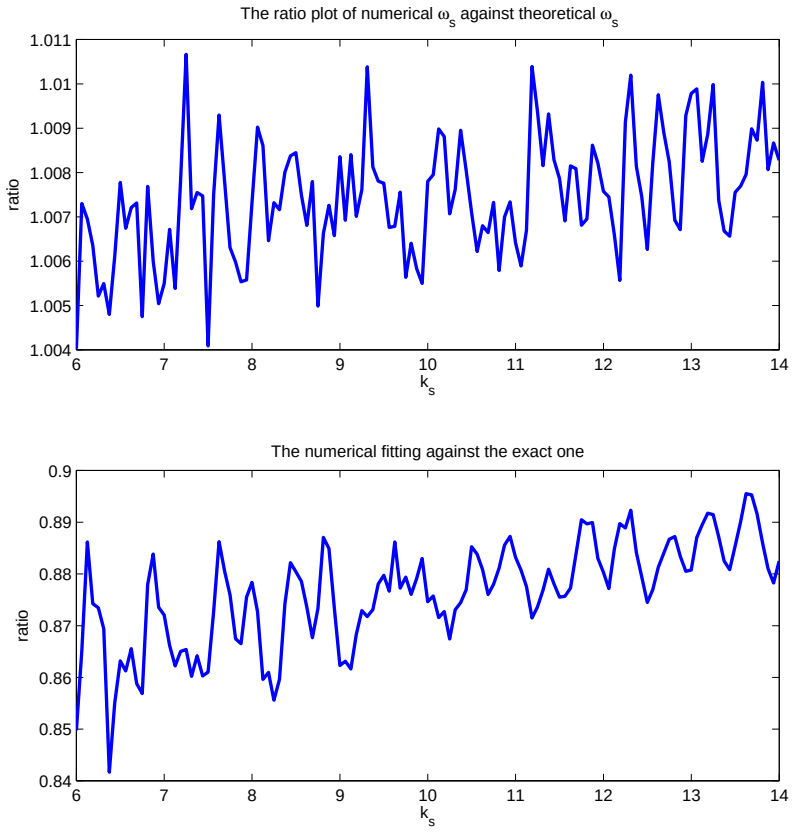

Figure 4.13: Normalized dispersion relation coefficients $\frac{\bar{a}_0(k_s)}{\omega_s}$ (upper) and $\frac{\bar{c}_0(k_s)}{(k_s\omega_1 a_1)}$ (lower) with $k_1 = 1/16$ and $k_1 a_1 = 0.02$

future studies. Overall the results show the standard first order prediction of the local frequency to have reasonable, but not complete, accuracy.

4.6 Wave action theory

The theory of wave action was developed for analysis of the evolution of a weakly nonlinear short wave "packet" as it propagates in an inhomogeneous background medium. The short wave packet consists of a narrowband set of waves centered around a carrier wavelength. In many water wave applications, the inhomogeneities encountered are current fields that vary slowly in space and/or time compared to the corresponding scales of the wave packet of interest. The concept of the conservation of wave action is based fundamentally on a separation of scales in both space and time, with packet properties described in terms of short scale wavenumber k_s and angular frequency ω_s parameters, while the slower variations are described in terms of x and t for space and time scales, respectively. The theory has been utilized to describe many phenomena of oceanographic interest, including the modulation of short waves by long waves relevant in this paper. Here we follow the first order solution of the wave action equation [25, 26, 28] developed to capture long-short wave modulation effects. While a numerical solution of the wave action equation (as in [71]) for the configurations of this paper could be pursued, such numerical solutions are far less frequently utilized in practice than the first order solution, and are therefore not considered further.

We also note that small differences in the form of the first order HMTF are observed in the literature, for example between [25] and [28]. These differences are partially explained by the inclusion of "heaving" effects due to the vertical component

of the long wave orbital velocity in [28], but also due to the neglect of a group velocity term in the zeroth order Lagrangian in [28]. While other authors [25, 26] do not include the former, these other authors are uniformly in agreement that the latter is necessary. We choose to follow the formulation of [26] in what follows.

The wave action quantity N here is defined as [70]

$$N(k_s, x, t) = \frac{S(k_s, x, t)}{\omega_s}, \tag{4.13}$$

where k_s is the local short wave wavenumber, $S(k_s, x, t)$ is the local short wave spectrum, and $\omega_s = \sqrt{gk_s}$ is the short wave radian frequency. For the purposes of this analysis, the wave action is modeled only for the short wave portion of the spectrum, and the dependencies on x and t result due to long wave effects that occur on the larger spatial and time scales. The analysis assumes that k and x are independent variables, although both depend on time.

Following [25, 26, 28, 70], an equation describing the conservation of wave action can be written as

$$\frac{dN}{dt} = Q, \tag{4.14}$$

where the differential operator d is the material derivative and operates along the characteristic or "ray" paths, while the term Q represents any sources or sinks of wave action. These include potential wind forcing, viscous damping, resonant nonlinear wave-wave interactions, or wave breaking [28] effects. Again in practice these terms are described primarily using empirical relations. The simulations performed include none of these sources or sinks with the exception of wave-wave interactions. However since no strong resonant interactions are expected in the simulations, the term Q is set to zero in the remaining analyses.

For long-short wave modulation studies, it is convenient to rewrite equation (4.14) in phase space:

$$\frac{\partial N}{\partial t} + \dot{x}\frac{\partial N}{\partial x} + \dot{k_s}\frac{\partial N}{\partial k_s} = 0. \tag{4.15}$$

where the dot denotes the derivative with respect to time. The "ray" equations that describe the evolution of the canonical variables x and k_s are:

$$\dot{x} = \frac{\partial \omega}{\partial k_s} = c_g + U \tag{4.16}$$

$$\dot{k_s} = -\frac{\partial \omega}{\partial x} = -k_s\frac{\partial U}{\partial x}, \tag{4.17}$$

where $c_g = \frac{1}{2}\sqrt{\frac{g}{k_s}}$ is the short wave group velocity for the wavenumber considered, and U is the horizontal component of the long wave orbital velocity.

4.6.1 Determination of HMTF

Following [25, 26], a perturbative solution to first order is sought. A description of the long wave orbital velocity consistent with this goal is

$$U = \omega_1 a_1 \sin(\Phi) \tag{4.18}$$

where $\Phi = k_1 x - \omega_1 t$ denotes the long wave phase.

Because it is modulations of the spectrum, not of wave action, that are of interest in the studies of this paper, the substitutions

$$\frac{\partial N}{\partial t} = \frac{1}{\omega_s}\frac{\partial S}{\partial t} \tag{4.19}$$

$$\frac{\partial N}{\partial x} = \frac{1}{\omega_s}\frac{\partial S}{\partial x} \tag{4.20}$$

$$\frac{\partial N}{\partial k_s} = \frac{1}{\omega_s}\frac{\partial S}{\partial k_s} - \frac{c_g}{\omega_s^2}S \tag{4.21}$$

$$= -\frac{S}{\omega_s k_s}\left[m + \gamma_s\right] \tag{4.22}$$

are utilized to recast equation (4.15) in terms of the short wave spectrum alone; equation (4.22) holds when it is assumed that the spectrum assumes the form $\bar{S} \propto \bar{k}_s^{-m}$ as given in equation (4.5). The quantity $\gamma_s(k_s)$ is given by $\frac{c_g(k_s)}{c_p(k_s)}$, where c_g and c_p are the group and phase velocities of the short wave considered, respectively; for purely gravity waves, $\gamma_s = 0.5$. Note it is assumed in equation (4.19) that the value of ω_s used in the denominator of the wave action definition is independent of time; this will be considered further below.

Substituting the above equations into equation (4.15) and combining with equations (4.16)-(4.17) yields

$$\frac{\partial S}{\partial t} + c_g \frac{\partial S}{\partial x} = -U \frac{\partial S}{\partial x} - [m + \gamma_s] S \frac{\partial U}{\partial x} \tag{4.23}$$

A perturbation solution is now performed, in which the orbital velocity U is assumed to be the small parameter. Writing

$$S = S^{(0)} + S^{(1)} + \cdots \tag{4.24}$$

yields at zeroth order

$$\frac{\partial S^{(0)}}{\partial t} + c_g \frac{\partial S^{(0)}}{\partial x} = 0 \tag{4.25}$$

The above can be transformed into an ordinary differential equation by introducing the variables

$$\alpha = x - c_g t \tag{4.26}$$

$$\beta = x + c_g t \tag{4.27}$$

to obtain

$$\frac{\partial S^{(0)}}{\partial \beta} = 0 \tag{4.28}$$

The solution to this equation is that $S^{(0)}$ is constant in β, while remaining arbitrary in α. However if an initial condition of the zeroth order solution is chosen that is independent of x at time zero (as is appropriate for the studies described here), the result is that $S^{(0)}$ is independent of x and t.

Continuing to first order, the relevant equation is

$$\frac{\partial S^{(1)}}{\partial t} + c_g \frac{\partial S^{(1)}}{\partial x} = -\left[m + \gamma_s\right] S^{(0)} \frac{\partial U}{\partial x} \tag{4.29}$$

with the linear term in U vanishing due to the constant nature of $S^{(0)}$. Substituting the specified form for U, and again making use of the variable transformation described previously allows this equation to be solved. The result is

$$S^{(1)} = k_1 a_1 \sin(\Phi) \frac{\left[m + \gamma_s\right]}{1 - \frac{c_g}{c_1}} S^{(0)} \tag{4.30}$$

where $c_1 = \sqrt{\frac{g}{k_1}}$ is the long wave phase velocity.

Because $S^{(1)}$ above is directly proportional to $\sin\Phi$, the predicted HMTF can now be determined in terms of

$$\frac{S^{(1)}}{S^{(0)} \sin(\Phi)} \tag{4.31}$$

with the magnitude and phase of this quantity defined as R_1 and Φ_1, respectively. Substituting equation (4.30) in equation (4.31) and solving yields

$$R_1 = (k_1 a_1) \frac{\left[m + \gamma_s\right]}{1 - \frac{c_g}{c_1}} \tag{4.32}$$

$$\Phi_1 = 0 \tag{4.33}$$

This HMTF prediction is identical to that in [26].

Although only a single long wave was considered in this derivation, the linear nature of the first order solution ensures that the combined effect of two long waves to first order is simply the sum of their individual contributions.

4.6.2 Comparison with numerical simulations

For the numerical simulations performed, the spectrum utilized had a k_s^{-3} dependence, yielding $m = 3$ for use in equation (4.32). In addition, the value of γ_s is 0.5 for gravity waves, so that the predicted value of R_1 can be simplified to

$$(k_1 a_1) \frac{3.5}{1 - \frac{1}{2}\sqrt{\frac{k_1}{k_s}}} \tag{4.34}$$

Factoring out $k_1 a_1$ as in Figure 4.7, the remaining coefficient ranges from a value of 3.766 at $k_s = 50$ rads/m to 3.684 at $k_s = 100$ rads/m with $k_1 = 1$ rad/m, compared to the observed values near 4 from the numerical simulations (Figures 4.7 and 4.10). The predicted phase of zero degrees is well matched by the numerical simulations.

Although further studies of the differences between the numerical and analytical models could be performed, overall the results indicate that the first order HMTF derived from wave action theory yields reasonable (within 10%) predictions of short wave modulations by longer sea waves. It is noted that this difference remains consistent even as the long wave amplitude is decreased; this fact motivates continued studies to improve upon the wave action theory formulation applied here.

One possible correction involves inclusion of time variations in ω_s in computing the time derivative of the wave action, so that

$$\frac{\partial N}{\partial t} = \frac{1}{\omega_s}\frac{\partial S}{\partial t} - \frac{c_g}{\omega_s^2} S \frac{\partial k_s}{\partial t} \tag{4.35}$$

as opposed to equation (4.19). The result of this modification is a change in the value 3.5 in equation (4.34) to 4; the final predicted HMTF values now exceed 4 by 5 to 8%, whereas the original values were less than 4 by similar percentages. Therefore no clear improvement results from this change.

A second possible correction involves the inclusion of local acceleration effects as described in [28]. In this case, the gravitational acceleration is modified along the long wave by the vertical long-wave acceleration; this change in the local gravitational acceleration is modeled by introducing an additional $-\frac{\partial \tilde{\omega_s}}{\partial x}$ term on the right hand side of equation (4.17). The local frequency is given by

$$\tilde{\omega_s} \quad = \quad \sqrt{\tilde{g} k_s} \tag{4.36}$$

within which only $\tilde{g}$ is considered a function of x. The method for determining the local gravitational acceleration $\tilde{g}$ is described in [28]. Following this process results in a change in equation (4.34) to

$$(k_1 a_1) \frac{3.5 \left(1 + \frac{1}{2}\sqrt{\frac{k_1}{k_s}}\right)}{1 - \frac{1}{2}\sqrt{\frac{k_1}{k_s}}} \tag{4.37}$$

which varies from 4.033 at $k_s = 50$ rads/m to 3.87 at $k_s = 100$ rads/m when normalized. Although these values are closer to those obtained numerically, the inclusion of local acceleration effects in fact increases the error in the short wave dispersion relation fits described in Section 4.5. For this reason, the modeling of local acceleration effects used here cannot be considered completely validated.

While further extensions of the wave action theory to include other effects or second order contributions for comparison with the second order numerically obtained results are possible, the first order theory described here is most commonly used in practice, and is the most relevant in applications. Further examinations of improvements to the wave action theory are left for future work.

4.7 Concluding remarks

A numerical study of the modulation of short sea waves by longer waves was performed in order to provide an assessment of the first order "hydrodynamic modulation transfer function" (HMTF) commonly used in remote sensing of the sea. The use of numerical simulations allowed examination of the theory in a controlled environment, without need for empirical models of effects such as wind forcing and wave breaking. Results show the first order HMTF to provide a reasonable prediction of the short wave modulations observed in the numerical simulations. Numerical results also show the basic applicability of the standard Doppler shifted dispersion relation in the cases considered. However in both of these areas, differences on the order of 10% from the commonly used analytical theories were encountered, indicating that revisions to the standard first order forms may be possible to yield improved predictions.

Future work will include further analysis of the basic wave action theory formulation and its first and second order HMTF predictions, as well as more detailed numerical simulations over a wider range of short and long wave environments. The numerical procedures presented here should be applicable to such studies with only minor modifications.

CHAPTER 5

STUDIES OF OCEAN WAVE-RADAR MODULATION MECHANISMS - INCLUSION OF THE THIRD-SCALE EFFECT

5.1 Introduction

It is well-known that electromagnetic backscattering from the sea surface varies spatially and temporally. For a stationary imaging radar or scatterometer, there are two basic mechanisms for cross section variations that are usually considered: those due to "tilt" effects and those due to hydrodynamic effects. Tilt effects are due to local incidence angle changes caused when the short Bragg waves, which are important for radar scattering, are observed along "tilted" portions of longer sea waves. Such variations for radars whose range resolution is smaller than the scale of longer sea waves are described through the use of a power modulation [72], including the tilt modulation and the strain modulation (later called hydrodynamic modulation). The power modulation is also described by a radar modulation transfer function (RMTF) [25], which includes radar tilted MTF (RTMTF) due to the local incidence change and radar HMTF (RHMTF) due to hydrodynamic modulation for short Bragg waves. The definition of RMTF in [25] is slightly different from that given in [72]. A complete theoretical description of RMTF is summarized in [39].

Numerous ocean radar experiments have been conducted to investigate the ocean wave-radar MTF at different radar frequencies and polarizations, for example, X-band VV polarization [72, 73], X- and L-band [74, 38], K_a-band dual polarization [75], X- and K_a-band dual polarization [33], L- and K_u-band [34], C-band [35, 76], L-, C-, and X-band [36]. The results of those experiments show that the RHMTF inferred from the experimental RMTF is larger than the pure HMTF predicted by the wave action theory [27, 24, 40, 36, 76], and the inferred RHMTF is polarization dependent [24, 40, 36]. Theoretically, the mapping from the pure HMTF to the electromagnetic RHMTF is linear. Therefore, the RHMTF is polarization independent [38]. The third-scale (the intermediate scale) modulation is considered to explain this discrepancy between the theoretically predicted RHMTF and the experimentally derived RHMTF [27, 24, 40, 36]. Besides these experimental studies, an approximate numerical electromagnetic integral equation method was used to study the RMTF [41], where the RHMTF was approximately treated by the wave action theory [25]. Both experimental and numerical results demonstrated that the intermediate scale waves have an effect on the RMTF, since the intermediate waves are hydrodynamically modulated by the presence of long waves. Such modulation results in those intermediate waves being distributed locally. Therefore, the intermediate waves introduce the second "tilt" and "heave" effect on the Bragg waves.

The numerical study of HMTF based on the exact nonlinear hydrodynamic equation was reported in [77] (see Chapter 4). This progress enables us to apply computational electromagnetics to the modulated ocean surfaces to study the RMTF, because such a long and short wave surface inherently includes both the RTMTF and the RHMTF. Then, we can study the RHMTF further only by filtering out long wave

components from the long and short wave surface. Furthermore, the intermediate waves influence on the RMTF was able to be studied through varying short wave spectral contents. This idea is realized and implemented in this chapter.

The methodology of the numerical study of ocean wave radar modulation mechanisms by inclusion of the third scale effect is described in Section 5.2. To explain and compare our numerical results, we derive an analytical ocean wave-radar MTF based on the two-scale electromagnetic model in Section 5.3. In order to further discuss the intermediate waves' ms slope influence on MTF, an empirical model based on RCS expansion along the surface slope and the statistical two-scale model which depends on the surface slope, are presented to analyze the intermediate waves' effect on MTF. Consequently, the RMTF results and discussions are shown in Section 5.4. Section 5.5 concludes this chapter.

5.2 Methodology

This section describes the procedure of the numerical study of the ocean-wave RMTF from a sea surface. This procedure includes five steps. In the first two steps, we need to generate time-varying modulated ocean surfaces and to compute the backscattering fields by use of numerical scattering integral equation methods. In the third step, the RCS dataset is obtained from the ensemble average of the backscattering fields calculated in the second step. In the fourth step, by use of the least square method, the RMTF and RHMTF are extracted from the RCS dataset. The final step is to calculate the RTMTF from RMTF and RHMTF data.

5.2.1 Nonlinear surfaces generation

The entire surface generated in this step, which is utilized to study the RMTF, includes both long and short waves. Then, the long wave components can be filtered out from this entire surface. Only the short wave surface is used to study the RHMTF.

The nonlinear ocean surfaces which are utilized in this numerical RMTF study is assumed to be a one-dimensional fluid surface of infinite depth. We also assume that the fluid is incompressible and inviscid; surface tension effects are also neglected. The surface elevation is denoted as $z = \eta(x,t)$ and the surface velocity potential as $\phi(x,t)$, where x, z are the horizontal and vertical space coordinates, respectively, and t represents time. The evolution of these two quantities is determined by the following equations [29]

$$\phi_t = -g_0\eta - \frac{1}{2}\phi_x^2 + \frac{1}{2}\phi_z^2[1+\eta_x^2], \tag{5.1}$$

$$\eta_t = -\phi_x\eta_x + \phi_z[1+\eta_x^2], \tag{5.2}$$

where the subscript denotes the associated derivative and g_0 is the gravitational acceleration (9.8 m/s^{-2}).

We solve equations (5.1-5.2) using the pseudo-spectral method of [29], and retain terms up to the 2nd order (two nonlinear order) in the slope expansion. The initial condition for this numerical simulation consists of a deterministic long wave and a band-limited stochastic "Pierson-Moskowitz" (PM) short waves. The short PM wavenumber bandwidth is $[31, 400]$ rad/m (due to the numerical stability issue, we cannot run equations (5.1) and (5.2) with a very broad spectrum), and the steepness of the long wave is 0.05 with a unit wavenumber. The ocean surface wind speed is at 19.5 m is 3 m/s. The speed value does not have a direct effect on our numerical

MTF study. The reason that we choose a low value is to have good numerical stability. The total recorded data duration is 4 s with a sampling time step 0.1 s. The surface discretization number is 2048 with a length $Ls = 2\pi$ m. The recorded data is $\eta(x_i, t_j, r_m)$, where x_i denotes the spatial coordinate, t_j denotes the time coordinate, and r_m denotes the realization identification number.

5.2.2 Electromagnetic scattering models

Electromagnetic backscattering fields of both HH and VV polarizations are computed from the electrical field integral equation (EFIE) and magnetic field integral equation (MFIE), respectively, in this study. With a transformation, the EFIE can be converted into a MFIE [56]. Therefore, both electric and magnetic field integral equations can be written with a generalized magnetic field integral form as [46, 55, 56]

$$\begin{aligned}\mathbf{J}(x,t,r_m) = \mathbf{J}^{inc}(x,t,r_m) + \int_{-\infty}^{x} dx' G(x',x)\mathbf{J}(x',t,r_m) \\ + \int_{x}^{\infty} dx' G(x',x)\mathbf{J}(x',t,r_m),\end{aligned} \tag{5.3}$$

where $\mathbf{J}^{inc}$ is the generalized incidence current, $\mathbf{J}$ is the unknown induced generalized current, $G(x', x)$ is the generalized Green function, which is written with

$$\begin{cases} -\frac{ik}{4}\frac{H_1^{(1)}(kd)}{d}\sqrt{\frac{1+\eta_x(x',t,r_m)^2}{1+\eta_x(x,t,r_m)^2}}[-\eta_x(x,t,r_m)(x-x') + \eta(x,t,r_m) - \eta(x',t,r_m)] \\ \quad \text{for HH polarization} \\ \frac{ik}{4}\frac{H_1^{(1)}(kd)}{d}[-\eta_x(x',t,r_m)(x'-x) + \eta(x',t,r_m) - \eta(x,t,r_m)] \\ \quad \text{for VV polarization,} \end{cases}$$

where $d = \sqrt{(x-x')^2 + (\eta(x,t,r_m) - \eta(x',t,r_m))^2}$, x' and x are the source point and the field point, respectively, and $H_1^{(1)}$ is the first order Hankel function of the first kind. With the generalization form (see equation (5.3)), the original first kind Fredholm integral equation of the EFIE can be converted into the second kind Fredholm integral equation. This conversion improves the iteration convergence rate. Equation (5.3)

can be effectively solved with a method called "Forward-Backward" (FB) [55] or a method called the method of ordered multiple interactions (MOMI) [46]. The MOMI is used in this study to solve equation (5.3). In combination with the spectral acceleration method [47, 57], the overall numerical operation is about $O(N)$ for both solving and saving count. The MOMI iteration convergence threshold is defined as $\sqrt{|\mathbf{J}_{l+1} - \mathbf{J}_l|^2/|\mathbf{J}_l|^2}$, where the subscript l denotes the iteration step, and the threshold is 0.001 in this study. The total MOMI iteration requires only about two steps to converge to this threshold for each backscattering computation. Once $\mathbf{J}$ is known, the backscattering fields of both HH and VV polarization can be obtained with a near-field integral [56].

5.2.3 RCS dataset calculation and tapering issues

In reality, we have difficulties running a surface with an infinite length. Alternatively, a truncated surface with a finite length is applied in our numerical computation. In order to minimize the truncated edge effects and to compute the localized scattering field, a tapered incident wave is chosen in this study [53]. Increasing the tapering parameter g enables the radar to collect the backscattering mainly from a very narrow local surface element. The remainder of this subsection describes details of tapering issues.

Tapering configuration

The scattering fields for both polarizations are computed from each time step t_j and realization r_m surface $\eta(x, t_j, r_m)$. Figure 5.1 illustrates the far-field scattering at one time step surface. Figure 5.1, (a) shows the tapered incidence waveform; (b) shows the far-field scattering from the long and short wave surface and the computed

RCS dataset is used to study RMTF; (c) shows the scattering from the short waves ($k_s \in [40, 380]$ rad/m) only surface, and its RCS dataset is used to study the RHMTF, which includes both short waves and intermediate waves; (d) shows the scattering from the short waves ($k_s \in [k_c, 380]$ rad/m) only surface, where k_c is the cutoff wavenumber close to the Bragg wavenumber and is given in Table 5.1, and its RCS dataset is used to short waves only RHMTF. The reason for choosing a large k_c is to minimize the intermediate waves' effect.

θ_i (degree)	k_B (rad/m)	k_c (rad/m)
20	87.5	70
25	108.2	80
30	128.0	110
35	146.8	120
40	164.6	140
45	181.0	150
50	196.1	170
55	209.7	180
60	221.7	195

Table 5.1: The low cutoff wavenumber in the HMTF computation

Simulation parameters

The electromagnetic incidence wave number k_i is chosen as 128 rad/m. This means that the total ocean surface length equals 128 electromagnetic wavelength λ. The incidence angles vary from 20^0 to 60^0 with a stepsize 5^0. The valid truncated ocean wave number is within $[1, 9]$ rad/m for long waves and $[40, 380]$ rad/m for short waves. The gap between 9 rad/m and 40 rad/m is due to the initial truncation.

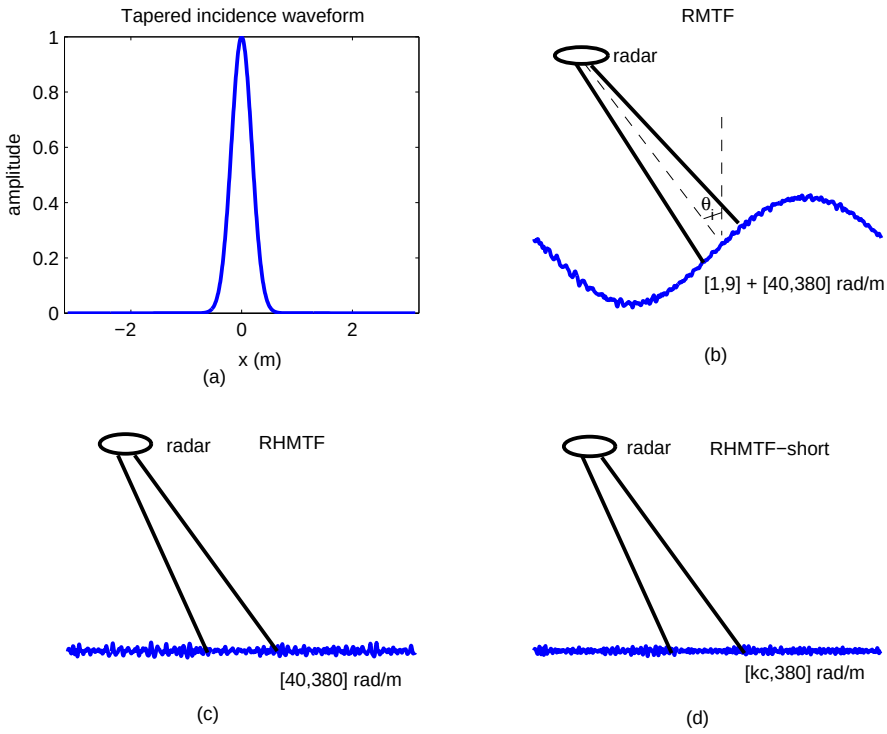

Figure 5.1: Illustrations of electromagnetic scattering simulations in this study

The single long wave will evolve into a Stokes wave using equations (5.1) and (5.2). Thus, even with a single initial long wave, the surface includes many long waves after time evolution. Among them, only the first- and second-order long wave modes are important to the study of modulation, since the amplitude of the other modes are much smaller than that of the first order and second order. Therefore, 9 rad/m is a relatively large value. The difference of the RMTF obtained from the cutoff 3 rad/m and the cutoff 9 rad/m should be negligible.

The high cutoff k_c is about $3k_0$, which is close to the suggested values [78, 23]. Further investigation on high cutoff with [300, 350, 390] rad/m is studied. The modulated RCS results given by the 300 rad/m are slightly different from those given by the other two cutoffs. The difference between RCS given by cutoff 350 rad/m and that given by 390 rad/m is negligible. Furthermore, the incidence angles that we studied are far from the low-grazing. Therefore, the high cutoff 380 rad/m is a reasonable value.

Tapering g determination

Theoretically, we expect that the simulated surface has a large length Ls, for example, $Ls > 1000\lambda$, and that a beam incidence is very narrow, for instance, $g/Ls << 1$. It is known that the surface length Ls with a hundred electromagnetic wavelengths is enough for small to moderate incidence angles [79]. If the incidence angle tends to LGA, the required surface length increases dramatically. Due to the hydrodynamic code limitation, we choose $Ls = 128\lambda$. Then, the remaining question is how to determine a reasonable g. A smaller g can cause a larger numerical error [56], therefore, three different g choices are used to find a reasonable value.

A linear band-limited ($k \in [k_i/4, 4k_i]$) PM surface with $U_{19.5}$ =3 m/s and $Ls = 128\lambda$ is utilized to test the reasonable Ls and g. Figure 5.2 shows the ensemble averaged RCS variations over incidence angles from 20^0 to 80^0 with $g = Ls/6, Ls/12, Ls/24$. Since this simulated surface is very smooth with respect to λ, the SPM solutions are also shown for comparison. Comparison results demonstrate that 128λ with a tapering $g = Ls/24$ is a reasonable setting for incidence θ_i between 20^0 and 60^0. A further validation from nonlinear surfaces backscattering at $\theta_i = 40^0$ is shown in Figure 5.3. Again, the result shown in this figure supports that $Ls = 128\lambda$ and $g = Ls/24$ are reasonable values.

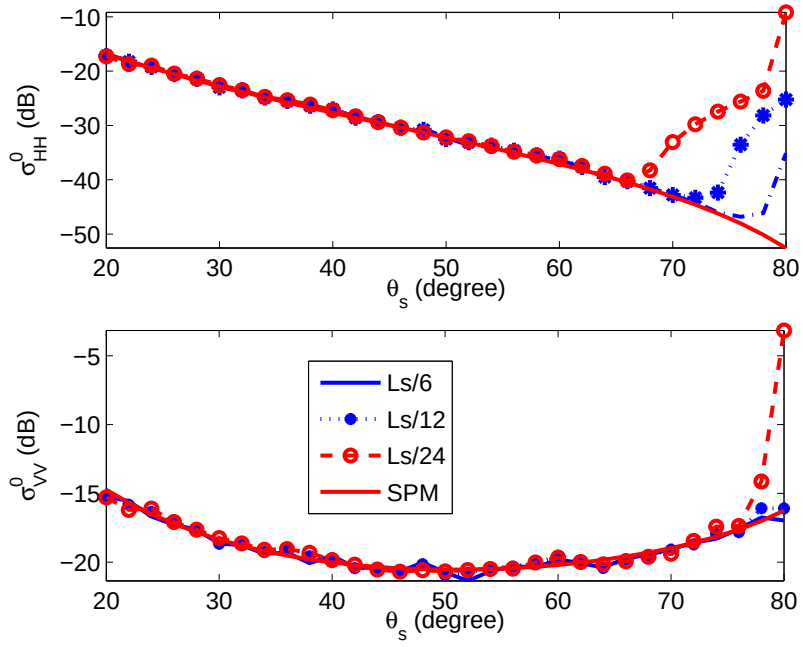

Figure 5.2: The RCS comparison of different tapering g for linear surfaces with $L_s = 128\lambda$

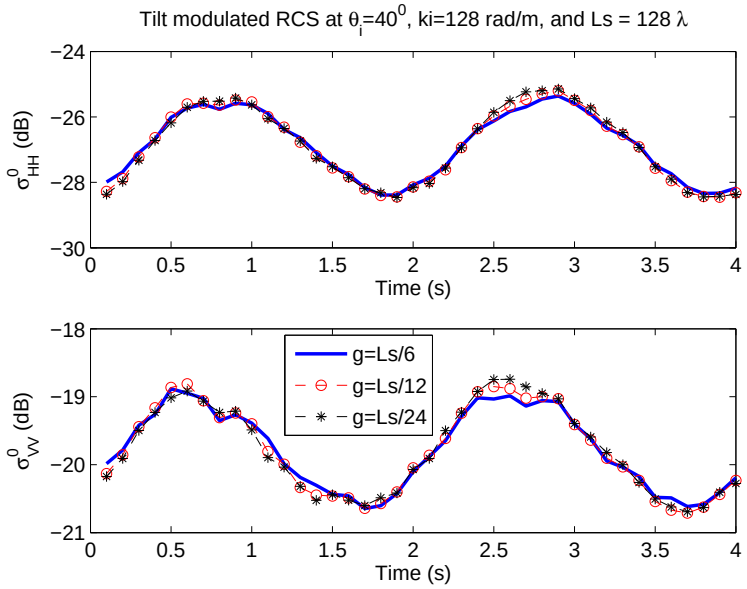

Figure 5.3: The RCS comparison between different tapering g for nonlinear long wave and short wave surfaces at $\theta_i = 40^0$

Theoretical convergence with varying g

From Figure 5.3, we find that the RCS variation is larger with a narrower tapering window, i.e., a smaller incidence spot size. Numerically, we have difficulties in running a much smaller g. The question which arises is how a smaller g influences the tapering convergence. In order to answer this question, we study an ideal case where a sinusoidal time varying surface multiplies with a Gaussian tapering. The Gaussian tapering is an approach to the Gaussian-like tapering used in this study. The ideal convergence rate is plotted in Figure 5.4. In this figure, the tapered incident waves vary with different g. The purpose of this multiplication is to obtain the numerical surface slope. Results in Figure 5.4 demonstrate that the slope with the taper parameter $g = Ls/24$ is very close to its exact value, and the local tapering algorithm has

an exponential convergence rate. In addition, the numerical MTF convergence rate (exponential convergence), which is obtained from the nonlinear modulated surfaces, is plotted in Figure 5.5. The result in this figure supports that a narrower tapering has a larger MTF coefficient. However, within each illumination spot, there must be enough Bragg waves, which enables us to obtain the correct RCS. Thus, g can not be very small.

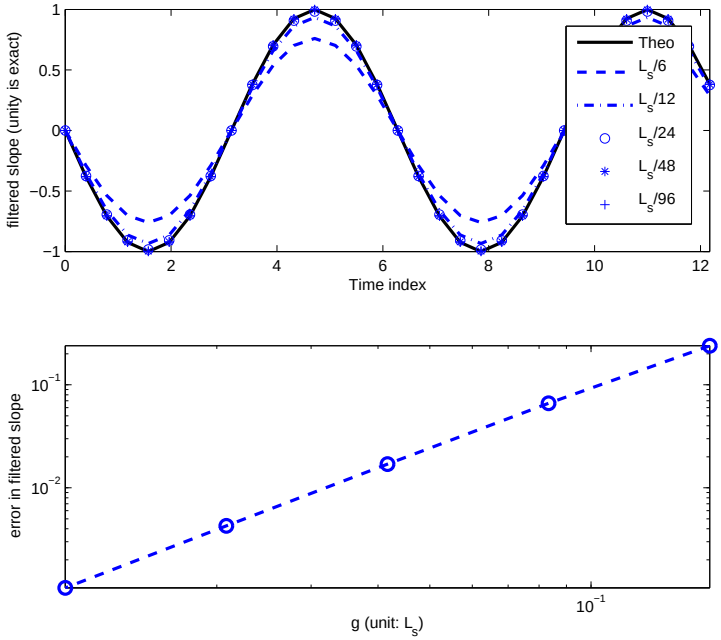

Figure 5.4: Theoretical Gaussian tapering convergence illustration from a sinusodial surface

Further validation for Ls and g from nonlinear surfaces

Upon g and Ls determined, we further examine how well these parameters perform in the entire surface ensemble-averaged RCS compared to the analytical SPM solution.

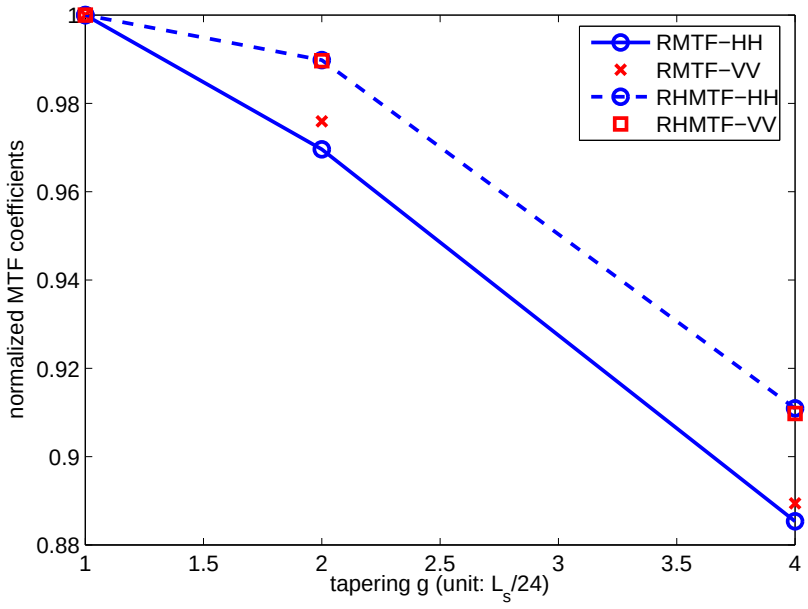

Figure 5.5: The convergence of different tapering g in the nonlinear scattering computation at $\theta_i = 40^0$

We utilized 1600 Monte-Carlo simulations. The average over time duration is 4 s (about 2 periods). The polarized ensemble-averaged RCS obtained from numerical simulations and from the small perturbation model (SPM) (equations (5.9) and (5.10)) are shown in Figure 5.6. In this figure, the short wave only surface has a low cutoff, given in Table 5.1, and the entire surface has a low cutoff 40 rad/m. The numerical RCS of VV polarization matches very well with that predicted by the SPM in the cases with/without long waves. In particular, this figure also shows that the RCS of HH polarization from the entire surface is larger than that from the short waves only surface because the intermediate waves between the 40 rad/m and the cutoff value given in Table 5.1 make some contribution to short Bragg waves. Further discussion is provided in Section 5.4.2.

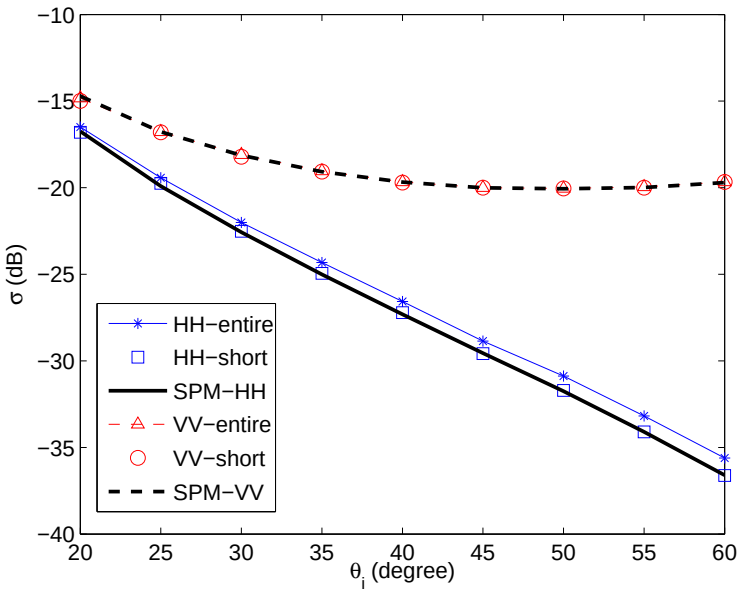

Figure 5.6: The ensemble-averaged RCS comparison

5.2.4 Numerical extraction of RMTF/RHMTF

At each time t_j and realization r_m, we compute the backscattering field for both polarizations once using the tapered incident wave, and obtain a complex scattering field $f_{pp}(t_j, r_m)$, where the subscript pp denotes polarization status. The RCS of each polarization is computed from the scattering field data as

$$\sigma_{pp}(t_j) = \langle |f_{pp}(t_j, r_m) - \langle f_{pp}(t_j, r_m) \rangle|^2 \rangle, \tag{5.4}$$

where the ensemble average $\langle\rangle$ is over realizations. Then, we obtain the time varying polarized RCS $\sigma_{pp}(t_j)$ (see Figure 5.3).

The MTF describes the variation of the RCS over time and/or space. Therefore, the numerical MTF can be extracted from the RCS dataset. The least square fitting

formula is utilized to extract the MTF [77]

$$\begin{aligned}\frac{\sigma_{pp}(t_i)}{\overline{\sigma}_{pp}} &= c_0 + c_{11}\sin(-c_g(k_B)t) + c_{12}\cos(-c_g(k_B)t) \\ &+ c_{21}\sin(\Phi(t)) + c_{22}\cos(\Phi(t)) \\ &+ c_{31}\sin(2\Phi(t)) + c_{32}\cos(2\Phi(t)),\end{aligned} \tag{5.5}$$

where $\overline{\sigma}_{pp}$ denotes the average of $\sigma_{pp}(t_i)$ over time, $\Phi(t) = -\sqrt{g_0}t$, and $c_g(k_B)$ is the group velocity of short Bragg wave with $k_B = 2k_i\sin(\theta_i)$. Then, the amplitude and phase of the first-order RMTF (or RHMTF) coefficient are given by

$$R_1 = \sqrt{c_{21}^2 + c_{22}^2}, \tag{5.6}$$

$$\psi_1 = \arctan(c_{22}/c_{21}). \tag{5.7}$$

Although equation (5.5) includes the second-order effect, it is very small with respect to the first order (see Figure 5.7). Therefore, we analyze only the first-order RMTF and RHMTF.

The equation (5.5) is used to extract RMTF from the RCS dataset of the entire surface. The amplitude R_p^M and phase Φ_p^M of RMTF are computed with use of equation (5.6) and (5.7), respectively. The subscript p denotes polarization. The RHMTF amplitude R_p^H and phase Φ_p^H are computed from the RCS dataset generated from the short wave only surfaces.

5.2.5 Numerical calculation of RTMTF

Since the entire surface and the short wave only surface have the same short wave components at each time and realization, we assume that the RHMTF from the entire surface and the RHMTF from the short wave surface are equivalent to each other. Therefore, based on the assumption that the total RMTF consists of RHMTF

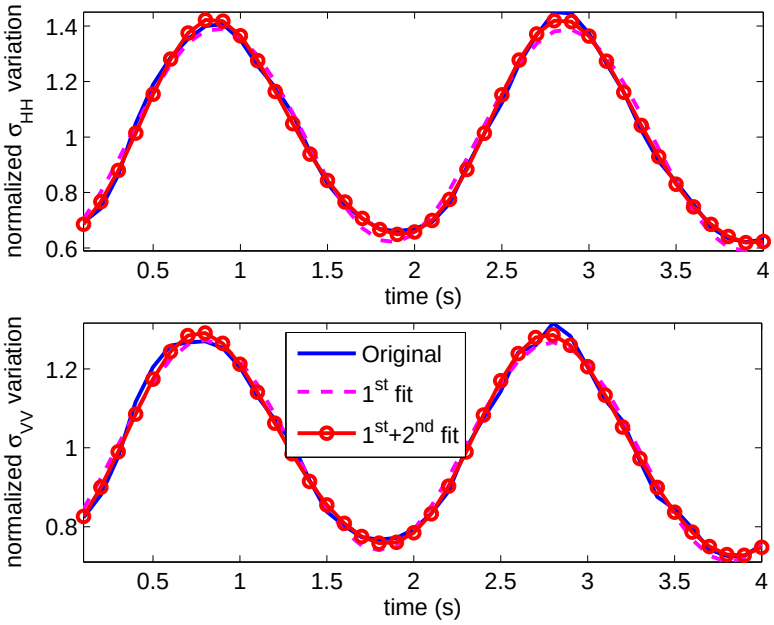

Figure 5.7: The first-order and up to second-order fitting at $\theta_i = 25^0$ from the long wave and short wave surfaces

and RTMTF [38] (or referring to equation (5.22) and (5.23)), the numerical RTMTF amplitude R_p^T and phase Φ_p^T satisfy:

$$R_p^M \sin(\Phi + \Phi_p^M) = R_p^H \sin(\Phi + \Phi_p^H) + R_p^T \sin(\Phi + \Phi_p^T). \tag{5.8}$$

From equation (5.8), it is easy to compute the amplitude R_p^T and phase Φ_p^T of the TMTF. All amplitudes of RMTF, RTMTF, and RHMTF are normalized by the steepness (0.05) of the underlying long wave.

5.3 Analytical MTF

In reality, the sea surface consists of many different water waves. Due to nonlinear interactions between long waves and short waves, those short waves are locally modulated by the presence of long waves both in amplitude and frequency. Those

short waves are kinds of Bragg waves in radar remote sensing. Therefore, observed radar signals also include some modulation, i.e., variation over space and time. Such radar signal modulation has been reported in many references [72, 38, 33, 35, 36, 76]. To analytically interpret and evaluate our numerical results of MTF, we re-derive the analytical MTF using the two-scale electromagnetic model [38, 24]. The mechanisms of TMTF and HMTF are illustrated in Figure 5.8. The TMTF is due to the local incidence angle change, i.e., $\theta_{il} = \theta_i - \theta_s$. The HMTF is due to the local short wave spectrum change. For example, the Bragg spectrum within subspace $w_i(x)$ is different with that of $w_{i+1}(x)$.

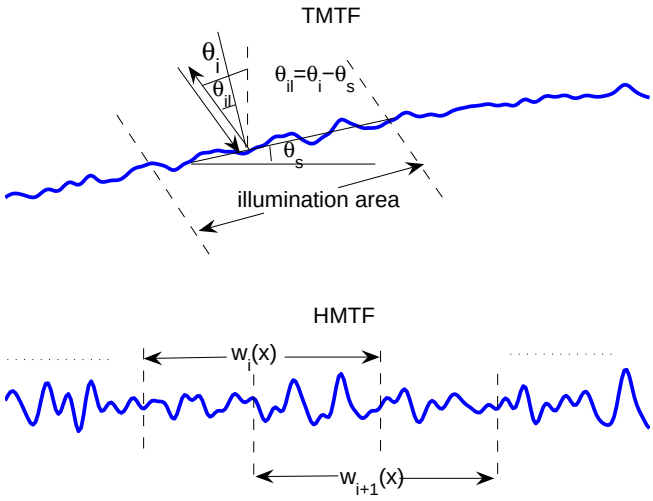

Figure 5.8: The TMTF and HMTF mechanism illustration

5.3.1 Derivation of MTF - two-scale model (tilted SPM)

Based on the Bragg scattering mechanism, the polarized backscattering normalized radar cross section (NRCS) of ocean-like surfaces (PEC) is given by [49]

$$\sigma_{HH}(\theta_i) = 4k_i^3 \cos^3(\theta_i) W(-2k_i \sin(\theta_i)), \tag{5.9}$$

$$\sigma_{VV}(\theta_i) = 4k_i^3 \frac{(1+\sin^2(\theta_i))^2}{\cos(\theta_i)} W(-2k_i \sin(\theta_i)), \tag{5.10}$$

where W is the rough surface spectral density, and $2k_i \sin(\theta_i)$ is the Bragg wavenumber. Due to the presence of long waves or currents, the local incidence angle θ_{il} is modified by the presence of local slope angle θ_s as

$$\theta_{il} = \theta_i - \theta_s. \tag{5.11}$$

Corresponding to this change, the local NRCS is given by

$$\sigma_{HH}(\theta_{il}) = 4k_i^3 \cos^3(\theta_{il}) W(-2k_i \sin(\theta_{il})), \tag{5.12}$$

$$\sigma_{VV}(\theta_{il}) = 4k_i^3 \frac{(1+\sin^2(\theta_{il}))^2}{\cos(\theta_{il})} W(-2k_i \sin(\theta_{il})). \tag{5.13}$$

Therefore, the induced NRCS variations due to the presence of long waves are

$$\Delta\sigma_{HH}(\theta_i) = \sigma_{HH}(\theta_{il}) - \sigma_{HH}(\theta_i), \tag{5.14}$$

$$\Delta\sigma_{VV}(\theta_i) = \sigma_{VV}(\theta_{il}) - \sigma_{VV}(\theta_i). \tag{5.15}$$

Due to $\theta_s << 1$, the terms of equation (5.12) can be expanded up to $O(\theta_s^2)$ as follows:

$$\cos^3(\theta_i - \theta_s) \approx \cos^3(\theta_i) + 3\theta_s \sin(\theta_i)\cos^2(\theta_i), \tag{5.16}$$

$$\begin{aligned} W(-2k_i \sin(\theta_i - \theta_s)) &\approx \overline{W}(-2k_i \sin(\theta_i - \theta_s))(1 + R_{HMTF}) \\ &\approx \overline{W}(-2k_i \sin(\theta_i))(1 + 3\theta_s \cot(\theta_i))(1 + R_{HMTF}), \end{aligned} \tag{5.17}$$

where $\overline{W}$ denotes the unperturbed spectral density, the PM spectrum density W is assumed, and R_{HMTF} denotes the HMTF. Using $\theta_s = \eta_x(x,t)$, we get

$$\frac{\Delta\sigma_{HH}(\theta_i)}{\sigma_{HH}(\theta_i)} \approx R_{HMTF} + 3\eta_x(x,t)[\tan(\theta_i) + \cot(\theta_i)], \tag{5.18}$$

where R_{HMTF} is the same order of θ_s or $\eta_x(x,t)$ [25, 77]. The first part of equation (5.18) denotes the HMTF effect, and the second term denotes the TMTF effect. The latter includes two parts, $\tan(\theta_i)$ and $\cot(\theta_i)$. $\tan(\theta_i)$ is the direct tilt effect, and $\cot(\theta_i)$ accounts for the local Bragg wave number change induced by the tilt effect.

Similarly, we have the following approximations for VV polarization:

$$[1 + \sin^2(\theta_i - \theta_s)]^2 \approx [1 + \sin^2(\theta_i)]^2 - 4\theta_s \sin(\theta_i)\cos(\theta_i)[1 + \sin^2(\theta_i)], \tag{5.19}$$

$$\frac{1}{\cos(\theta_i - \theta_s)} \approx \frac{1}{\cos(\theta_i)}(1 - \theta_s \tan(\theta_i)). \tag{5.20}$$

Combining equation (5.17), (5.19), and (5.20), we have

$$\frac{\Delta\sigma_{VV}(\theta_i)}{\sigma_{VV}(\theta_i)} \approx R_{HMTF} + \eta_x(x,t)\left[-\tan(\theta_i) + 3\cot(\theta_i) - \frac{2\sin(2\theta_i)}{1 + \sin^2(\theta_i)}\right]. \tag{5.21}$$

If there is only one long wave $\eta(x,t) = a\sin(kx - \sqrt{g_0 k}t)$ presence, both equations (5.18) and (5.21) can be simplified as

$$\frac{\Delta\sigma_{HH}(\theta_i)}{\sigma_{HH}(\theta_i)} \approx R_H \sin(\Phi) + 3ka\cos(\Phi)[\tan(\theta_i) + \cot(\theta_i)], \tag{5.22}$$

$$\frac{\Delta\sigma_{VV}(\theta_i)}{\sigma_{VV}(\theta_i)} \approx R_H \sin(\Phi) + ka\cos(\Phi)\left[-\tan(\theta_i) + 3\cot(\theta_i) - \frac{2\sin(2\theta_i)}{1 + \sin^2(\theta_i)}\right], \tag{5.23}$$

where $\Phi = kx - \sqrt{g_0 k}t$, and R_H is the amplitude of the HMTF. The TMTF and the HMTF in both equation (5.22) and (5.23) have a 90^0 phase shift, which is identical to the result given in [38]. In addition, the results given by (5.18) and (5.21) are the same as the results given by equation (12) presented in [24] except for the additional beam limited function $\tan(\theta_i)$.

5.3.2 Analytical HMTF - wave action theory

The theory of wave action was developed for the analysis of the evolution of a weakly nonlinear short wave "packet" as it propagates in an inhomogeneous background medium. The theory has been utilized to describe many phenomena of oceanographic interest, including the modulation of short waves by long waves relevant in this paper. Here, we write the first order HMTF amplitude solution R_H (normalized by the steepness of the long wave) of the wave action equation for an ocean with a "PM" spectrum [26, 77] (or see equation (4.32))

$$R_H = \frac{3+\gamma_s}{1-\frac{c_g}{c_1}}\sin(\Phi), \tag{5.24}$$

where c_g is the group velocity of the wave package with the center at the Bragg wavenumber, c_1 is the phase velocity of the long wave, and γ_s is the ratio between the group velocity and the phase velocity of the Bragg wave. The value γ_s is about 0.5 for gravity waves.

5.4 Results and discussions

This section describes the numerical results of RMTF in Section 5.4.1 based on the methodology described in Section 5.2. In this subsection, the numerical results of RMTF are also compared with the analytical results of RMTF based on the two-scale model described in Section 5.3. The numerical results of RMTF and RHMTF demonstrate a positive contribution from the third scale, the intermediate waves. To further investigate the third scale effect on RMTF, we compute the ms of intermediate waves from the simulated surface first. Then, to further interpret the numerical three-scale effect, we develop an analytical solution to calculate the three-scale effect on

RMTF based on the statistical two-scale model. Finally, results of the numerical third scale effect and those of the analytical three-scale effect are compared and discussed. The analysis of the three-scale effect on RMTF is presented in Section 5.4.2 in detail.

5.4.1 Numerical RMTF

Results of the numerical RMTF based on the methodology described in Section 5.2 and those of analytical MTF derived in Section 5.3.1 are demonstrated and compared in this subsection. We compute the numerical RTMTF by use of equation (5.8) and the analytical TMTF by using equation (5.22) and (5.23). The low cutoff k_c is used in the numerical RHMTF computation. Comparison results show that our numerical RTMTF matches very well with the analytical TMTF both in amplitude and phase.

The amplitude computation results are shown in Figure 5.9. This figure shows that both numerical RTMTF amplitude and analytical TMTF amplitude agree with each other very well within the moderate incidence angles. In addition, we also examine the RTMTF extracted from the RHMTF, which is obtained from the low cutoff 40 rad/m short waves only surface. Figure 5.10 shows that the RTMTF amplitude difference between the two cutoffs, 40 rad/m and k_c, is very small with respect to their values. Therefore, either 40 rad/m or k_c can be used as the low cutoff to calculate the RTMTF.

We also examine the phase difference between numerical RTMTF and numerical RHMTF. Theoretically, the phase difference between RTMTF and RHMTF is about -90^0 from equation (5.22) and (5.23). Figure 5.11 shows the numerical phase difference for both polarizations. In particular, there is a phase sign change for VV polarization around $\theta_i > 51^0$ (see Figure 5.9). This change is numerically captured

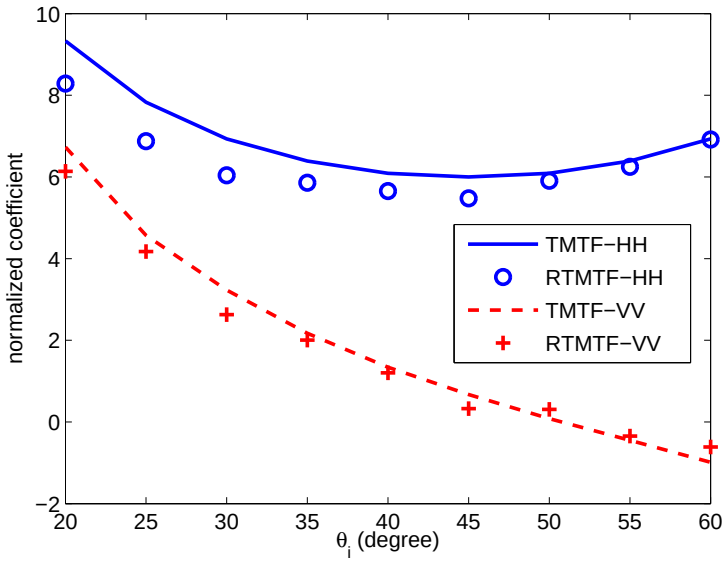

Figure 5.9: TMTF results from the numerical simulation and the analytical two scale model

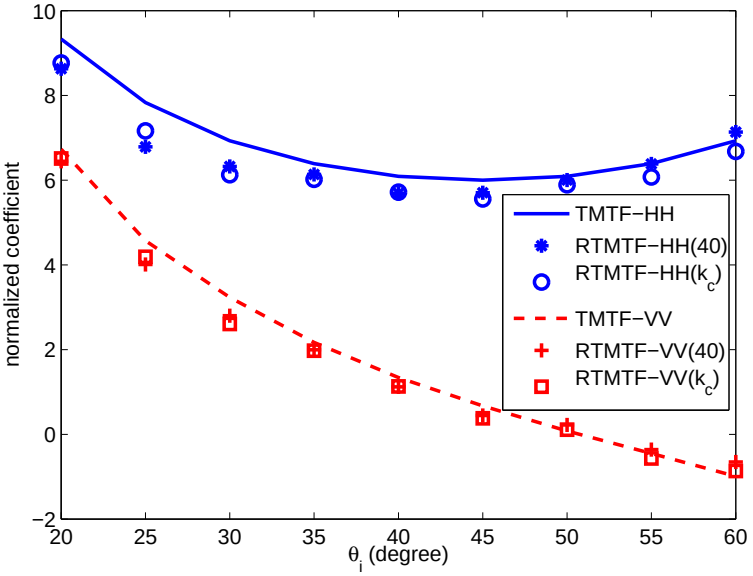

Figure 5.10: TMTF results from the numerical simulation (with cutoffs 40 rad/m and k_c) and the analytical two-scale model prediction

in Figure 5.11. Our numerical phase difference results for $\theta_i > 51^0$ are lower than the theoretical value 90^0. We also notice that the phase difference at $\theta_i = 50^0$ is much lower than its theoretical prediction value of -90^0. This discrepancy may be caused by a numerical error because the actual TMTF value around $\theta_i = 50^0$ of VV polarization is close to zero (see Figure 5.9). With a small amplitude, any small numerical error in amplitude may cause a large numerical error in phase.

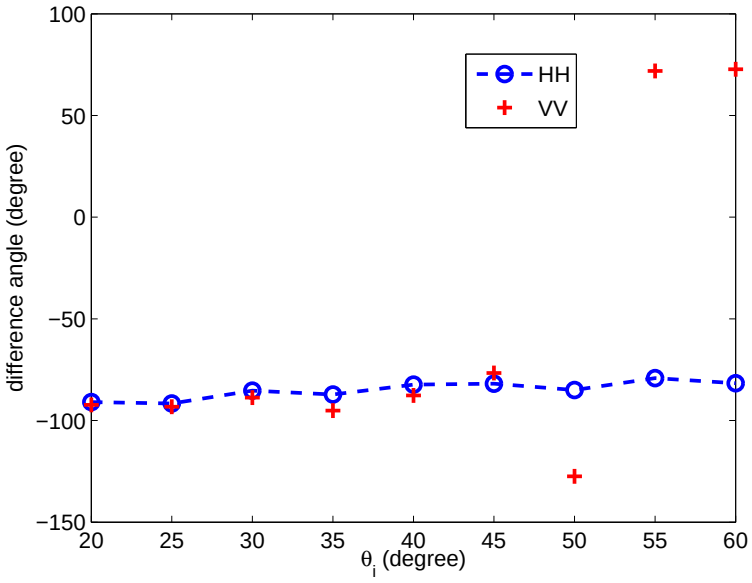

Figure 5.11: The numerical phase difference between the RTMTF and RHMTF

5.4.2 Intermediate waves (third scale) effect on RMTF

This subsection describes the numerical and analytical results of the intermediate waves effect on RMTF. These results support that the intermediate waves have positive contribution to RMTF.

Those modulated intermediate waves have both "tilt" and "hydrodynamic" modulation to Bragg waves. Hydrodynamic modulation of intermediate waves to a specific Bragg wave is too complicated, and is not studied here. In this study, we assume that the HMTF induced by the intermediate waves all are same, although the low cutoff of the intermediate waves is changed. Therefore, only the tilt modulation of intermediate waves is further studied.

With given $\theta_i = 50^0$, the intermediate waves effect on RMTF is examined by varying the intermediate wave contents by choosing different low cutoff k_c. The computed normalized RMTF and RHMTF of HH polarization are shown in Figure 5.12. Results demonstrate that the intermediate waves make more positive contribution to both RMTF and RHMTF with smaller k_c. The numerical HMTF prediction given by the numerical HMTF presented in Chapter 4 is also shown in Figure 5.12. Our numerical results also show that the RHMTF depends on intermediate wave contents, while the HMTF value is independent of the intermediate wave contents.

The intermediate waves effect on the RMTF was reported in [24, 40, 36, 41]. In order to further quantitatively analyze this effect, a method based on the intermediate waves' mean-square (ms) slope is presented both numerically and analytically in the following two subsections. Following these two subsections, the third-scale effect is interpreted by an analytical two-scale model and an empirical formula. Finally, these results are compared and discussed in the last subsection.

Numerical third-scale effect

The ms slope of the intermediate waves is computed from the simulated surface, and its variation part is induced by the long wave modulation. The different low

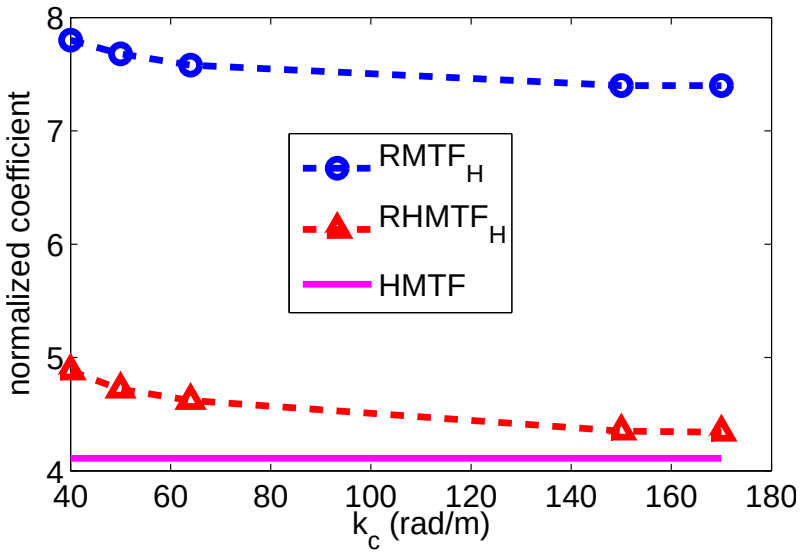

Figure 5.12: The intermediate waves effect on MTF - third-scale effect at $\theta_i = 50^0$

cutoffs of short waves have an appreciable effect on both RMTF and RHMTF (Figure 5.12). To further study the intermediate wave influence on the modulated radar signals, we analyze the ms slope of the intermediate waves. The numerical ms slope s_{ms} of the studied surfaces is computed by

$$s_{ms} = \langle s^2(x_i, t_j)\rangle = \frac{1}{N_r}\sum_{r_m=1}^{N_r}[s(x_i, t_j, r_m) - \langle s(x_i, t_j, r_m)\rangle]^2, \tag{5.25}$$

where the $s(x_i, t_j, r_m)$ is the slope at the spatial coordinate x_i, and the $\langle s(x_i, t_j, r_m)\rangle$ is the ensemble average over realizations r_m. Then, the local ms slope is weighted by the tapering incidence function g, and is further averaged over spatial x_i to obtain the local ms slope $\langle s^2(t_j)\rangle$. Essentially, the ms slope is the local illumination spot slope.

Figure 5.13 shows three different ms slopes of short waves calculated by use of equation (5.25). In this figure, $k_B = 210$ rad/m at $\theta_i = 55^0$. For example, $40 - k_B$

represents the valid short waves in $[40, 210]$ rad/m. The numerical fitting formulae for the ms slope are listed in Figure 5.13. The constant term in those fitting formulae is related to the average of the ms slope and reflects the total slope. The time varying term (having Φ) corresponds to the long wave, and the ms slope has a 90^0 phase shift with the underlying long wave slope (or in phase with long wave height) (Figure 5.13). The variation amplitude of ms slope of intermediate waves depends on the contents of short waves, and its variation period equals that of the long wave. It was reported that the intermediate waves are hydrodynamically modulated by the presence of long waves and those intermediate waves modulate short Bragg waves [41]. Figure 5.13 further supports this statement.

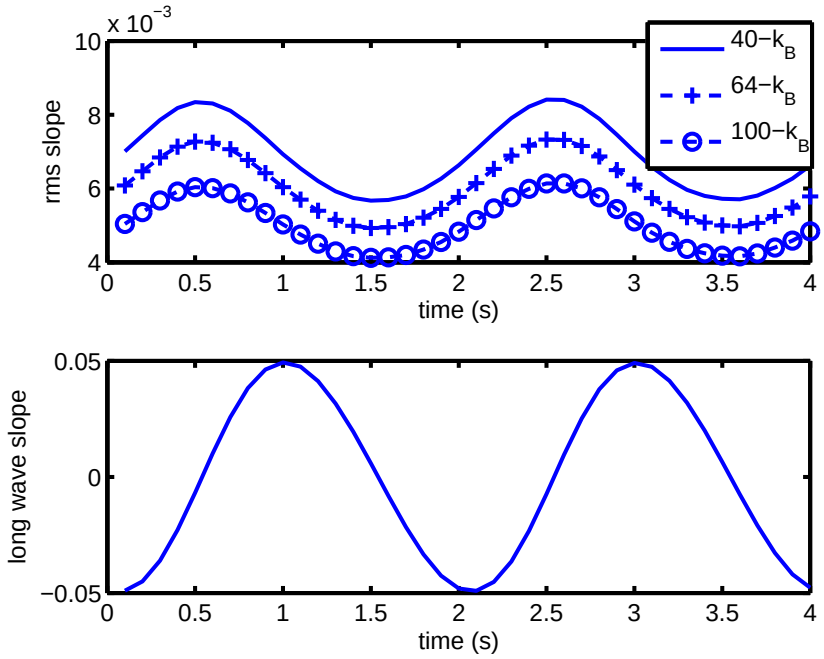

Figure 5.13: The ms slope of intermediate waves [The ms slope variations are represented by 6.9E-3+1.3E-3sin($\Phi - 0.11$) for $40 - k_B$, 5.0E-3+9.7E-4sin($\Phi - 0.11$) for $64 - k_B$, and 3.2E-3+6.2E-4sin($\Phi - 0.12$) for $100 - k_B$.]

The constant in our ms slope expression depends on the wave contents. This value can be analytically computed from $\int kW(k)dk$, where $W(k)$ is the spectral density. Given $U_{19.5} = 3$ m/s, the theoretical ms slope of wave contents in $[40, 210]$ rad/m, $[64, 210]$ rad/m, and $[100, 210]$ rad/m is 0.0067, 0.0048, and 0.0030, respectively. With the modulation of underlying long waves, our numerical results from the aforementioned constant terms are slightly greater than those theoretical values. For example, our numerical results from the ms slope of wave contents in $[40, 210]$ rad/m, $[64, 210]$ rad/m, and $[100, 210]$ rad/m are 0.0069, 0.0050, 0.0032, respectively. The reason that the numerical results are greater than their theoretical predictions is that the input energy of intermediate waves from long waves is greater than the output energy to shorter waves with respect to the intermediate waves.

ms slope effect based on statistical two-scale model

For a given multiple-scale statistical rough surface, the backscattering RCS can be expressed by a slope s integral as [80]

$$\sigma_{pp}(s, \theta_i) = \int_{-s-\Delta s}^{s+\Delta s} ds' G_{pp}^{SPM}(\theta_i) H(s'), \tag{5.26}$$

where G_{pp}^{SPM} is the polarized SPM kernel as given in (5.9) and (5.10), Δs is the integration range (which is chosen as about $2s$ in this study), and $H(s')$ is a transfer function including shadowing, projection and slope distribution effect.

Based on equation (5.26), we develop a method to study the ms effect on the RMTF. We assume that the simulated surface consists of a deterministic long wave and many stochastic PM short waves. The long wave is exactly the same as that given in previous simulations. Then, the "two-scale" MTF is computed in the following steps:

1. calculate the local incidence angle θ_{il} based on the long wave tilt;

2. calculate the local slope as

$$s(k_c) = \bar{s}(k_c) + c_0(k_c)h_L, \tag{5.27}$$

   where $\bar{s}(k_c)$ is given by $\int_{k_c}^{k_B} kW(k)dk$, $c_0(k_c)$ denotes the amplitude of ms slope of perturbed intermediate waves, and h_L denotes the long wave height;

3. search the RCS values based on the $(s(k_c), \theta_{il})$ to obtain the local RCS as $\sigma_{pp}((s(k_c), \theta_{il})$;

4. use the least-square method to extract the MTF from $\sigma_{pp}((s(k_c), \theta_{il})$ data.

The c_0 presented in equation (5.27) describes the intermediate waves' effect. As an example, its value represents the coefficient of the $\sin(\Phi)$ shown in the caption of Figure 5.13. As mentioned earlier, the stochastic intermediate waves are hydrodynamic modulated by the underlying long wave. Therefore, their ms slope is no longer zero. Due to the capability of inclusion of intermediate waves ms slope, the stochastic two-scale model is adapted to analyze the third- scale effect.

Third-scale effect by an empirical method

Alternatively, the ms slope effect can be approximated by an empirical formula as given in [40]:

$$\sigma_{pp}(x, t; \theta) \approx \overline{\sigma}_{pp}(x, t; \theta)\big[1 + c_1 < s > + c_2 < s^2 >\big] \tag{5.28}$$

where the subscript pp denotes that the polarization, c_1 and c_2 are constants, and $<>$ denotes the ensemble average. c_1 and c_2 are dependent on the surface properties. For example, if the surface is entirely stochastic, then $c_1 = 0$. However, if the surface

consists of a deterministic long wave and a band-limited stochastic short waves, c_1 relates to the long wave slope. The ms slope term c_2 denotes the intermediate waves' contribution to MTF, i.e., the third scale contribution (see Figure 5.14).

Comparison of third-scale effect results

The results of intermediate waves effects on RMTF and RHMTF are compared in detail in this section. Firstly, we show our numerical results and the results of the slope expanded equation (5.28). Then, our numerical results and the results of the stochastic two-scale model are compared and analyzed.

In order to use the empirical equation (5.28) to interpret our numerical results, we obtain c_1 and c_2 from our numerical data with use of the least-square method. Figure 5.14 shows our numerical RMTF and RHMTF results and corresponding empirical results. For simplicity, a normalized fitting formula $c_1\langle s\rangle[1 + c_2/c_1\langle s^2\rangle]$ is used to examine the empirical equation (5.28) performance. Figure 5.14 shows the linear contribution of the intermediate waves' ms slope to RTMTF and RHMTF. The ratio of c_2/c_1 of RTMTF and RHMTF in this figure is about 4 and 10, respectively. This further proves the ms slope of intermediate waves contributes the same modulation as that of the long wave slope does. However, their contribution is relatively smaller than that of the long wave. This is because $c_2 s^2 \ll c_1\langle s\rangle$. In this study, $\langle s\rangle = 0.05$, and $\langle s^2\rangle$ varies depending on the wave contents. For example, $\langle s^2\rangle$ is about 0.0013 for $k_s \in [40, 210]$ rad/m. The latter is about 2 percent of the long wave slope. This means that the intermediate waves do have some contribution to the modulation. However, their contribution is much smaller that that caused by the long wave.

Generally, the long wave profile contributes to the RHMTF, and its slope contributes to the RTMTF. The ms slope of intermediate waves varies in the phase of

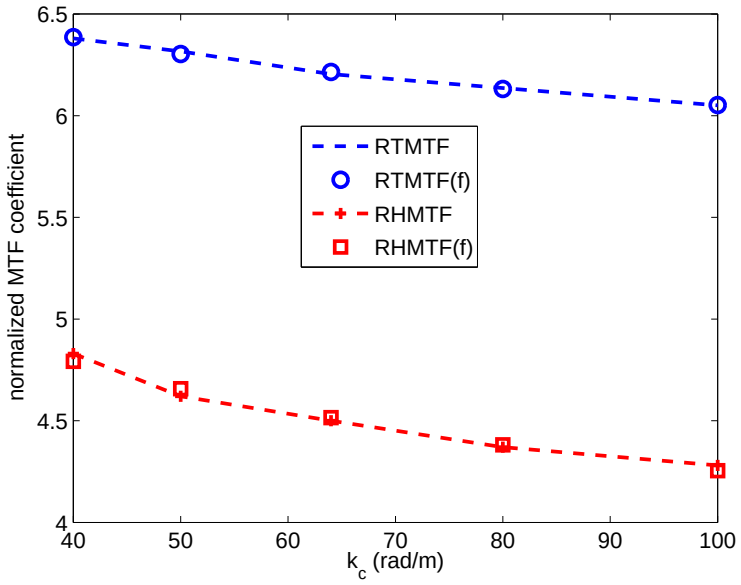

Figure 5.14: Fitting results with linear ms slope correction to the RMTF [The normalized correction formulae $c_1\langle s\rangle[1+c_2/c_1\langle s^2\rangle]$: $1+4.0\langle s^2\rangle$ for RTMTF and $1+9.8\langle s^2\rangle$ for RHMTF, and the notation f inside the bracket denotes the results obtained by the fitting method.]

the long wave profile (see Figure 5.13). This means that the ms slope may contribute to RHMTF only. However, it also contributes to RTMTF (see Figure 5.14). Therefore, the modulation contribution of those intermediate waves can account for not only RHMTF, but also RTMTF.

In order to analytically study this third-scale effect further, the RTMTF results predicted by the statistical two-scale model is used to validate our numerical RTMTF. Figure 5.15 shows the normalized RTMTF results from different methods. In the "numerical-linear" results, there is no ms slope contribution to the RTMTF. The results and the "2-scale" results increase as the cutoff increases (that is, the surface consists of fewer short waves). The reason is that the RCS with fewer short waves is smaller than that with more short waves (see Figure 5.16). Figure 5.16 shows the RCS of HH polarization with different methods and different cutoffs. However, the RTMTF given by the "numerical-linear" results and the "2-scale" results have different trends from our numerical RTMTF (see Figure 5.15). The reason is that the third-scale effect is not accounted for appropriately in the "2-scale" and is completely lacking in the "numerical-linear". In order to further explore the ms slope effect on the RTMTF, we magnify c_0 to be $4c_0$ and use it in the stochastic two-scale model. The results of the "2-scale" with $4c_0$ show the same trend as our numerical RTMTF (see Figure 5.15). The magnifying coefficient 4 numerically equals to the empirical coefficient 4.0 presented in the RTMTF (see Figure 5.14). Therefore, both the empirical approach and the analytical approach - the stochastic two-scale model interpret our numerical RMTF data very well.

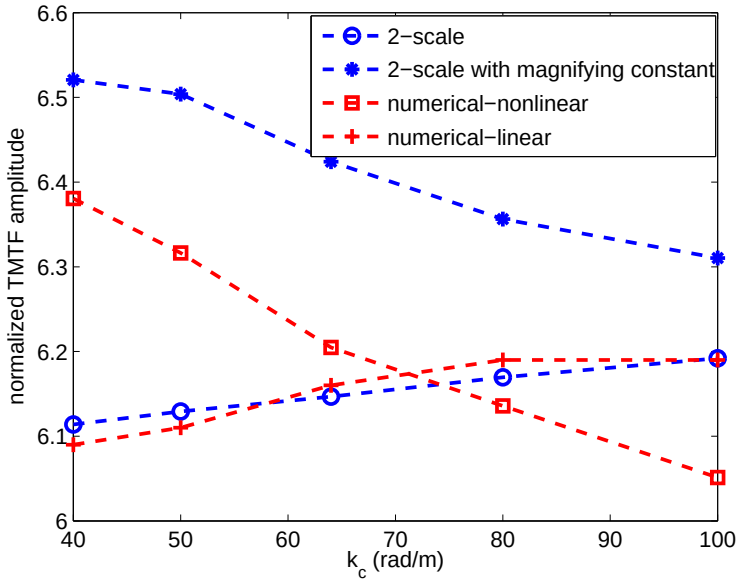

Figure 5.15: Different RTMTF comparison vs cutoff. ["numerical-linear " denotes the RTMTF obtained from a linear long wave and a band-limited "PM" short waves, "numerical-nonlinear" denotes the RTMTF obtained from nonlinear surface, "2-scale" denotes the statistical two-scale method (equation (5.27)), and "2-scale with magnifying constant" denotes $c_0 = 4c_0$ in (5.27)]

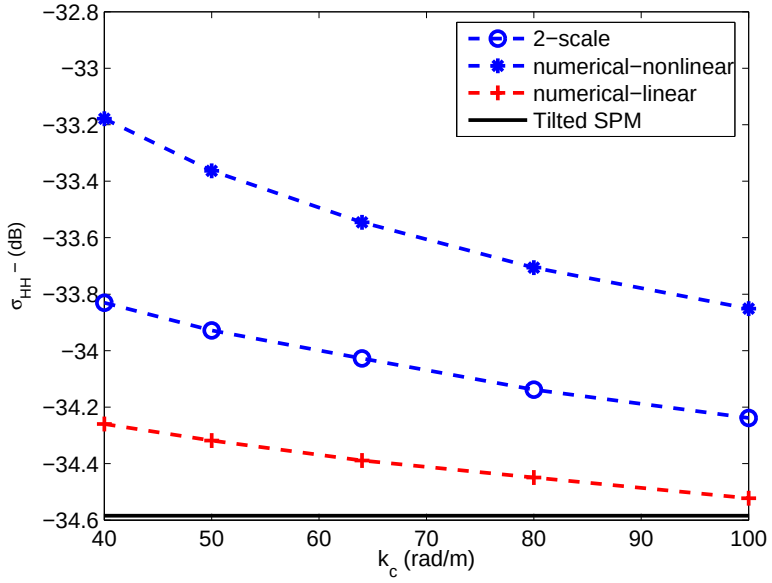

Figure 5.16: RCS of HH polarization comparison vs cutoff. ["numerical-linear " denotes the RTMTF obtained from a linear long wave and a band-limited "PM" short waves, "numerical-nonlinear" denotes the RTMTF obtained from nonlinear surface, "2-scale" denotes the statistical two-scale method (equation (5.27)), and "Tilted-SPM" denotes the tilted SPM

5.5 Concluding remarks

This chapter describes the numerical method that we developed to study the radar-ocean wave MTF (both RHMTF and RTMTF) through use of nonlinear hydrodynamics and the fast electromagnetic integral method. A very narrow Gaussian-like tapering incidence wave is capable of capturing the localized scattering field from a large finite surface.

Our numerical RTMTF results match very well with those predicted by the electromagnetic two-scale model both in amplitude and phase. The numerical results of RHMTF and RMTF indicate that the intermediate waves make an appreciable contribution to the RMTF and RHMTF because the intermediate waves are also hydrodynamically modulated by the presence of long waves. In order to interpret our numerical third scale results, we develop an empirical RCS formula along the surface slope expansion and a stochastic two-scale electromagnetic model. The third scale effect is numerically studied further by varying the intermediate wave contents. The third-scale effect on our numerical RTMTF can be explained well both with this empirical formula and the stochastic two-scale model.

The third-scale effect on the RHMTF is not further explained in this study, and it remains a challenging problem. A more powerful hydrodynamic code which can handle more spectral contents might be helpful in studying the third-scale effect on the RHMTF.

The modulation mechanisms are studied at moderate incidence angles only. A large surface length with respect to the electromagnetic wavelength can be useful for us to further study the modulation at LGA.

CHAPTER 6

ANALYTICAL DOPPLER SPECTRUM DERIVATION AND VALIDATION

6.1 Introduction

The ocean Doppler spectrum measured by a radar system is an important observed parameter. Polarized ocean Doppler measurement has been studied since several decades ago [81, 82]. It is well known that the Doppler shift is related to the radar range cell mean horizontal velocity (or mean drift), and the Doppler spectrum bandwidth is related to the horizontal velocity spread within the radar cell [82, 83]. Therefore, the Doppler information (shift and bandwidth) can provide the surface long wave information.

Many Doppler measurements are conducted at LGA [81, 84, 85] where the horizontal orbital velocity is greater with larger incidence angles. Numerical studies in Doppler spectrum from theoretical electromagnetic scattering models have been performed successfully, for example, based on the two-scale model [86], or based on exact integral equation methods [31, 22, 23, 32]. The nonlinear hydrodynamic models are applied in some studies [31, 22, 23, 32]. These studies show that the nonlinearity further broadens the Doppler bandwidth. In addition, the modulation mechanism has

been considered in the Doppler spectrum analysis, and the intermediate scale wave influence on the Doppler spectrum has also been accounted for [42, 19]. Our previous study (see Chapter 5) also demonstrated the intermediate wave impact on the short Bragg waves. Although the intermediate waves perturb the Doppler spectrum, their influence will not be analyzed here.

As mentioned earlier, such Doppler information is related to hydrodynamics. To further explore the hydrodynamic influence on the ocean Doppler, we perform an analytical Doppler derivation based on hydrodynamics. This analytical formulation can help us to simplify the ocean Doppler analysis without further electromagnetic simulations.

The purpose of this chapter is to derive an analytical formula of modulated short waves. It is based on the "Watson-West" (WW) equations [29] (see (4.1) and (4.2)). Firstly, a simplified ordinary differential equation system is obtained after some mathematical manipulations. Then, the analytical solution to this system is presented, which gives the analytical form of the complex amplitude of the modulated short waves. Further Doppler analysis based on this analytical solution are discussed. Finally, some comparisons between this simplified method and the original "WW" method are presented. In particular, the radar Doppler from the simplified WW surfaces is shown. Results demonstrate that the simplified method works well under small long wave steepness.

6.2 Derivation of simplified WW equations

Based on the assumption that the present long waves or currents are known and linear, we decompose the total surface elevation $\eta(x,t) = \eta_L(x,t) + \eta_S(x,t)$, as well

as the surface velocity potential $\phi(x,t) = \phi_L(x,t) + \phi_S(x,t)$. Then, simplified short wave evolution equations result from keeping only those terms related to short waves as follows:

$$\frac{\partial \phi_S}{\partial t} \approx -g\eta_S - \nabla\phi_S \nabla\phi_L + W_{0L}W_{0S} \tag{6.1}$$

$$\frac{\partial \eta_S}{\partial t} \approx -(\nabla\eta_L \nabla\phi_S + \nabla\eta_S \nabla\phi_L) + W_{0S} + W_{1S}, \tag{6.2}$$

where

$$W_{0L} = \kappa\phi_L \tag{6.3}$$

$$W_{0S} = \kappa\phi_S \tag{6.4}$$

$$W_{1S} = -\kappa[\eta_S\kappa\phi_L + \eta_L\kappa\phi_S] + \eta_L\kappa^2\phi_S + \eta_S\kappa^2\phi_L \tag{6.5}$$

$$g \quad \text{is the gravity acceleration.} \tag{6.6}$$

and the κ is an operator [29]. To simplify the derivation, the expansions are up to only first order in equations (6.1) and (6.2).

In order to obtain an analytical form of $\eta_S(x,t)$ or $\phi_S(x,t)$, we need to further simplify equations (6.1) and (6.2). Assuming long waves propagating along $\hat{x}$ direction, we have

$$\eta_L(x,t) = \sum_{m=-\infty}^{\infty} a_L^m e^{i(k_L^m x - \omega_L^m t + \theta^m)}, \tag{6.7}$$

$$\phi_L(x,t) = \sum_{m=-\infty}^{\infty} b_L^m e^{i(k_L^m x - \omega_L^m t + \theta^m)} \tag{6.8}$$

where

$$a_L^m = (a_L^{-m})^* \tag{6.9}$$

$$b_L^m = (b_L^{-m})^* \qquad (* \text{ denotes complex conjugate}) \tag{6.10}$$

$$k_L^m = m\frac{2\pi}{L_s} \tag{6.11}$$

$$\theta^m = -\theta^{-m} \tag{6.12}$$

$$\omega_L^m = \text{sgn}(k_L^m)\sqrt{g|k_L^m|} \qquad (\text{sgn - sign function}). \tag{6.13}$$

Such notations ensure that η_L and ϕ_L are real. For short waves, we assume that

$$\eta_S(x,t) = \sum_{n=-\infty}^{\infty} a_S^n(t)e^{ik_S^n x} \tag{6.14}$$

$$\phi_S(x,t) = \sum_{n=-\infty}^{\infty} b_S^n(t)e^{ik_S^n x}, \tag{6.15}$$

where $a_S^n = (a_S^{-n})^*$, $b_S^n = (b_S^{-n})^*$. After some manipulations (see Appendix B), the original equations (6.1) and (6.2) can be rewritten as

$$\sum_n b_S^n(t)'e^{ik_S^n x} \approx -g\sum_n a_S^n(t)e^{ik_S^n x} + \sum_{m,n}\left(|k_L^m k_S^n| + k_L^m k_S^n\right) b_L^m b_S^n(t)e^{i(k_S^n+k_L^m)x}e^{-i\omega_L^m t+i\theta^m} \tag{6.16}$$

$$\sum_n a_S^n(t)'e^{ik_S^n x} \approx \sum_n |k_S^n| b_S^n(t)e^{ik_S^n x} + \sum_{m,n}\left(|k_L^m|(|k_L^m| - |k_S^n + k_L^m|) + k_S^n k_L^m\right) a_S^n(t)b_L^m e^{i(k_S^n+k_L^m)x}e^{-i\omega_L^m t+i\theta^m}. \tag{6.17}$$

From equations (6.16) and (6.17), $a_S^n(t)$ and $b_S^n(t)$ of each k_S^n component satisfy:

$$b_S^n(t)' = -ga_S^n(t) + \sum_{\text{sgn}(n)m} 2|k_L^m k_S^{n-m}| b_L^m e^{-i\omega_L^m t+i\theta^m} b_S^{n-m}(t) \tag{6.18}$$

$$a_S^n(t)' = |k_S^n| b_S^n(t) + \sum_{-\text{sgn}(n)m} 2|k_L^m|(|k_L^m| - |k_S^{n-m}|) b_L^m e^{-i\omega_L^m t+i\theta^m} a_S^{n-m}(t), \tag{6.19}$$

where $|n| > |m|$, sgn$(n)m$ denotes m has the same sign as n. $a_S^n(t)$ and $b_S^n(t)$ have their corresponding conjugate pairs $a_S^{-n}(t)$ and $b_S^{-n}(t)$. Therefore, we can only consider all

positive n, and equations (6.18) and (6.19) are rewritten as

$$b_S^n(t)' = -ga_S^n(t) + \sum_{m>0}^{m<n} k_L^m k_S^{n-m} b_L^m e^{-i\omega_L^m t + i\theta^m} b_S^{n-m}(t) \tag{6.20}$$

$$a_S^n(t)' = k_S^n b_S^n(t) + \sum_{m>0}^{m<n} k_L^m (k_L^m - k_S^{n+m}) b_L^m e^{i\omega_L^m t - i\theta^m} a_S^{n+m}(t). \tag{6.21}$$

Note that all coefficients in equations (6.20) and (6.21) are slightly different from their previous definitions. They are double their previous values.

6.3 Determination of modulated short wave amplitudes

To further simplify equations (6.20) and (6.21), we assume there are $2N+1$ ($N < n$) truncated short waves with the central mode k_S^n and M ($M \geq 1$) long waves. Then, we rewrite equations (6.20) and (6.21) with a matrix form as following:

$$\begin{bmatrix} b_S^{n+N}(t)' \\ a_S^{n+N}(t)' \\ \cdots \\ b_S^n(t)' \\ a_S^n(t)' \\ \cdots \\ b_S^{n-N}(t)' \\ a_S^{n-N}(t) \end{bmatrix} = \mathbf{A}(t) \begin{bmatrix} b_S^{n+N}(t) \\ a_S^{n+N}(t) \\ \cdots \\ b_S^n(t) \\ a_S^n(t) \\ \cdots \\ b_S^{n-N}(t) \\ a_S^{n-N}(t) \end{bmatrix}, \tag{6.22}$$

where $\mathbf{A}(t)$ is a diagonally banded block matrix, and each of its block element $\mathbb{A}_{pq}$ (p and $q \in [1, 2N+1]$) consists of a 2x2 matrix. The diagonal block $\mathbb{A}_{pp}$ is given by

$$\begin{bmatrix} 0 & -g \\ k_S^{n+N+1-p} & 0 \end{bmatrix}.$$

The other non-zero blocks are $\mathbb{A}_{p,p+m}$ ($m \in [1, M]$) and $\mathbb{A}_{p,p-m}$ ($m \in [1, M]$), and they are given as follows:

$$\mathbb{A}_{p,p+m} = \begin{bmatrix} -\omega_L^m a_L^m k_S^{n+N+1-p-m} e^{-i\omega_L^m t + i\theta^m} & 0 \\ 0 & 0 \end{bmatrix},$$

$$\mathbb{A}_{p,p-m} = \begin{bmatrix} 0 & 0 \\ 0 & -\omega_L^m a_L^m (k_L^m - k_S^{n+N+1-p+m}) e^{i\omega_L^m t - i\theta^m} \end{bmatrix},$$

where we use the identity $k_L^m b_L^m = -\omega_L^m a_L^m$.

The above matrix equation (6.22) can be written as

$$\frac{d\mathbf{B}}{dt} = \mathbf{A}(t)\mathbf{B}. \tag{6.23}$$

Since $\mathbf{A}(t)$ is varying over t, equation (6.23) is a variable coefficient first-order ordinary differential system. Rewriting $\mathbf{A}(t) = \mathbf{A}_0 + \mathbf{A}_1(t)$, we have

$$\frac{d\mathbf{B}(t)}{dt} = \left[\mathbf{A}_0 + \mathbf{A}_1(t)\right]\mathbf{B}(t), \tag{6.24}$$

where

$$\mathbf{A}_0 = \begin{bmatrix} \mathbb{A}_{11} & 0 & ... & 0 & 0 \\ 0 & \mathbb{A}_{22} & ... & 0 & 0 \\ ... & ... & ... & ... & ... \\ 0 & 0 & ... & \mathbb{A}_{2N,2N} & 0 \\ 0 & 0 & ... & 0 & \mathbb{A}_{2N+1,2N+1} \end{bmatrix},$$

$$\mathbf{A}_1(t) = \begin{bmatrix} 0 & \mathbb{A}_{12} & ... & 0 & 0 \\ \mathbb{A}_{21} & 0 & ... & 0 & 0 \\ ... & ... & ... & ... & ... \\ 0 & 0 & ... & 0 & \mathbb{A}_{2N,2N+1} \\ 0 & 0 & ... & \mathbb{A}_{2N+1,2N} & 0 \end{bmatrix}.$$

With this decomposition, we rewrite equation (6.24) as

$$\frac{d\mathbf{B}(t)}{dt} = \mathbf{A}_0\mathbf{B}(t) + \mathbf{A}_1(t)\mathbf{B}(t), \tag{6.25}$$

Equation (6.25) consists of a constant coefficient homogeneous equation plus a "forcing" term $\mathbf{A}_1(t)\mathbf{B}(t)$. The eigenvalues of matrix $\mathbf{A}_0$ consist of those eigenvalues of each block matrix $\mathbb{A}_{pp}$, which are $\lambda_{p,\pm} = \pm\sqrt{-gk_S^{n+N+1-p}}$ ($p \in [1, 2N+1]$, and total $4N+2$ eigenvalues), and corresponding eigenvectors $\mathbf{e}$ only have non-zero entries with $\mathbf{e}_{p,p} = -\frac{g}{\sqrt{-gk_S^{n+N+1-p}}}$, $\mathbf{e}_{p,p+1} = 1$ for eigenvalue $\sqrt{-gk_S^{n+N+1-p}}$, and $\mathbf{e}_{p,p} = \frac{g}{\sqrt{-gk_S^{n+N+1-p}}}$, $\mathbf{e}_{p,p+1} = 1$ for eigenvalue $-\sqrt{-gk_S^{n+N+1-p}}$, respectively. Thus, the general solution $\mathbf{B}_0(t)$ of the homogeneous equation can be written with positive

propagation short waves as

$$\mathbf{B}_0(t) = \begin{bmatrix} a_S^{n+N}(t_0)\frac{g}{\sqrt{-gk_S^{n+N}}}e^{-\sqrt{-gk_S^{n+N}}t} \\ a_S^{n+N}(t_0)e^{-\sqrt{-gk_S^{n+N}}t} \\ \cdots \\ a_S^{n}(t_0)\frac{g}{\sqrt{-gk_S^{n}}}e^{-\sqrt{-gk_S^{n}}t} \\ a_S^{n}(t_0)e^{-\sqrt{-gk_S^{n}}t} \\ \cdots \\ a_S^{n-N}(t_0)\frac{g}{\sqrt{-gk_S^{n-N}}}e^{-\sqrt{-gk_S^{n-N}}t} \\ a_S^{n-N}(t_0)e^{-\sqrt{-gk_S^{n-N}}t} \end{bmatrix},$$

where $a_S^{n+p}(t_0)$ is the short wave mode k_S^{n+p} amplitude at initial time t_0. Then, with the "forcing" term in equation (6.25) approximated by $\mathbf{A}_1(t)\mathbf{B}_0(t)$, we rewrite equation (6.25) as

$$\frac{d\mathbf{B}(t)}{dt} \approx \mathbf{A}_0\mathbf{B}(t) + \mathbf{A}_1(t)\mathbf{B}_0(t). \tag{6.26}$$

The final solutions for $b_{n+N+1-p}(t)$ and $a_{n+N+1-p}$ are given, respectively,

$$b_{n+N+1-p}(t) = \frac{1}{2}\sum_{m=1}^{M}(\omega_L^m a_L^m)III_p^U(t) + a_{n+N+1-p}(t_0)\frac{g}{\sqrt{-gk_S^{n+N+1-p}}}e^{-i\sqrt{gk_S^{n+N+1-p}}t}, \tag{6.27}$$

$$a_{n+N+1-p}(t) = \frac{1}{2}\sum_{m=1}^{M}(\omega_L^m a_L^m)III_p^D(t) + a_{n+N+1-p}(t_0)e^{-i\sqrt{gk_S^{n+N+1-p}}t}. \tag{6.28}$$

In the above equations, we have already assumed C^U and C^D are zero (or C^U and C^D are absorbed in the initial condition), and $III_p^U(t)$ and $III_p^D(t)$ are given in Appendix B. Furthermore, second-order approximations are also presented there.

As an example, the modulated short wave amplitude of mode k_S^n ($p = N+1$) with only one long wave present ($k_L = 1$, $m = 1$, and $t_0 = 0$) is explicitly written as

$$\begin{aligned} a_S^n(t) = a_S^n(0)e^{-i\sqrt{gk_S^n}t} - \frac{i\omega_L a_L a_S^{n-1}(0)k_S^n\sqrt{gk_S^{n-1}}}{\left(\sqrt{gk_S^{n-1}}+\omega_L\right)^2 - gk_S^n}e^{-i(\sqrt{gk_S^{n-1}}+\omega_L)t+i\theta} \\ + \frac{i\omega_L a_L a_S^{n+1}(0)k_S^n\left(\sqrt{gk_S^{n+1}}-\omega_L\right)}{\left(\sqrt{gk_S^{n+1}}-\omega_L\right)^2 - gk_S^n}e^{-i(\sqrt{gk_S^{n+1}}-\omega_L)t-i\theta}, \end{aligned} \tag{6.29}$$

where $a_S^n(0)$ is the initial amplitude, and θ is the initial phase of the long wave. The amplitude of the mode k_S^n given by equation (6.29) shows that only the two adjacent modes have a contribution to the central mode. If we further simplify (6.29) with the assumption $\sqrt{gk_S^n} >> \omega_L$, (6.29) can be written as

$$\begin{aligned} a_S^n(t) \approx a_S^n(0)e^{-i\sqrt{gk_S^n}t} - \frac{ia_L a_S^{n-1}(0)k_S^n}{2}e^{-i(\sqrt{gk_S^{n-1}}+\omega_L)t+i\theta} \\ - \frac{ia_L a_S^{n+1}(0)k_S^n}{2}e^{-i(\sqrt{gk_S^{n+1}}-\omega_L)t-i\theta}. \end{aligned} \tag{6.30}$$

If we substitute the Fourier coefficient $a_S^n(t)$ into (6.14), and set the initial time t_0 and $t = t - t_0$, we get

$$\begin{aligned} \eta_S(x,t) \approx \sum_{n=-\infty}^{\infty}\Bigg[a_S^n(t_0)e^{i(k_S^n x-\omega_S^n t)} - \frac{i}{2}k_S^n\Bigg(a_S^{n-1}(t_0)e^{i(k_S^{n-1}x-\omega_S^{n-1}t)}a_L e^{i(x-\omega_L t)} \\ + a_S^{n+1}(t_0)e^{i(k_S^{n+1}x-\omega_S^{n+1}t)}a_L e^{-i(x-\omega_L t)}\Bigg)\Bigg]. \end{aligned} \tag{6.31}$$

The difficulty is to determine the initial values of $a_S^{n-1}(t_0)$ and $a_S^{n+1}(t_0)$. We offer an approach: assuming that there is only one long wave in the initial state, i.e., $a_S^n(0) = 1$, then we can approximate

$$a_S^{n-1}(0) \approx a_S^{n-1}(\Delta t) = \frac{i\omega_L a_L a_S^n(0)k_S^{n-1}\left(\sqrt{gk_S^n}-\omega_L\right)}{\left(\sqrt{gk_S^n}-\omega_L\right)^2 - gk_S^{n-1}}e^{-i(\sqrt{gk_S^n}-\omega_L)\Delta t-i\theta}, \tag{6.32}$$

$$a_S^{n+1}(0) \approx a_S^{n+1}(\Delta t) = -\frac{i\omega_L a_L a_S^n(0)k_S^{n+1}\sqrt{gk_S^n}}{\left(\sqrt{gk_S^n}+\omega_L\right)^2 - gk_S^{n+1}}e^{-i(\sqrt{gk_S^n}+\omega_L)\Delta t+i\theta}. \tag{6.33}$$

6.4 Analytical Doppler analysis

The well-known Doppler effect of short waves propagating over a long wave is given by [69]

$$\widetilde{\omega}_S^n = \omega_S^n + k_S^n U_L = \omega_S^n + \frac{1}{2} k_S^n a_L \omega_L [e^{i\omega_L t - i\theta} + e^{-i\omega_L t + i\theta}], \tag{6.34}$$

where $\widetilde{\omega}_S^n$ is the apparent (or perturbed) radian frequency of short wave with the mode k_S^n. To further analyze the Doppler shift from equation (6.30), we assume $\sqrt{g k_S^{n\pm1}} \approx \sqrt{g k_S^n} = \omega_S^n$ in equation (6.30), and get

$$a_S^n(t) \approx e^{-i\omega_S^n t} \left[a_S^n(0) - a_S^{n-1}(0) \frac{i a_L k_S^n}{2} e^{-i\omega_L t + i\theta} - a_S^{n+1}(0) \frac{i a_L k_S^n}{2} e^{i\omega_L t - i\theta} \right] \tag{6.35}$$

In the spectral domain, the short wave form is written as

$$\eta_S(x,t) = \sum_{n=1}^{N} c_S^n e^{i(k_S^n x - \widetilde{\omega}_S^n t)} \tag{6.36}$$

Comparing equation (6.14) and equation (6.36), we expect

$$a_S^n(t) = c_S^n e^{-i\widetilde{\omega}_S^n t}, \tag{6.37}$$

where c_S^n is the amplitude of wavemode k_S^n. It implies that

$$c_S^n e^{-\frac{1}{2} i k_S^n a_L \omega_L [e^{i\omega_L t - i\theta} + e^{-i\omega_L t + i\theta}] t} = a_S^n(0) - \frac{i a_L a_S^{n-1}(0) k_S^n}{2} e^{-i\omega_L t + i\theta} - \frac{i a_L a_S^{n+1}(0) k_S^n}{2} e^{i\omega_L t - i\theta}. \tag{6.38}$$

To further simplify this comparison, we assume the global time t as $t = t_0 + \tau$, where τ is the small scale time and t_0 is the large scale time. We also assume $\omega_L \tau << 1$.

Therefore, the left side of equation (6.38) can be written as

$$\begin{aligned} c_S^n e^{-\frac{1}{2}ik_S^n a_L\omega_L[e^{i\omega_L t-i\theta}+e^{-i\omega_L t+i\theta}]t} &= c_S^n e^{-\frac{1}{2}ik_S^n a_L\omega_L[e^{i\omega_L(t_0+\tau)-i\theta}+e^{-i\omega_L(t_0+\tau)+i\theta}]t_0} \\ & e^{-\frac{1}{2}ik_S^n a_L\omega_L[e^{i\omega_L(t_0+\tau)-i\theta}+e^{-i\omega_L(t_0+\tau)+i\theta}]\tau} \\ &\approx c_S^n e^{-\frac{1}{2}ik_S^n a_L\omega_L[e^{i\omega_L t_0-i\theta}+e^{-i\omega_L t_0+i\theta}]t_0} e^{-\frac{1}{2}ik_S^n a_L\omega_L[e^{i\omega_L(t_0+\tau)-i\theta}+e^{-i\omega_L(t_0+\tau)+i\theta}]\tau} \\ &\approx \widetilde{c}_S^n(t_0)\left[1-\frac{i}{2}k_S^n a_L\omega_L\tau(e^{i\omega_L t_0}e^{i\omega_L\tau-i\theta}+e^{-i\omega_L t_0}e^{-i\omega_L\tau+i\theta})\right], \end{aligned} \tag{6.39}$$

where $\widetilde{c}_S^n(t_0) = c_S^n e^{-\frac{1}{2}ik_S^n a_L\omega_L[e^{i\omega_L t_0-i\theta}+e^{-i\omega_L t_0+i\theta}]t_0}$. Substituting equation (6.39) in equation (6.38), we get

$$\widetilde{c}_S^n(t_0) = a_S^n(t_0), \tag{6.40}$$

$$\omega_L\tau\widetilde{c}_S^n(t_0)e^{-i\omega_L t_0} = a_S^{n-1}(t_0), \tag{6.41}$$

$$\omega_L\tau\widetilde{c}_S^n(t_0)e^{i\omega_L t_0} = a_S^{n+1}(t_0). \tag{6.42}$$

Equation (6.40)-(6.42) imply that

- the adjacent mode amplitudes with respect to the central mode are symmetric at any given time t_0. Figure 6.1 proves this symmetry from the results given by our derived solution ((6.20) and (6.21)) and the exact original WW code, where the initial condition is $a_L =$, $k_L = 1$ rad/m, $a_S =$, and $k_s = 100$ rad/m.
- there is a 90^0 phase shift with respect to that of the central mode. These two adjacent mode amplitudes are conjugate to each other (Figure 6.2). The data in Figure 6.2 are obtained from the exact WW code. In this Figure, the original "WW" result is denoted by "WW", and its nonlinear expansion is up to the third order. The result obtained from the simplified equations (6.1) and (6.2) is denoted by "WWS". Then, the result obtained from truncated equations (6.20) and (6.21) with use of MATLAB ODE solver "ode45" (a solver for initial value problems for ODE) is denoted by "ODE".

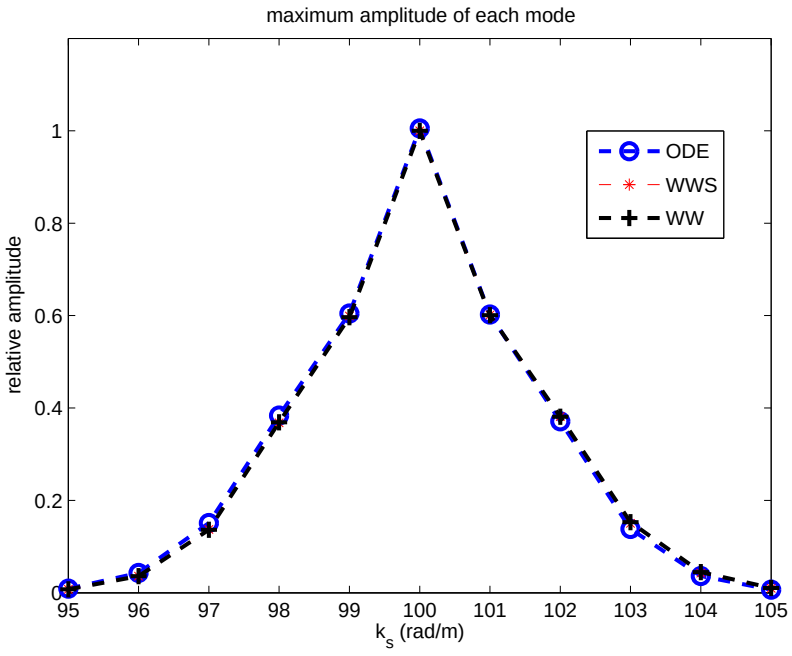

Figure 6.1: The normalized spectral amplitudes comparison among different wave modes

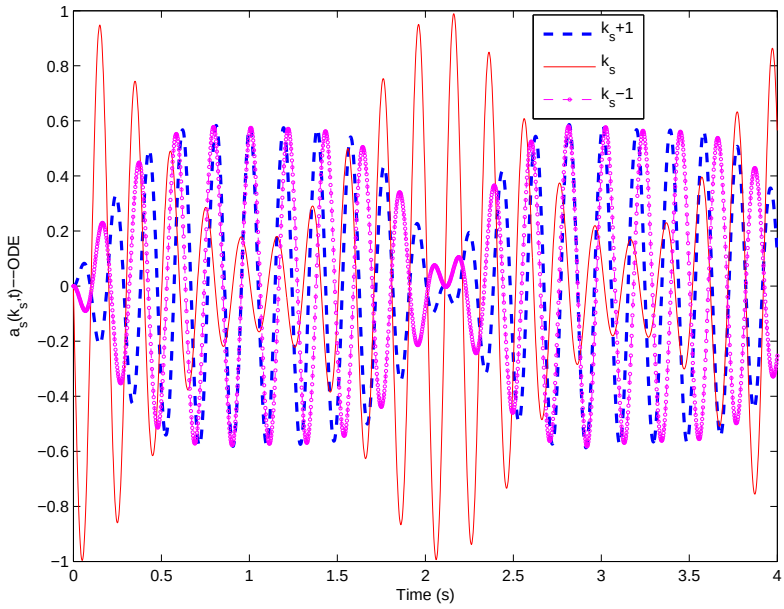

Figure 6.2: The relative amplitudes evolution comparison among three adjacent wave modes

From Figure 6.1 and Figure 6.2, it is obvious that the Doppler effect is at least implicitly included in the solution (6.30).

6.5 Simplified WW equations and analytical results validations

In the truncated case ("ODE"), if we do not have a priori about the initial condition, we need to run a matrix system at least 14X14 to obtain the reasonable $a_S^n(t)$, which means there are at least seven distinct adjacent short waves. However, if we set the initial condition correctly, we only need three distinct adjacent short waves using equation (6.29) to obtain the amplitude evolution, see Figure 6.3. In this figure, the initial amplitudes are obtained from the "ODE" result. The analytical solution

(denoted by "Ana") is obtained from equation (6.30) with initialization (6.32) and (6.33) (see Appendix B).

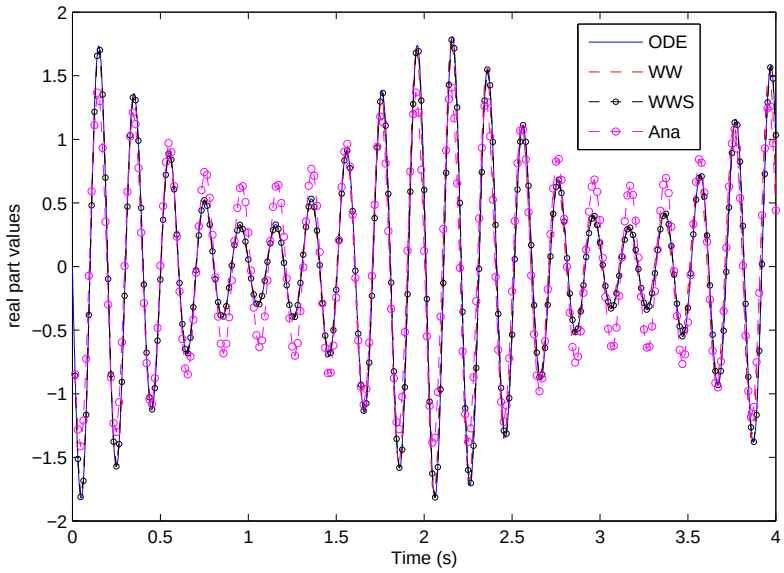

Figure 6.3: The complex amplitude $a_S^n(t)$ evolution with one long wave $k_L = 1$ rad/m and $k_L a_L = 0.01$

The difference between the "Ana" solution and others is that only three short wave components are considered in this analytical solution. If more short wave components are accounted for, the difference would be smaller. Alternatively, if the initial adjacent wave amplitudes are obtained from other methods, and the central wave mode evolution is still using equation (6.30), the amplitude evolution difference among those methods is very small (see Figure 6.4).

In order to further validate our analytical derivation ((6.20) and (6.21)), the spectral coefficient evolution and total surface height computed by ODE, WWS, and WW, in four different cases, are further compared as follows.

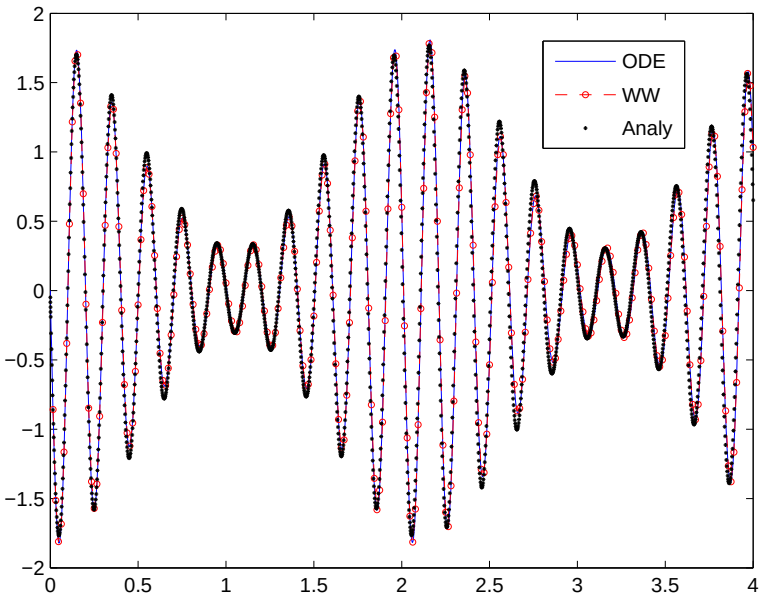

Figure 6.4: The complex amplitude $a_S^n(t)$ evolution with one long wave $k_L = 1$ rad/m and $k_L a_L = 0.01$ using initial adjacent wave amplitudes from ODE solution

6.5.1 Case 1: one long wave + one short wave

In this part, two different long wave steepness (0.01 and 0.02, respectively) cases are studied. Figure 6.5 shows the comparison among "WW", "WWS", and "ODE". The complex amplitude a_S^{100} matches perfectly among those methods. However, if the steepness increases, there is some discrepancy among those methods. In particular, the discrepancy increases when the time increases, see Figure 6.6.

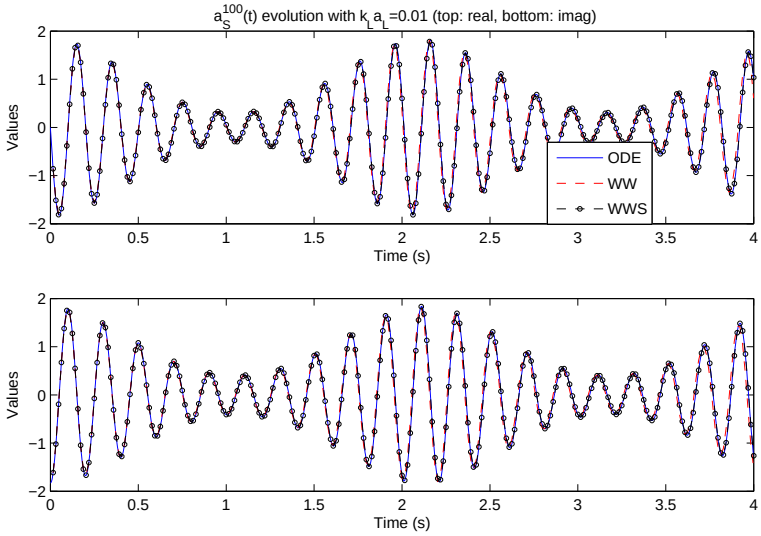

Figure 6.5: The complex amplitude $a_S^n(t)$ evolution with one long wave $k_L = 1$ rad/m and $k_L a_L = 0.01$

6.5.2 Case 2: one long wave + three short waves

Figure 6.7 shows the central short wave amplitude a_S^{100} time evolution with initial three short waves with wavenumber $[99, 100, 101]$ rad/m. The simplified method predicts rather accurate results with respect to those given by the "exact" WW.

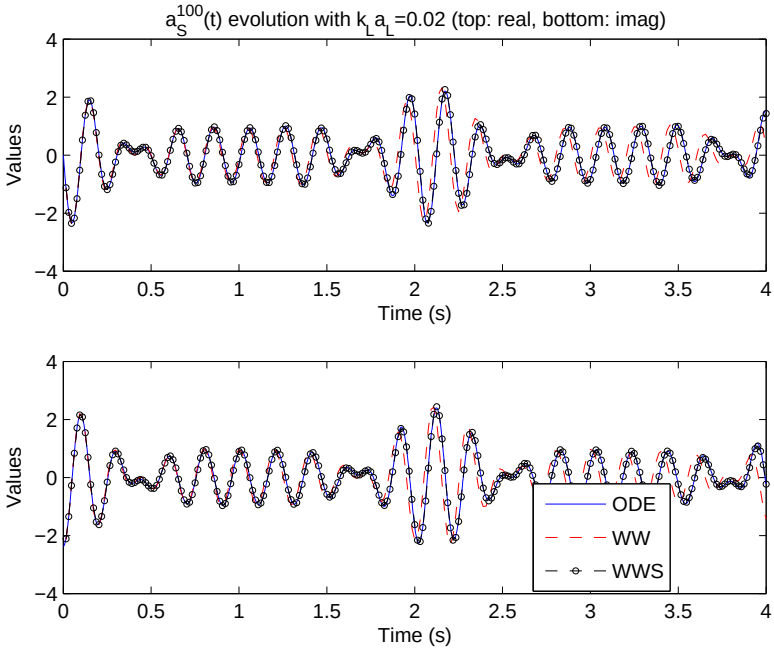

Figure 6.6: The complex amplitude $a_S^n(t)$ evolution with one long wave $k_L = 1$ rad/m and $k_L a_L = 0.02$

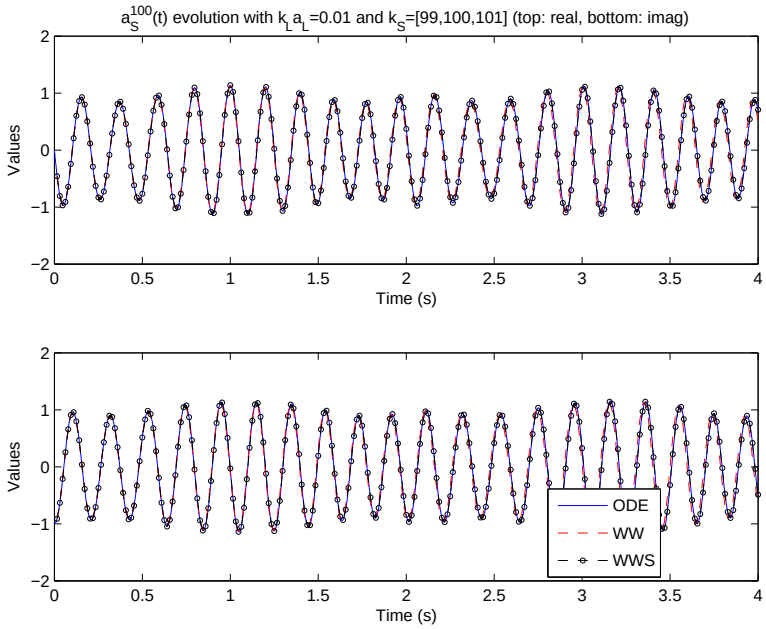

Figure 6.7: The complex amplitude $a_S^n(t)$ evolution with one long wave $k_L = 1$ rad/m, $k_L a_L = 0.01$ and three short waves

6.5.3 Case 3: two long waves + one short wave

Figure 6.8 shows the comparison with initially two long waves: $k_L^1 = 1$ rad/m and $k_L^2 = 2$ rad/m. Again, the simplified WW method works well.

6.5.4 Case 4: one long wave + band-limited PM short waves

Figure 6.9 shows the surface profile and spectral coefficient comparison between the WW and WWS with a band limited PM short wavenumber [30,60] rad/m. The long wave steepness is again 0.01. It further proves that the WWS works accurately for many random short waves.

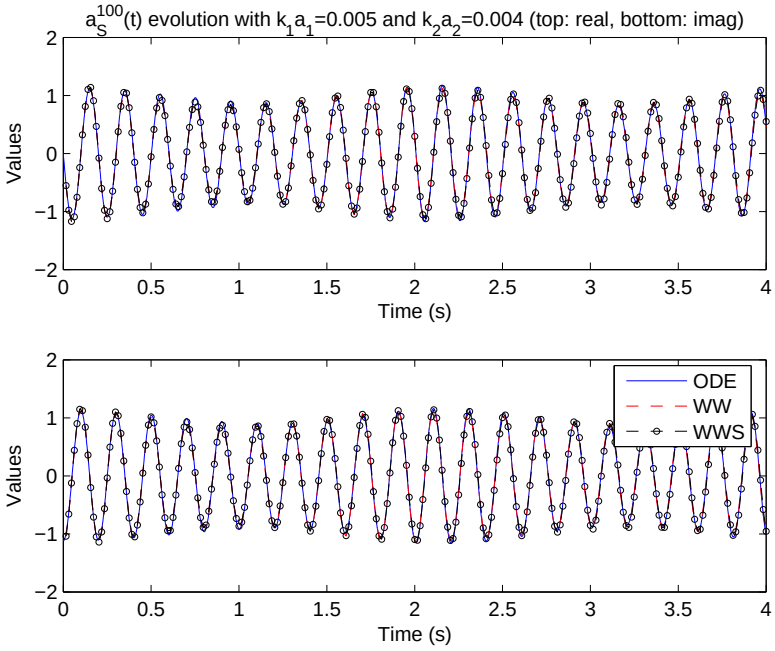

Figure 6.8: The complex amplitude $a_S^n(t)$ evolution with two long wave $k_L^1 = 1$ rad/m and $k_L^2 = 2$ rad/m

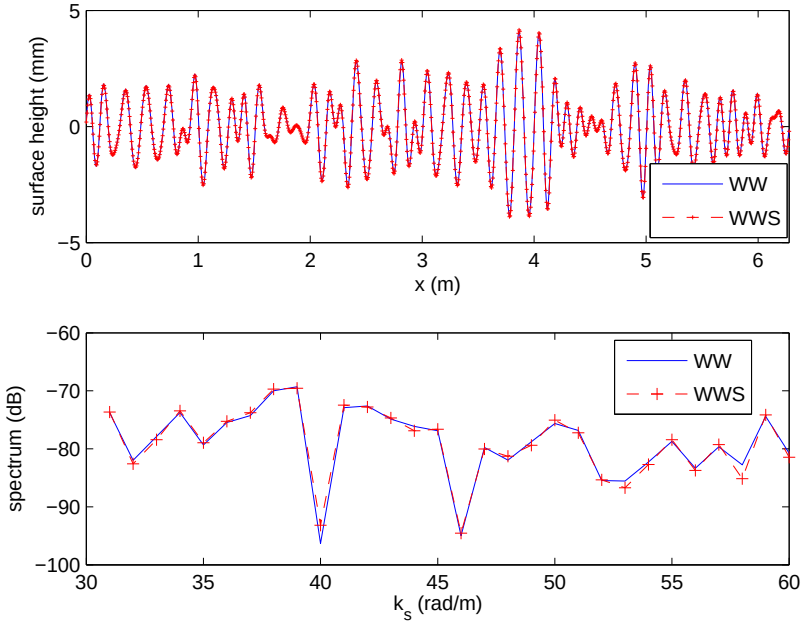

Figure 6.9: The band-limited PM short waves comparison with one long wave $k_L^1 = 1$ rad/m between WWS and WW

The advantage of using WWS and ODE is that we can solve the nonlinear equations without a need to perform intensive numerical computations for original WW equations. In particular, the ODE solution is a dramatic computation saving method.

The results presented have demonstrated that both the simplified WW method and the truncated numerical method work rather well given that the long wave steepness is small, for example, 0.01.

6.6 Numerical Doppler spectrum from simulated radar data

The modulated short wave amplitudes predicted by simplified WW method are very close to those from the original WW solution in the previous section. All those comparisons are from a hydrodynamics point of view. In order to further investigate how this simplified WW solution predicts Doppler spectrum, we conduct radar Doppler analysis, which is a combination of hydrodynamics and electromagnetics.

Polarized Doppler spectra are computed for two slightly different surfaces. The first surface includes only modulated short waves based on equations (6.1) and (6.2), and its surface profile is shown in the lower plot in Figure 6.10. The other surface contains the linear long wave (see the upper plot in Figure 6.10) in addition to modulated short waves in the first surface. The total surface length is 201.06 (64π) m, the band-limited PM short wave cutoffs are [40,240] rad/m, the long wave wavenumber k_L is 0.0625 rad/m, and its steepness is 0.01, and the wind speed at 19.5 m is 3 m/s. The nonlinear surface evolves over time with a recorded time step as 0.02 s, and total time duration is 1.28 s (with 64 time steps). The electromagnetic center frequency is 3.0 GHz, with 128 frequency sweep (sweep step: 0.7455 MHz). The radar incidence angle is 80^0.

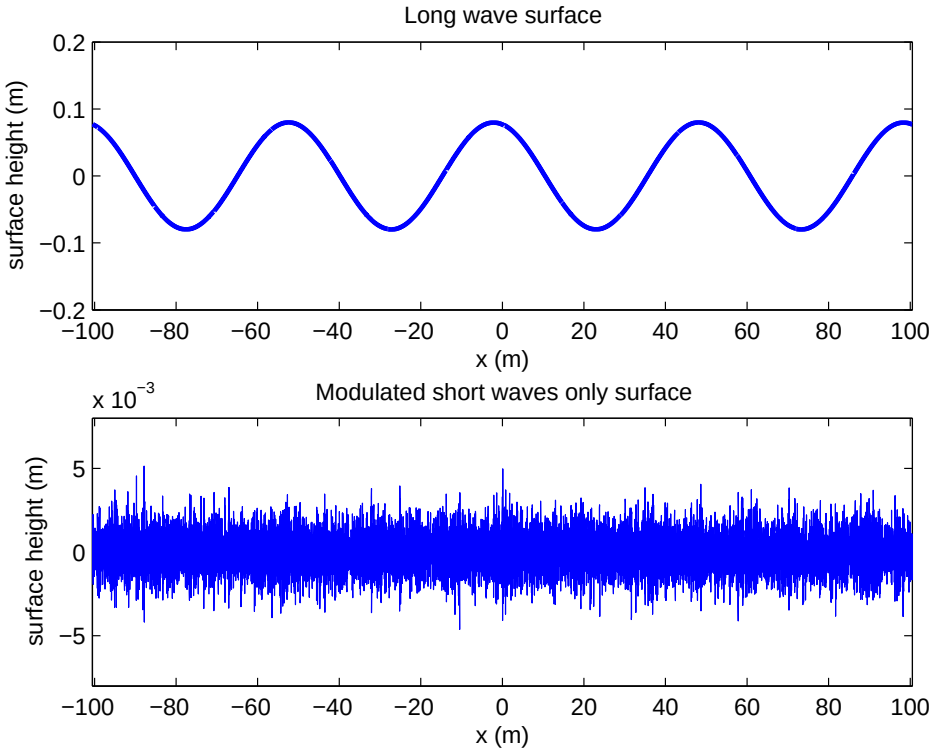

Figure 6.10: The modulated short wave and long wave only surfaces profile at time 0.02 s

In order to study the modulated Doppler spectrum, we apply the sweep radar technique to calculate the range-resolved polarized Doppler spectra. Both HH and VV polarized Doppler spectra are shown in Figure 6.11. Comparing Figure 6.11 and

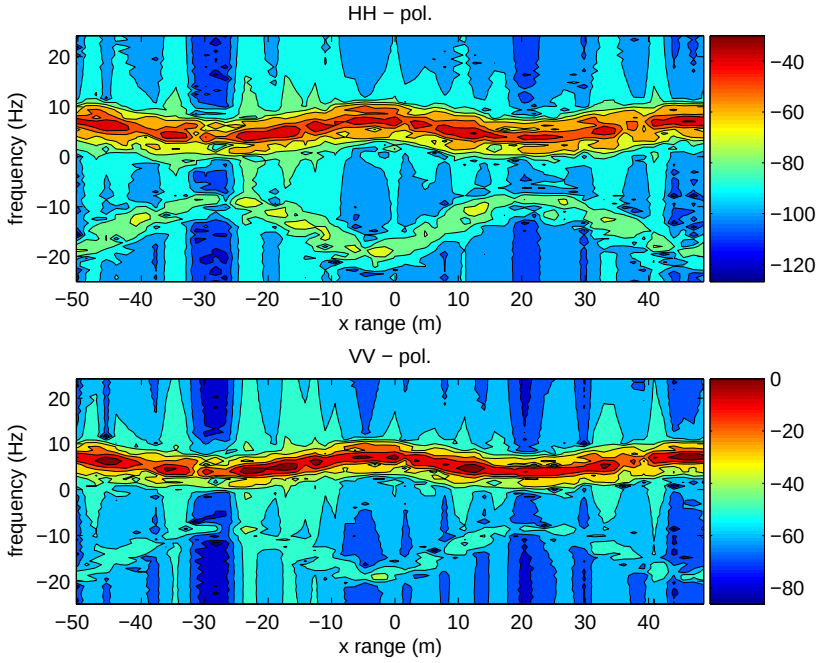

Figure 6.11: The polarized Doppler spectra without explicit long waves

the top plot in Figure 6.10, we find that the Doppler spectra vary with the same period as that of the given long wave. The Doppler frequency reaches the maximum value at the crest of the long wave, and the minimum at the trough of the long wave. We also notice that there is very weak negative Doppler spectra existence. They are more than 30 dB down to the positive Doppler intensity. We perform a Doppler analysis based on the original WW equation. The results are shown in Figure 6.12, and they can affirm that the negative Doppler results are artifacts.

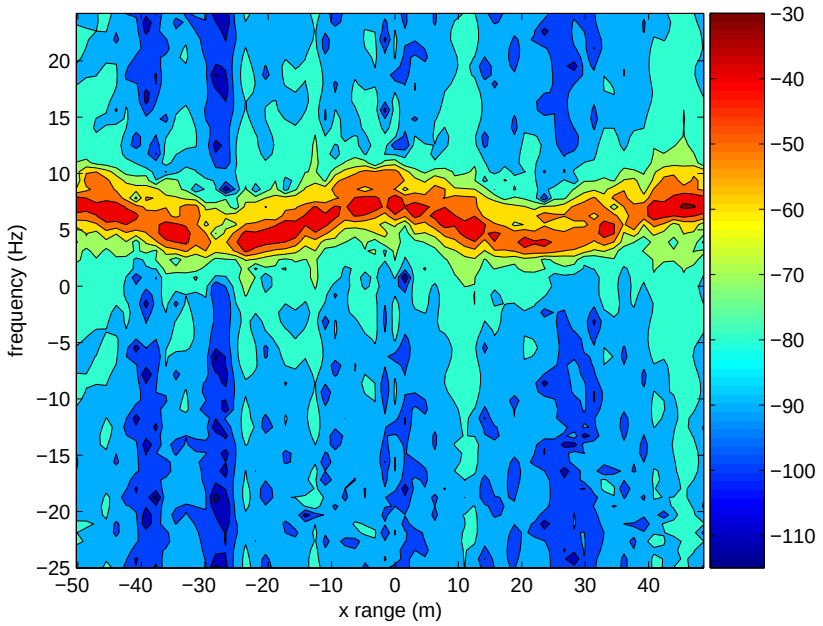

Figure 6.12: The polarized Doppler spectrum at HH polarization using the original WW equations

The Doppler spectrum width (Doppler bandwidth or Doppler shift) is also an important parameter in the Ocean Doppler analysis [87]. To further analyze the Doppler spectra width, we compare the range average Doppler spectra. Figure 6.13 shows the

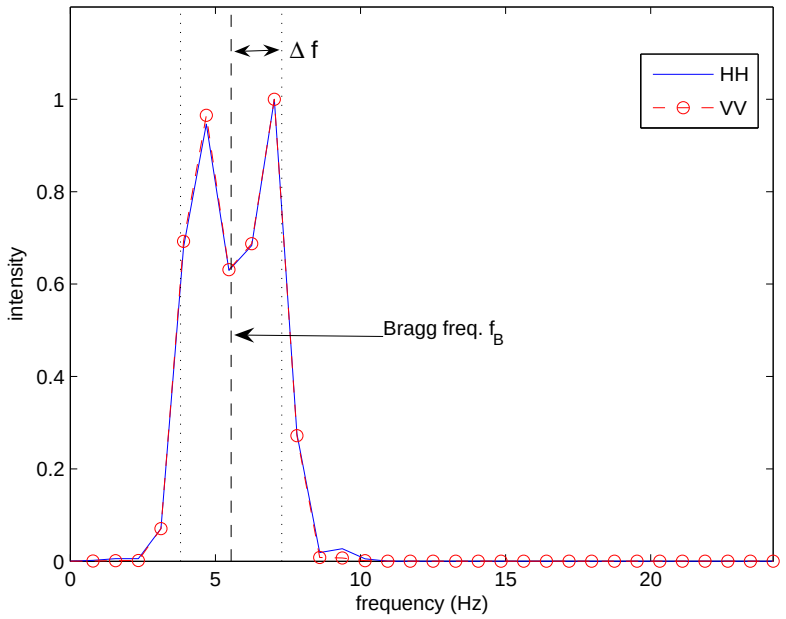

Figure 6.13: The range averaged polarized Doppler spectra

polarized numerical Doppler, and Δf denotes the Doppler width predicted by equation (6.34). It demonstrates that the numerical Doppler matches well with that from the analytical prediction. We note that the maximum Doppler intensity shifts to the edge rather than locating at the middle Bragg frequency point, a phenomenon for which there are two possible reasons. The first one is that the edges correspond to the long wave crest and trough regions, where the short Bragg waves have the highest energy compared to the other regions (the Doppler spectrum intensity is proportional

to the square of short wave amplitude). The second reason is that there is only one maximum located at the crest/trough against two maxima for each period range average.

From Figure 6.11, we can see that the range-resolved mean Doppler frequency variation indicates the orbital velocity of resolved waves. Therefore, such information can be used to retrieve the long waves. The orbital velocity U and the surface elevation η satisfy [88]

$$U = \int \omega(k)\eta e^{ikx} dk. \tag{6.43}$$

Therefore, the surface elevation η can be retrieved from U by Fast Fourier transform. The orbital velocity can be computed from the Doppler information. The Doppler centroid maps the evolution of the resolved waves [89], and it is calculated as

$$f_{DC} = \frac{\int f S(f) df}{\int S(f) df}, \tag{6.44}$$

where $S(f)$ denotes the Doppler spectrum at the frequency f. Figure 6.14 shows the polarized Doppler centroids and the surface retrievals, and indicates that the Doppler centroid is directly related to the long wave. Therefore, Doppler information can be used to resolve/retrieve the long wave. The retrieval results from both polarized Doppler centroids match very well with the original long wave profile, and their retrieval results are found to have a better accuracy than the retrieval result obtain from the two-scale model (see Figure 6.15). In order to study what effect the explicit slope of long wave have on the radar Doppler spectrum, a linear long wave is added in the modulated short wave surface. The numerical Doppler comparison between with an explicit long wave and that without a long wave is shown in Figure 6.16 and

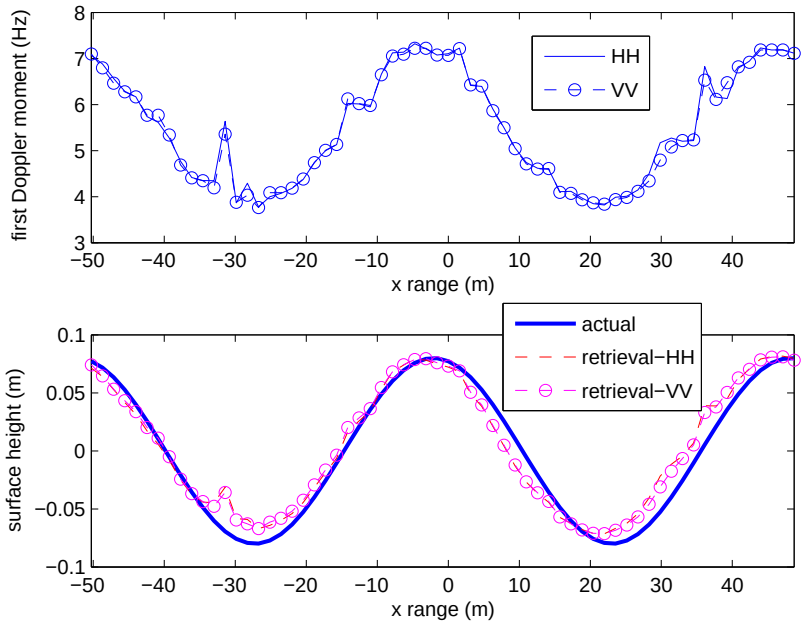

Figure 6.14: The polarized Doppler centroids comparisons (top) and long wave surface retrieval from the Doppler centroids information (bottom)

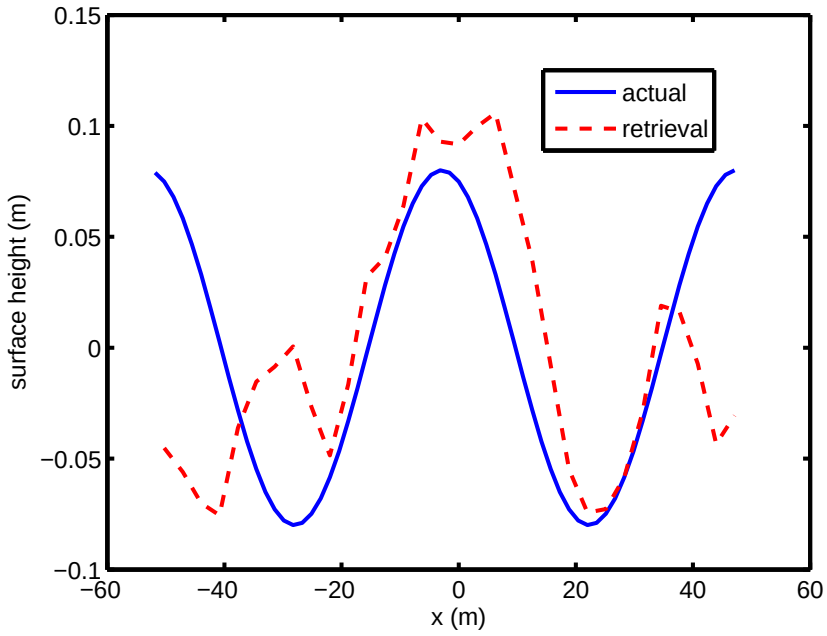

Figure 6.15: Long wave surface retrieval with use of the two-scale model

Figure 6.17. The results show that the long wave slope does not have an appreciable effect on the Doppler spectrum in both polarizations from both range-averaged Doppler and Doppler centroids comparisons as long as the long wave slope influence has been accounted for by the hydrodynamic modulation.

6.7 Conclusion

The time varying spectral coefficient of short waves is perturbed by the presence of long waves, which induce the perturbed Doppler shift. The coefficient is derived in equation (6.30) based on simplified nonlinear WW equations. The analytical short wave amplitude is derived explicitly. From this result, the theoretical Doppler frequency can be derived under the multiple scale approach. The analytical result and

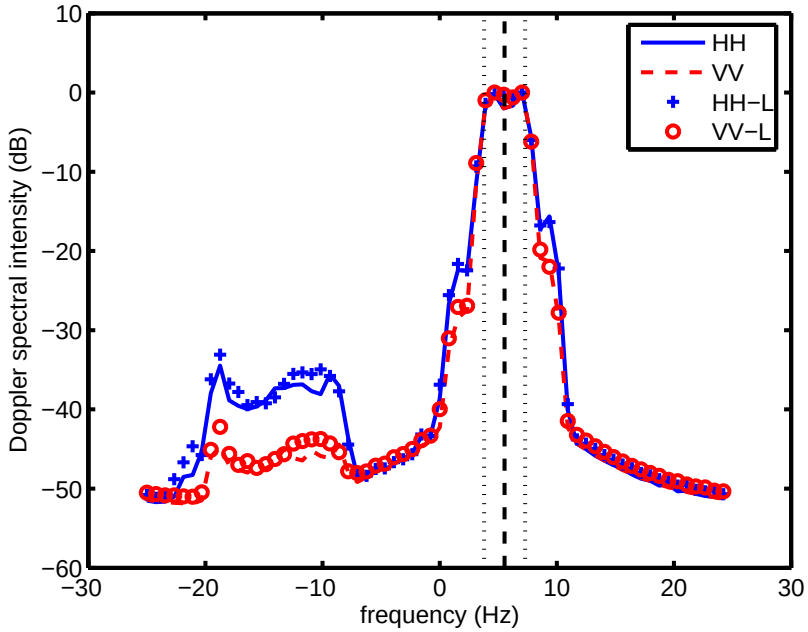

Figure 6.16: The polarized range averaged Doppler comparisons with and without explicit presence of long waves

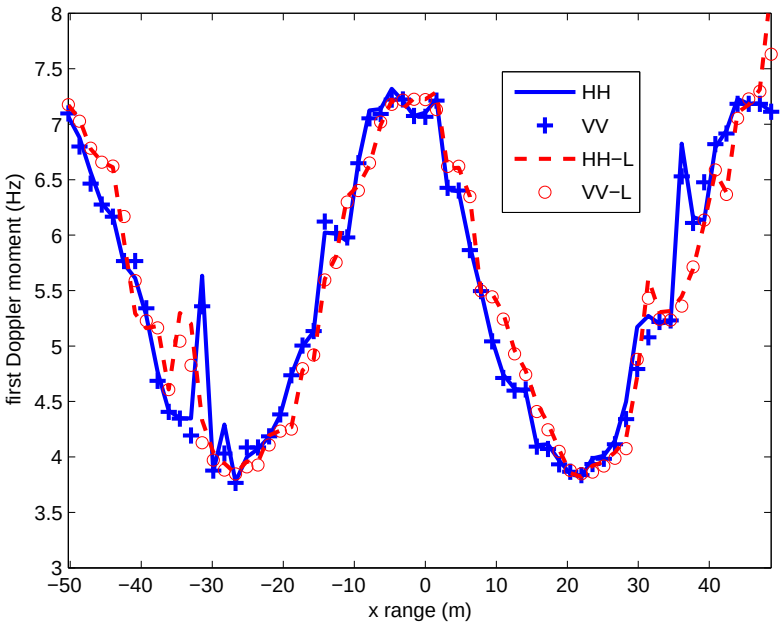

Figure 6.17: The polarized Doppler centroids comparisons with and without explicit presence of long waves

the simplified WW prediction are validated in several different cases. Those results demonstrate that the simplified WW equations can be applied to do Doppler analysis, as well as the analytically derived Doppler.

In addition, the range-resolved radar Doppler from the simplified WW equations was also analyzed. The numerical Doppler from these simplified WW equations is almost the same as that calculated from the original WW equations. The range average Doppler further validates the accuracy of the simplified WW equations. The first moment of Doppler (or Doppler centroid) can be directly converted to the orbital velocity of the presented long waves. This information is also a function of the long wave profile. Therefore, the surface retrieval from the Doppler information can be performed. This provides an alternative retrieval method to the scattering model retrieval that we studied in Chapter 3.

CHAPTER 7

CONCLUSIONS

This thesis has presented the ocean surface electromagnetic scattering study through the combination of numerical nonlinear hydrodynamics and computational electromagnetics. The results have shown that the combination can improve our understanding of radar observations over ocean surfaces. With respect to the goal of ocean surface electromagentic scattering study, this thesis has made the following major contributions:

- A new numerical method is developed to study the HMTF. It allows us to examine the theory in a controlled environment, without the need for empirical models of effects such as wind forcing and wave breaking.
- A new numerical method is developed to study the RMTF. It enables us to investigate the intermediate waves (the third scale) influence on RMTF.
- A novel analytical Doppler is derived based on hydrodynamics. It inherently includes the hydrodynamic modulation effect.
- A new numerical method is developed to study the nonlinear dispersion relation for modulated water waves

- TSM is found to be applicable for the retrieval of ocean surface profile with reasonable accuracy from LGA radar data, but Doppler retrievals are found to provide higher accuracy.

Several widely used analytical scattering models (SPM, KA, SSA, and TSM) are further investigated, and their prediction results of range-resolved RCS at the LGA are compared with the exact solution from MOM in Chapter 2. The results show that the difference between RCS at the LGA predicted by these analytical models and that by MOM is appreciable, in particular, for VV polarization, although most of these models predict accurate range-resolved RCS at small to moderate incidence angles. The difference is mainly caused by possible shadowing and multiple scattering. Although the second order SSA and NLSSA include some multiple scattering, TSM predicts batter scattering at the LGA. Our results also suggest that one forward and backward scattering iteration has to be performed to obtain accurate range resolved RCS at LGA.

The ocean surface profile retrieval study is presented in Chapter 3. This study uses the physical scattering model other than some commonly used empirical models. The principle is to retrieve the ocean surface profile from the range-resolved RCS. This is because the range-resolved RCS is a function of the local slope, which is directly related to the surface profile. The TSM model is applied to retrieve the ocean surface from HH polarization scattering field data. The results demonstrate that the model-based retrieval algorithm is applicable. With use of our retrieval algorithm, those parameters that influence the retrieval accuracy are further studied. The results retrieved also indicate that using a relative higher ocean surface wind speed can lead to better retrieval accuracies.

A numerical method to study the hydrodynamic modulation transfer function (HMTF) is described in Chapter 4. Using a numerical hydrodynamics code - called the "Watson-West" (WW) method - the modulation of those stochastic short waves by the presence of deterministic longer waves is numerically extracted by a "short-time" Fourier transform method. The nonlinear interaction (modulation) between the deterministic longer waves and those short waves is forced by the hydrodynamic equations, and the nonlinear initial conditions are simulated by a time "ramp-up" process. Our numerical HMTF results match well with those predicted by the analytical wave action theory. However, our numerical results are slightly higher than those analytical predictions. To further explore what causes the discrepancy, we propose a numerical water wave dispersion relationship. Our results further suggest that those classical approaches may ignore some higher order nonlinearity that may cause the difference between our numerical results and those analytical predictions.

Our numerical HMTF method is further applied to study the electromagnetic scattering from the nonlinear ocean surfaces in this study. The procedure to retrieve MTF (RMTF) and HMTF (RHMTF) and our results are described in Chapter 5. With use of this procedure, a narrow tapered incidence wave is chosen to obtain the localized RCS at first. Then, the numerical MTF from the time varying RCS can be extracted. Finally, the total numerical MTF (RMTF) and the numerical radar HMTF (RHMTF) can be obtained from a surface consisting of the long wave and short waves and a surface consisting of only modulated short waves, respectively. Our numerical radar TMTF (RTMTF) matches very well with that predicted by the two-scale model. We further studied the intermediate waves' influence on the MTF (the third scale effect) through varying of the band-limited short waves lower cutoff. Our

numerical results further demonstrate that the third-scale effect is essentially caused by the modulation of deterministic long waves to intermediate waves. The stochastic two-scale model and the empirical method are also applied to analyze the third-scale effect, and their results are compared with our numerical results. It turns out that the trend in our numerical intermediate waves' MTF and that their results are in agreement.

An analytical solution to retrieve the modulated short wave spectral amplitude is described in Chapter 6. It is based on the simplified "WW" equations. The nonlinearity is accounted for up to the first order in our analytical solution. Under two-scale time analysis, the formulation is approximated as the classical modulated dispersion formula. The formulation derived is validated by the comparison with the original "WW" solutions. The radar Doppler is also computed with use of the modulated and simplified "WW" solution. Through the frequency sweep technique, the range-resolved Doppler spectrum is obtained for both HH and VV polarizations. The results show that the simplified "WW" equations predict accurate Doppler spectra. The surface profile retrieval from the Doppler centroid (or first moment of the Doppler spectrum) is also investigated. The retrieval results demonstrate that the range resolved Doppler centroids indicate the long wave orbital velocity, which can be used to retrieve the surface profile accurately.

The nonlinearity of hydrodynamics plays an important role in understanding radar scattering signals from ocean surfaces. It is also a challenging problem in ocean microwave remote sensing. This thesis presents the application of the numerical hydrodynamics and computational electromagnetics to the study of radar RCS and the study of Doppler. There still remain some uncertainties, for example, the influence

of the intermediate waves' HMTF on the short Bragg waves. We need to improve the numerical hydrodynamics so that it can simulate wider "PM" short waves and a larger long wave slope. With the combination of hydrodynamics and electromagnetics, a deeper and better understanding of radar ocean signals can be achieved.

APPENDIX A

STUDIES OF THE MODULATION OF SHORT SEA WAVE BY SLOWLY VARYING CURRENTS

The interactions between short waves and slowly varying currents is of interest in ocean remote sensing. Chapter 4 shows the HMTF study between longer waves and short waves. Here, the HMTF between slowly varying currents and short waves are numerically examined. The details are presented as follows.

A.1 Basic equations

With the presence of a slowly varying horizontal surface current $\mathbf{u} = u\hat{x}$, the original WW equation [29] will be modified as [90]

$$\frac{\partial \eta}{\partial t} = -(\phi_s)_x \eta_x + W[1 + (\eta_x)^2] - \nabla_x(u\eta) \tag{A.1}$$

$$\frac{\partial \phi_s}{\partial t} = -g\eta - \frac{1}{2}((\phi_s)_x)^2 + \frac{1}{2}W^2[1 + (\eta_x)^2] - u_x(\phi_s)_x \tag{A.2}$$

The time-varying surfaces are generated from equations (A.1) and (A.2).

A.2 Simulation setup

The input current is given by

$$u(x) = \pm u_0 \sin(x), \tag{A.3}$$

where the sign depends on the propagation direction with respect to short waves, and u_0 is the amplitude.

The space domain is $[0, 2\pi)$ m, the space discretization $N = 1024$, the initial short wave wavenumber is $k_s \in [30, 170]$ rad/m, and the time step Δt=0.002 s with total time 40 s. The ensemble average number is still 1200. In addition, the ramp-up parameters are set for a=2 s and b=0.5 s.

A.3 Analytical approach to MTF with presence of currents

With the presence of a current U, the conservation form is given by [63]:

$$(U + \frac{c}{2})cE = \text{constant} = (U_0 + \frac{c_0}{2})c_0E_0, \tag{A.4}$$

where c and c_0 represent the phase velocity of the short waves at U and U_0, respectively, $c_g = \frac{c}{2}$ for gravity waves, and subscript 0 denotes quantities within the frame of motion with ${U_0}^2$, in particular, $U_0 = \langle U \rangle$, where the bracket denotes the average. We assume that

- a short waves packet with the P-M frequency spectrum $\bar{\phi}(\bar{\omega}_s) = \frac{\beta g^2}{\bar{\omega}_s^5} \exp(-\frac{0.74g^2}{k^2 U_{19.5}^4})$,
- unity of the exponential term since its variation is negligible with/without a slowly varying current and the bar denotes the equilibrium state.

Based on these two assumptions and followed the derivation presented in [91], we have

$$(U_0 + \frac{c_0}{2})c_0\bar{\phi}(\omega)d\omega = (U + \frac{c}{2})c\phi(\omega)d\omega, \tag{A.5}$$

[2]The reference coordinate is moving with uniform velocity U_0. If U_0 is not zero, we need to transform it to the static coordinate system. Actually, the change of physical quantities between a static and uniform moving coordinate is negligible.

where $\phi(\omega)$ denotes the spectrum with presence of the current. From equation (A.5), we obtain

$$\phi(\omega) = \frac{(\frac{c_0}{2} + U_0)c_0}{(\frac{c}{2} + U)c}\bar{\phi}(\omega). \tag{A.6}$$

Now, we need to make the conversion from the frequency spectrum to the wavenumber spectrum. For energy conservation, we have

$$\phi(\omega)d\omega = S(k_s)dk_s, \tag{A.7}$$

where $S(k_s)$ is the wavenumber spectrum with presence of the current, and

$$d\omega = (U + \frac{c}{2})dk_s \tag{A.8}$$

which is easy obtained from dispersion equation presented in previous chapter with $c_g = \frac{c}{2}$. From equation (A.6) and (A.7), we get

$$\begin{aligned}
S(k_s) &= (c_0/2 + U_0)\frac{c_0}{c}\bar{\phi}(\omega) \\
&= (c_0/2 + U_0)\frac{c_0}{c}\frac{\beta g^2}{\omega^5}\exp(...) && \text{(Substitute P-M spectrum)} \\
&= (c_0/2 + U_0)\frac{c_0}{c}\frac{\beta g^2}{\bar{k}_s^5(U + c)^5}\exp(...) && \text{(By } \omega = \omega_s + \bar{k}_s U\text{)} \\
&= \frac{(1 + 2U_0/c_0)}{(1 + U/c)^5}\left(\frac{c_0}{c}\right)^2\frac{\beta}{2}\frac{1}{\bar{k}_s^3}\exp(...) && \text{(By } g = \bar{k}_s c^2\text{)} \\
&\approx \frac{(1 + 2\gamma)}{(1 + \frac{U}{c_0}\frac{1}{\alpha})^5}\frac{1}{\alpha^2}\bar{S}(\bar{k}_s) && \text{(Define } \alpha = \frac{c}{c_0} \text{ and } \gamma = \frac{U_0}{c_0}\text{)},
\end{aligned} \tag{A.9}$$

where α is given by [88]

$$\alpha \equiv \frac{c}{c_0} = \frac{1}{2(1 + \gamma)}\left(1 + \sqrt{1 + \frac{4(1 + \gamma)U}{c_0}}\right), \tag{A.10}$$

where it requires $4(1 + \gamma)U/c_0 > -1$ and $|\gamma| < 1$. In addition, the exponential term variations in the above derivation (equation (A.9)) are ignored. Finally, the

wavenumber spectrum variation over space with presence of a current is given by

$$\frac{S}{\bar{S}} = \frac{(1+2\gamma)}{(1+\frac{U}{c_0}\frac{1}{\alpha})^5}\frac{1}{\alpha^2}. \tag{A.11}$$

Special case: if $U_0 = 0$, there is [91]

$$\begin{aligned}\frac{S}{\bar{S}} &= \frac{1}{(1+U/c)^7} \\ &= \frac{1}{[1+\frac{2U/c_0}{1+\sqrt{1+4U/c_0}}]^7}.\end{aligned} \tag{A.12}$$

In equation (A.12), if we make the assumption that $U/c_0 \ll 1$, then we expand it as

$$\frac{S}{\bar{S}} = 1 - 7\frac{U}{c_0} + O((\frac{U}{c_0})^2). \tag{A.13}$$

A.4 MTF extraction methods

We simulated several cases using equation (A.1) and (A.2), and obtained the localized spectrum $S(x_i, k_s, t)$, where x_i is the local space index (the total sub-space number is still 31), k_s is the short wave wavenumber, and t is the observed time.

In real numerical simulations, the group velocity of short waves has an effect on the spectrum variation. Thus, we need to remove the group velocity effect by using the steady property. The procedures are listed as follows:

1. calculate the localized spectrum average over space and time, get the spectrum $\bar{S}(k_s) =<< S(x_i, k_s, t) >_{x_i}>_t$, where the subscript x_i and t denote the average direction in x and t, respectively;

2. calculate the localized spectrum normalization $S_n(x_i, k_s, t) = S(x_i, k_s, t)/\bar{S}(k_s)$;

3. average over time for normalized local spectrum to remove the group velocity effect to get $S/\bar{S} = S_n(x_i, k_s) =< S_n(x_i, k_s, t) >_t$.

A.5 Results

Figure A.1 shows the localized spectrum, where the spectra are not calibrated by the ensemble number and the coefficient of FFT. Figure A.2 and A.3 show the spectrum variation and the comparison to the analytical approach, where the legend N inside the bracket denotes the *numerical*, and legend T is the *theoretical*, i.e., equation (A.12).

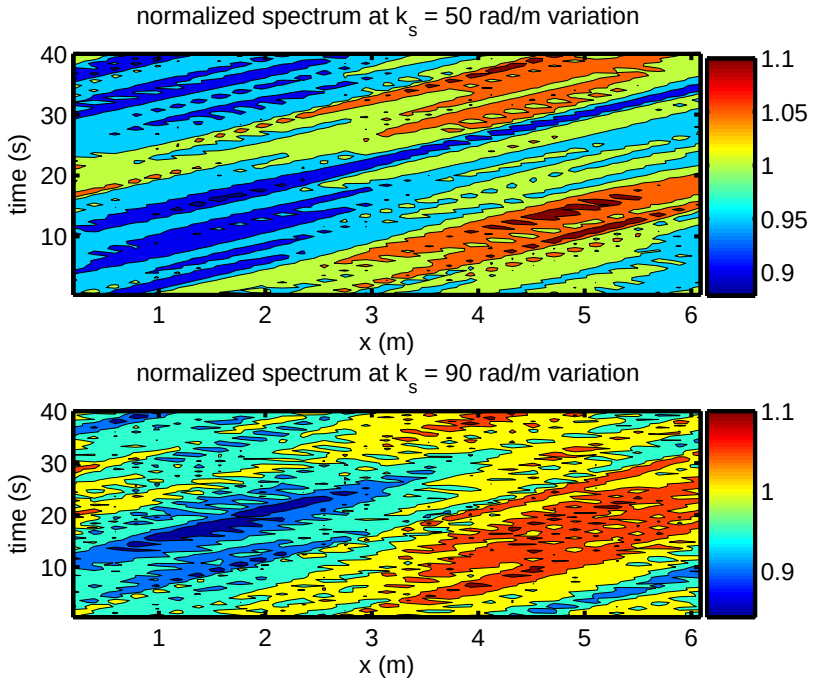

Figure A.1: Normalized short wave spectrum variation over space and time

A.6 Conclusion

Both numerical results and theoretical predictions of the spectrum variation of short waves with the presence of a slowly varying current match very well.

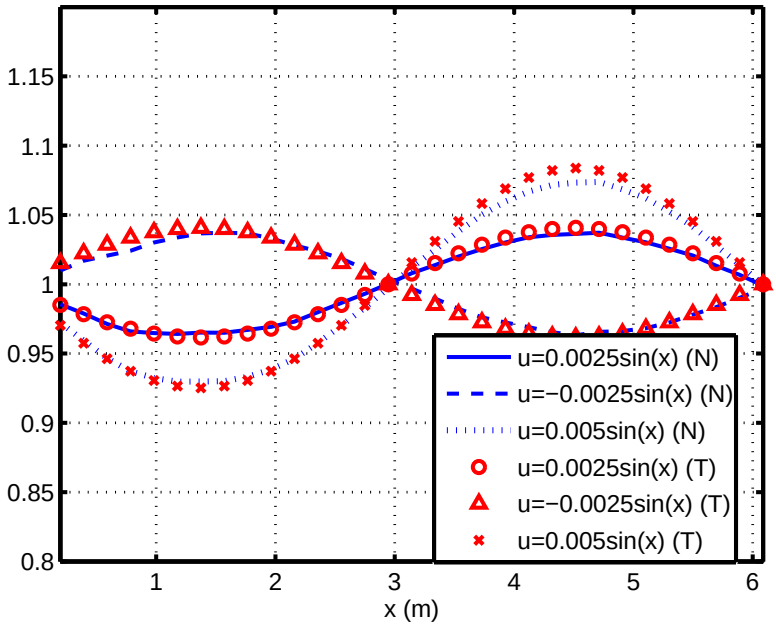

Figure A.2: Normalized spectrum variation over time at $k_s = 50$ rad/m

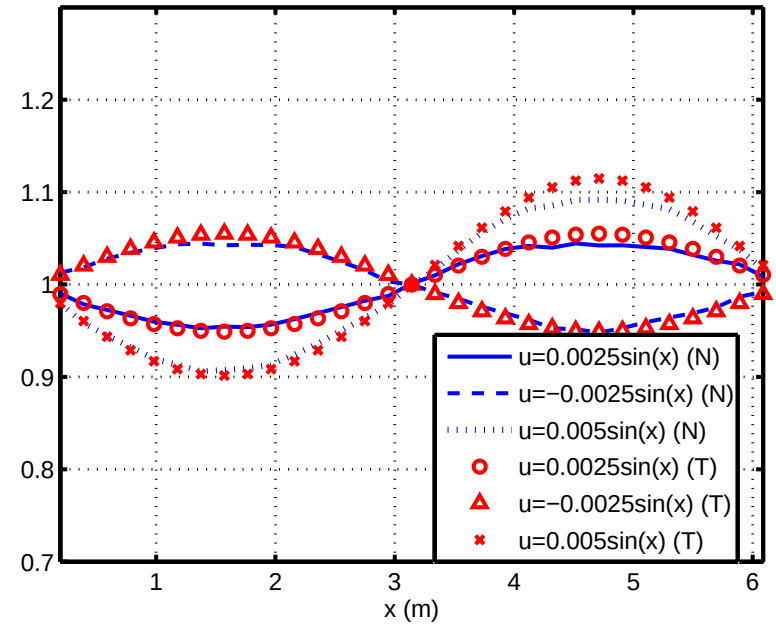

Figure A.3: Normalized spectrum variation over time at $k_s = 90$ rad/m

APPENDIX B

DERIVATION OF DETAILED DOPPLER ANALYSIS

B.1 Derivation of simplified short wave evolution

For short waves, we assume that

$$\eta_S(x,t) = \sum_{n=-\infty}^{\infty} a_S^n(t) e^{ik_S^n x}, \tag{B.1}$$

$$\phi_S(x,t) = \sum_{n=-\infty}^{\infty} b_S^n(t) e^{ik_S^n x}, \tag{B.2}$$

where $a_S^n = (a_S^{-n})^*$, $b_S^n = (b_S^{-n})^*$.Then, we have

$$\nabla\eta_L = \sum_m ik_L^m a_L^m e^{i(k_L^m x - \omega_L^m t + \theta_m)}, \tag{B.3}$$

$$\nabla\phi_L = \sum_m ik_L^m b_L^m e^{i(k_L^m x - \omega_L^m t + \theta_m)}, \tag{B.4}$$

$$W_{0L} = \sum_m |k_L^m| b_L^m e^{i(k_L^m x - \omega_L^m t + \theta_m)}, \tag{B.5}$$

$$\nabla\eta_S = \sum_n ik_S^n a_S^n(t) e^{ik_S^n x}, \tag{B.6}$$

$$\nabla\phi_S = \sum_n ik_S^n b_S^n(t) e^{ik_S^n x}, \tag{B.7}$$

$$W_{0S} = \sum_n |k_S^n| b_S^n(t) e^{ik_S^n x}, \tag{B.8}$$

and

$$\frac{\partial \phi_S}{\partial t} = \sum_n b_S^n(t)' e^{ik_S^n x}, \tag{B.9}$$

$$\frac{\partial \eta_S}{\partial t} = \sum_n a_S^n(t)' e^{ik_S^n x}, \tag{B.10}$$

$$\eta_S \kappa \phi_L = \sum_{m,n} |k_L^m| a_S^n(t) b_L^m e^{i(k_S^n + k_L^m)x} e^{-i\omega_L^m t + i\theta^m}, \tag{B.11}$$

$$\eta_L \kappa \phi_S = \sum_{m,n} |k_S^n| a_L^m b_S^n(t) e^{i(k_S^n + k_L^m)x} e^{-i\omega_L^m t + i\theta^m}, \tag{B.12}$$

$$\kappa(\eta_S \kappa \phi_L) = \sum_{m,n} |k_L^m||k_L^m + k_S^n| a_S^n(t) b_L^m e^{i(k_S^n + k_L^m)x} e^{-i\omega_L^m t + i\theta^m}, \tag{B.13}$$

$$\kappa(\eta_L \kappa \phi_S) = \sum_{m,n} |k_S^n||k_L^m + k_S^n| a_L^m b_S^n(t) e^{i(k_S^n + k_L^m)x} e^{-i\omega_L^m t + i\theta^m}, \tag{B.14}$$

$$\eta_L \kappa^2 \phi_S = \sum_{m,n} (k_S^n)^2 a_L^m b_S^n(t) e^{i(k_S^n + k_L^m)x} e^{-i\omega_L^m t + i\theta^m}, \tag{B.15}$$

$$\eta_S \kappa^2 \phi_L = \sum_{m,n} (k_L^m)^2 a_S^n(t) b_L^m e^{i(k_S^n + k_L^m)x} e^{-i\omega_L^m t + i\theta^m}. \tag{B.16}$$

Using above derivations, we have following intermediate results

$$W_{1S} = \sum_{m,n} \left(a_L^m b_S^n(t)|k_S^n| \left(|k_S^n| - |k_S^n + k_L^m|\right) + a_S^n(t) b_L^m |k_L^m| \left(|k_L^m| - |k_S^n + k_L^m|\right)\right) e^{i(k_S^n + k_L^m)x} e^{-i\omega_L^m t + i\theta^m}, \tag{B.17}$$

$$\nabla \eta_L \nabla \phi_S = -\sum_{m,n} k_L^m k_S^n a_L^m b_S^n(t) e^{i(k_S^n + k_L^m)x} e^{-i\omega_L^m t + i\theta^m}, \tag{B.18}$$

$$\nabla \eta_S \nabla \phi_L = -\sum_{m,n} k_L^m k_S^n a_S^n(t) b_L^m e^{i(k_S^n + k_L^m)x} e^{-i\omega_L^m t + i\theta^m}, \tag{B.19}$$

$$\nabla \phi_S \nabla \phi_L = -\sum_{m,n} k_L^m k_S^n b_L^m b_S^n(t) e^{i(k_S^n + k_L^m)x} e^{-i\omega_L^m t + i\theta^m}, \tag{B.20}$$

$$W_{0L} W_{0S} = \sum_{m,n} |k_L^m||k_S^n| b_L^m b_S^n(t) e^{i(k_S^n + k_L^m)x} e^{-i\omega_L^m t + i\theta^m}, \tag{B.21}$$

$$W_{1S} - (\nabla\eta_L \nabla\phi_S + \nabla\eta_S \nabla\phi_L) = \sum_{m,n} (|k_L^m| \, (|k_L^m| - |k_S^n + k_L^m|) + k_S^n k_L^m) \\ a_S^n(t) b_L^m e^{i(k_S^n + k_L^m)x} e^{-i\omega_L^m t + i\theta^m}, \tag{B.22}$$

$$W_{0L} W_{0S} - \nabla\phi_S \nabla\phi_L = \sum_{m,n} (|k_L^m||k_S^n| + k_L^m k_S^n) \\ b_L^m b_S^n(t) e^{i(k_S^n + k_L^m)x} e^{-i\omega_L^m t + i\theta^m}. \tag{B.23}$$

B.2 Solution of the ODE

$$\frac{d\mathbf{B}(t)}{dt} \approx \mathbf{A}_0 \mathbf{B}(t) + \mathbf{A}_1(t)\mathbf{B}_0(t) \tag{B.24}$$

The particular solution B_1 of equation (B.24) is written by [92]

$$\mathbf{B}_1 = \mathbf{X} \int_{t_0}^{t} ds \mathbf{X}^{-1}(s)[\mathbf{A}_1(s)\mathbf{B}_0(s)], \tag{B.25}$$

where the matrix $\mathbf{X}$ is the fundamental matrix of the system equation (B.24). The p^{th} column of fundamental matrix $\mathbf{X}$ consists of $e^{\lambda_p t}\mathbf{e}_p$. Eventually, the $\mathbf{X}$ is a diagonal 2x2 block matrix as following:

$$\mathbf{X} = \begin{bmatrix} \mathbb{X}_{11} & 0 & ... & 0 & 0 \\ 0 & \mathbb{X}_{22} & ... & 0 & 0 \\ ... & ... & ... & ... & ... \\ 0 & 0 & ... & \mathbb{X}_{2N,2N} & 0 \\ 0 & 0 & ... & 0 & \mathbb{X}_{2N+1,2N+1} \end{bmatrix},$$

where

$$\mathbb{X}_{pp} = \begin{bmatrix} -\frac{g}{\sqrt{-gk_S^{n+N+1-p}}} e^{i\sqrt{gk_S^{n+N+1-p}}t} & \frac{g}{\sqrt{-gk_S^{n+N+1-p}}} e^{-i\sqrt{gk_S^{n+N+1-p}}t} \\ e^{i\sqrt{gk_S^{n+N+1-p}}t} & e^{-i\sqrt{gk_S^{n+N+1-p}}t} \end{bmatrix}.$$

.

Now, we calculate the particular solution step by step. $\mathbf{A}_1(s)\mathbf{B}_0(s)$ is a column matrix with $4N+2$ elements. It consists of $2N+1$ (2x1) column matrix $\mathbf{F}_p$ ($p \in$

$[1, 2N+1]$) [3], where

$$\mathbf{F}_p(t) = \begin{bmatrix} \sum_{m=1}^{M}(-\omega_L^m a_L^m)k_S^{n+N-m+1-p} a_S^{n+N-m+1-p}(t_0)\frac{g}{\sqrt{-gk_S^{n+N-m+1-p}}} \\ e^{-i\sqrt{gk_S^{n+N-m+1-p}}t}e^{-i\omega_L^m t+i\theta^m} \\ \sum_{m=1}^{M}(-\omega_L^m a_L^m)(k_L^m - k_S^{n+N+m+1-p})a_S^{n+N+1-p+m}(t_0)e^{-i\sqrt{gk_S^{n+N+m+1-p}}t} \\ e^{i\omega_L^m t-i\theta^m} \end{bmatrix}.$$

$\mathbf{X}^{-1}$ is a diagonal 2x2 matrix $(4N+2)$ as

$$\mathbf{X}^{-1} = \begin{bmatrix} \mathbb{Y}_{11} & 0 & ... & 0 & 0 \\ 0 & \mathbb{Y}_{22} & ... & 0 & 0 \\ ... & ... & ... & ... & ... \\ 0 & 0 & ... & \mathbb{Y}_{2N,2N} & 0 \\ 0 & 0 & ... & 0 & \mathbb{Y}_{2N+1,2N+1} \end{bmatrix},$$

where

$$\mathbb{Y}_{pp} = \frac{1}{2}\begin{bmatrix} \frac{k_S^{n+N+1-p}}{\sqrt{-gk_S^{n+N+1-p}}}e^{-i\sqrt{gk_S^{n+N+1-p}}t} & e^{-i\sqrt{gk_S^{n+N+1-p}}t} \\ -\frac{k_S^{n+N+1-p}}{\sqrt{-gk_S^{n+N+1-p}}}e^{i\sqrt{gk_S^{n+N+1-p}}t} & e^{i\sqrt{gk_S^{n+N+1-p}}t} \end{bmatrix}.$$

Then, we have

$$\int_{t_0}^{t} ds\mathbf{X}^{-1}\mathbf{A}_1(s)\mathbf{B}_0(s) = \frac{1}{2}\sum_{m=1}^{M}(\omega_L^m a_L^m)\int_{t_0}^{t} ds\begin{bmatrix} I^U(s) \\ I^D(s) \end{bmatrix}, \tag{B.26}$$

where the p^{th} element of $I^U(s)$ and $I^D(s)$ are given, respectively,

$$\begin{aligned} I_p^U(s) = &-\frac{gk_S^{n+N+1-p}k_S^{n+N+1-p-m}e^{i\theta^m}}{\sqrt{-gk_S^{n+N+1-p}}\sqrt{-gk_S^{n+N+1-p-m}}}a_S^{n+N+1-p-m}(t_0) \\ &e^{-i(\sqrt{gk_S^{n+N+1-p}}+\sqrt{gk_S^{n+N+1-p-m}}+\omega_L^m)s} \\ &-(k_L^m - k_S^{n+N+1-p+m})a_S^{n+N+1-p+m}(t_0)e^{-i\theta^m} \\ &e^{-i(\sqrt{gk_S^{n+N+1-p}}+\sqrt{gk_S^{n+N+1-p+m}}-\omega_L^m)s}, \end{aligned} \tag{B.27}$$

$$\begin{aligned} I_p^D(s) = &\frac{gk_S^{n+N+1-p}k_S^{n+N+1-p-m}e^{i\theta^m}}{\sqrt{-gk_S^{n+N+1-p}}\sqrt{-gk_S^{n+N+1-p-m}}}a_S^{n+N+1-p-m}(t_0) \\ &e^{-i(-\sqrt{gk_S^{n+N+1-p}}+\sqrt{gk_S^{n+N+1-p-m}}+\omega_L^m)s} \\ &-(k_L^m - k_S^{n+N+1-p+m})a_S^{n+N+1-p+m}(t_0)e^{-i\theta^m} \\ &e^{-i(-\sqrt{gk_S^{n+N+1-p}}+\sqrt{gk_S^{n+N+1-p+m}}-\omega_L^m)s}. \end{aligned} \tag{B.28}$$

[3]If any term including index $n+N+1-p+m$ or $n+N+1-p-m$ is out of bound $n+N$ or $n-N$, respectively, its coefficient is zero.

Integrating them, we get

$$\int_{t_0}^{t} ds \mathbf{X}^{-1}\mathbf{A}_1(s)\mathbf{B}_0(s) = \frac{1}{2}\sum_{m=1}^{M}(\omega_L^m a_L^m)\begin{bmatrix} II^U(t) \\ II^D(t)\end{bmatrix}, \tag{B.29}$$

where the p^{th} element of $II^U(s)$ and $II^D(s)$ are given, respectively,

$$\begin{aligned} II_p^U(t) = & \frac{gk_S^{n+N+1-p}k_S^{n+N+1-p-m}e^{i\theta^m}}{\sqrt{-gk_S^{n+N+1-p}}\sqrt{-gk_S^{n+N+1-p-m}}}\frac{a_S^{n+N+1-p-m}(t_0)}{i(\sqrt{gk_S^{n+N+1-p}}+\sqrt{gk_S^{n+N+1-p-m}}+\omega_L^m)} \\ & \left[e^{-i(\sqrt{gk_S^{n+N+1-p}}+\sqrt{gk_S^{n+N+1-p-m}}+\omega_L^m)t} - e^{-i(\sqrt{gk_S^{n+N+1-p}}+\sqrt{gk_S^{n+N+1-p-m}}+\omega_L^m)t_0}\right] \\ & - \frac{e^{-i\theta^m}(k_L^m - k_S^{n+N+1-p+m})}{-i(\sqrt{gk_S^{n+N+1-p}}+\sqrt{gk_S^{n+N+1-p+m}}-\omega_L^m)}a_S^{n+N+1-p+m}(t_0) \\ & \left[e^{-i(\sqrt{gk_S^{n+N+1-p}}+\sqrt{gk_S^{n+N+1-p+m}}-\omega_L^m)t} - e^{-i(\sqrt{gk_S^{n+N+1-p}}+\sqrt{gk_S^{n+N+1-p+m}}-\omega_L^m)t_0}\right], \end{aligned} \tag{B.30}$$

$$\begin{aligned} II_p^D(t) = & \frac{gk_S^{n+N+1-p}k_S^{n+N+1-p-m}e^{i\theta^m}}{\sqrt{-gk_S^{n+N+1-p}}\sqrt{-gk_S^{n+N+1-p-m}}}\frac{a_S^{n+N+1-p-m}(t_0)}{i(\sqrt{gk_S^{n+N+1-p}}-\sqrt{gk_S^{n+N+1-p-m}}-\omega_L^m)} \\ & \left[e^{-i(-\sqrt{gk_S^{n+N+1-p}}+\sqrt{gk_S^{n+N+1-p-m}}+\omega_L^m)t} - e^{i(\sqrt{gk_S^{n+N+1-p}}-\sqrt{gk_S^{n+N+1-p-m}}-\omega_L^m)t_0}\right] \\ & - \frac{e^{-i\theta^m}(k_L^m - k_S^{n+N+1-p+m})}{-i(-\sqrt{gk_S^{n+N+1-p}}+\sqrt{gk_S^{n+N+1-p+m}}-\omega_L^m)}a_S^{n+N+1-p+m}(t_0) \\ & \left[e^{-i(-\sqrt{gk_S^{n+N+1-p}}+\sqrt{gk_S^{n+N+1-p+m}}-\omega_L^m)t} - e^{i(\sqrt{gk_S^{n+N+1-p}}-\sqrt{gk_S^{n+N+1-p+m}}+\omega_L^m)t_0}\right]. \end{aligned} \tag{B.31}$$

The particular solution is given by

$$\mathbf{X}\int_{t_0}^{t} ds \mathbf{X}^{-1}\mathbf{A}_1(s)\mathbf{B}_0(s) = \frac{1}{2}\sum_{m=1}^{M}(\omega_L^m a_L^m)\begin{bmatrix} III^U(t) \\ III^D(t)\end{bmatrix}, \tag{B.32}$$

where the p^{th} element of $III^U(s)$ and $III^D(s)$ are given, respectively,

$$\begin{aligned} III_p^U(t) = & -\frac{g}{\sqrt{-gk_S^{n+N+1-p}}}e^{i\sqrt{gk_S^{n+N+1-p}}t}II_p^U(t) \\ & + \frac{g}{\sqrt{-gk_S^{n+N+1-p}}}e^{-i\sqrt{gk_S^{n+N+1-p}}t}II_p^D(t), \end{aligned} \tag{B.33}$$

$$III_p^D(t) = e^{i\sqrt{gk_S^{n+N+1-p}}t}II_p^U(t) + e^{-i\sqrt{gk_S^{n+N+1-p}}t}II_p^D(t). \tag{B.34}$$

Further simplifying III^U and III^D with only positive propagation waves, we obtain

$$\begin{aligned}
III_p^U(t) = & \frac{g}{\sqrt{-gk_S^{n+N+1-p}}} \\
& \Bigg[\frac{gk_S^{n+N+1-p}k_S^{n+N+1-p-m}e^{i\theta^m}a_S^{n+N+1-p-m}(t_0)}{\sqrt{-gk_S^{n+N+1-p}}\sqrt{-gk_S^{n+N+1-p-m}}} \\
& \frac{i2(\sqrt{gk_S^{n+N+1-p}}+\omega_L^m)e^{-i(\sqrt{gk_S^{n+N+1-p-m}}+\omega_L^m)t}}{(\sqrt{gk_S^{n+N+1-p-m}}+\omega_L^m)^2-gk_S^{n+N+1-p}} \\
& -(k_L^m-k_S^{n+N+1-p+m})a_S^{n+N+1-p+m}(t_0)e^{-i\theta^m} \\
& \frac{i2\sqrt{gk_S^{n+N+1-p}}e^{-i(\sqrt{gk_S^{n+N+1-p+m}}-\omega_L^m)t}}{(\sqrt{-gk_S^{n+N+1-p+m}}-\omega_L^m)^2-gk_S^{n+N+1-p}}\Bigg] \\
& +C^U e^{-i\sqrt{gl_S^{n+N+1-p}}t},
\end{aligned} \tag{B.35}$$

$$\begin{aligned}
III_p^D(t) = & \frac{gk_S^{n+N+1-p}k_S^{n+N+1-p-m}e^{i\theta^m}a_S^{n+N+1-p-m}(t_0)}{\sqrt{-gk_S^{n+N+1-p}}\sqrt{-gk_S^{n+N+1-p-m}}} \\
& \frac{i2\sqrt{gk_S^{n+N+1-p}}e^{-i(\sqrt{gk_S^{n+N+1-p-m}}+\omega_L^m)t}}{(\sqrt{gk_S^{n+N+1-p-m}}+\omega_L^m)^2-gk_S^{n+N+1-p}} \\
& -(k_L^m-k_S^{n+N+1-p+m})a_S^{n+N+1-p+m}(t_0)e^{-i\theta^m} \\
& \frac{i2(\sqrt{gk_S^{n+N+1-p+m}}-\omega_L^m)e^{-i\sqrt{gk_S^{n+N+1-p+m}}-\omega_L^m)t}}{(\sqrt{-gk_S^{n+N+1-p+m}}-\omega_L^m)^2-gk_S^{n+N+1-p}} \\
& +C^D e^{-i\sqrt{gk_S^{n+N+1-p}}t},
\end{aligned} \tag{B.36}$$

where C^U and C^D are constants related to the initial conditions.

B.3 Higher order approximation to analytical coefficients

Chapter 6 presents the first-order perturbed approach. To obtain higher accuracy, we extend this perturbation up to second order. Rewrite equation (B.24) as

$$\frac{d\mathbf{B}(t)}{dt} \approx \mathbf{A}_0\mathbf{B}(t) + \mathbf{A}_1(t)\left[\mathbf{B}_0(t)+\mathbf{B}_1(t)\right], \tag{B.37}$$

where $\mathbf{B}_1$ is the perturbed solution. The p^{th} element of $\mathbf{B}_1$ is written by

$$\mathbf{B}_{1p} = \frac{1}{2}\sum_{m=1}^{M} \omega_L^m a_L^m \begin{bmatrix} c_{p,m}^U a_S^{n+N+1-p-m}(t_0) e^{-i(\sqrt{gk_S^{n+N+1-p-m}}+\omega_L^m)} \\ +d_{p,m}^U a_S^{n+N+1-p+m}(t_0) e^{-i(\sqrt{gk_S^{n+N+1-p+m}}-\omega_L^m)} \\ c_{p,m}^D a_S^{n+N+1-p-m}(t_0) e^{-i(\sqrt{gk_S^{n+N+1-p-m}}+\omega_L^m)} \\ +d_{p,m}^D a_S^{n+N+1-p+m}(t_0) e^{-i(\sqrt{gk_S^{n+N+1-p+m}}-\omega_L^m)} \end{bmatrix},$$

where $c_{p,m}^U$, $d_{p,m}^U$, $c_{p,m}^D$, and $d_{p,m}^D$ are determined from equations (B.35) and (B.36). Then, the additional forcing term is written by

$$\widetilde{\mathbf{AB}}_p(t) = \sum_{m=1}^{M}(-\omega_L^m a_L^m) \begin{bmatrix} k_S^{n+N-m+1-p}[c_{p,m}^U a_S^{n+N-m+1-p}(t_0) \\ e^{-i(\sqrt{gk_S^{n+N+1-p-m}}+\omega_L^m)t} \\ +d_{p,m}^U a_S^{n+N+1-p+m}(t_0) \\ e^{-i(\sqrt{gk_S^{n+N+1-p+m}}-\omega_L^m)t}]e^{-i\omega_L^m t+i\theta^m} \\ (k_L^m - k_S^{n+N+m+1-p})[c_{p,m}^D a_S^{n+N+1-p-m}(t_0) \\ e^{-i(\sqrt{gk_S^{n+N+1-p-m}}+\omega_L^m)t} \\ +d_{p,m}^D a_S^{n+N+1-p+m}(t_0) e^{-i(\sqrt{gk_S^{n+N+1-p+m}}-\omega_L^m)t}] \\ e^{i\omega_L^m t-i\theta^m} \end{bmatrix}.$$

After some manipulations, we obtain the second-order perturbed solution

$$\begin{aligned} \tilde{b}_{n+N+1-p}(t) &= c_{p,m}^a a_S^{n+N+1-p-m}(t_0) e^{-i(\sqrt{gk_S^{n+N+1-p-m}}+2\omega_L^m)t} \\ &+ c_{p,m}^b a_S^{n+N+1-p-m}(t_0) e^{-i(\sqrt{gk_S^{n+N+1-p+m}}-2\omega_L^m)t} \\ &+ c_{p,m}^c a_S^{n+N+1-p+m}(t_0) e^{-i\sqrt{gk_S^{n+N+1-p+m}}t} \\ &+ c_{p,m}^d a_S^{n+N+1-p-m}(t_0) e^{-i\sqrt{gk_S^{n+N+1-p-m}}t}, \end{aligned} \tag{B.38}$$

$$\begin{aligned} \tilde{a}_{n+N+1-p}(t) &= d_{p,m}^a a_S^{n+N+1-p-m}(t_0) e^{-i(\sqrt{gk_S^{n+N+1-p-m}}+2\omega_L^m)t} \\ &+ d_{p,m}^b a_S^{n+N+1-p-m}(t_0) e^{-i(\sqrt{gk_S^{n+N+1-p+m}}-2\omega_L^m)t} \\ &+ d_{p,m}^c a_S^{n+N+1-p+m}(t_0) e^{-i\sqrt{gk_S^{n+N+1-p+m}}t} \\ &+ d_{p,m}^d a_S^{n+N+1-p-m}(t_0) e^{-i\sqrt{gk_S^{n+N+1-p-m}}t}. \end{aligned} \tag{B.39}$$

where $c_{p,m}^{a,b,c,d}$ and $d_{p,m}^{a,b,c,d}$ are constants. The second-order modifications (equations (B.38) and (B.39)) are too complicated. The results are not presented in this study.

BIBLIOGRAPHY

[1] P. H. Y. Lee, J. D. Barter, K. L. Beach, C. L. Hindman, B. M. Lake, H. Rungaldier, J. C. Shelton, A. B. Williams, R. Yee, and H. C. Tuen. X band microwave backscattering from ocean waves. *J. Geophys. Res.*, 100(C2):2591–2611, 1995.

[2] A. D. Rozenberg, D. C. Quigley, and W. K. Melville. Laboratory study of polarized scattering by surface waves at grazing incidence: Part I - wind waves. *IEEE Trans. Geosci. Remote Sens.*, 33(4):1037–1046, 1995.

[3] A. D. Rozenberg, D. C. Quigley, and W. K. Melville. Laboratory study of polarized scattering by surface waves at grazing incidence: the influence of long waves. *IEEE Trans. Geosci. Remote Sens.*, 34(6):1331–1342, 1996.

[4] P. H. Y. Lee, J. D. Barter, K. L. Beach, C. L. Hindman, B. M. Lake, H. Rungaldier, H. R. Thompson Jr., and R. Yee. Experiments on Bragg and non-Bragg scattering using single- frequency and chirped radars. *Radio Sci.*, 32(5):1725–1744, 1997.

[5] C. L. Rino, E. Eckert, A. Siegel, T. Webster, A. Ochadlick, M. Rankin, and J. Davis. X-band low-grazing-angle ocean backscatter obtained during LOGAN 1993. *IEEE J. Ocean. Engineer.*, 22(1):18–26, 1997.

[6] J. Fuchs, D. Regas, T. Waseda, S. Welch, and M. D. Tulin. Correlation of hydrodynamic features with LGA radar backscatter from breaking waves. *IEEE Trans. Geosci. Remote Sens.*, 37(5):2442–2460, 1999.

[7] M. A. Sletten, J. C. West, X. Liu, and J. H. Duncan. Radar investigations of breaking water waves at low grazing angles with simultaneous high-speed optical imagery. *Radio Sci.*, 38(6):1110, doi:10.1029/2002RS002716, 2003.

[8] D. E. Barrick. Near-grazing illumination and shadowing of rough surfaces. *Radio Sci.*, 30(3):563–580, 1995.

[9] M. I. Charnotskii. Wave scattering by periodic surface at low grazing angles: single grazing mode. *Progress in Electromagnetics Research*, 26:1–41, 2000.

[10] A. G. Voronovich. *Wave Scattering from Rough Surfaces*. Springer-Verlag, Berlin, Germany, 1994.

[11] E. I. Thorsos and S. L. Broschat. An investigation of the small slope approximation for scattering from rough surfaces. part I. thoery. *J. Acoust. Soc. Am.*, 97(4):2082–2093, 1995.

[12] A. G. Voronovich. Non-local small-slope approximation for wave scattering from rough surfaces. *Waves Random Media*, 6:151–167, 1996.

[13] S. L. Broschat and E. I. Thorsos. An investigation of the small slope approximation for scattering from rough surfaces. part II. numerical studies. *J. Acoust. Soc. Am.*, 101(5):2615–2625, 1997.

[14] S. L. Broschat. Reflection loss from a "Pierson-Moskowitz" sea surface using the nonlocal small slope approximation. *IEEE Trans. Geosci. Remote Sens.*, 37(1):632–634, 1999.

[15] H. Kim and J. T. Johnson. Radar images of rough surface scattering: Comparison of numerical and analytical models. *IEEE Trans. Antennas Propagat.*, 50(2):94–100, 2002.

[16] M. J. Smith, E. M. Poulter, and J. A. McGregor. Doppler radar measurements of wave groups and breaking waves. *J. Geophys. Res.*, 101(C6):14269–14282, 1996.

[17] P. H. Y. Lee, J. D. Barter, K. L. Beach, B. M. Lake, H. Rungaldier, H. R. Thompson Jr., L. Wang, and R. Lee. What are mechanism for non-Bragg scattering from water wave surfaces? *Radio Sci.*, 34(1):123–138, 1999.

[18] E. A. Caponi, B. M. Lake, and H. C. Yuen. Hydrodynamic effects in low-grazing angle backscattering from the ocean. *IEEE Trans. Antennas Propagat.*, 47(2):354–363, 1999.

[19] W. J. Plant. A model for microwave Doppler sea return at high incidence angles: Bragg scattering from bound, tilted waves. *J. Geophys. Res.*, 102(C9):21131–21146, 1997.

[20] D. B. Trizna. A model for Brewster angle damping and multipath effects on the microwave radar sea eacho at low grazing angles. *IEEE Trans. Geosci. Remote Sens.*, 35(5):1232–1244, 1997.

[21] J. C. West. Effect of shadowing on electromagnetic scattering from rough ocean wavelike surfaces at small grazing angles. *IEEE Trans. Geosci. Remote Sens.*, 35(2):293–301, 1997.

[22] J. V. Toporkov and G. S. Brown. Numerical simulations of scattering from time-varying, randomly rough surfaces. *IEEE Trans. Geosci. Remote Sens.*, 38(4):1616–1625, 2000.

[23] J. T. Johnson, J. V. Toporkov, and G. S. Brown. A numerical study of backscattering from time-evolving sea surfaces: comparison of hydrodynamic models. *IEEE Trans. Geosci. Remote Sens.*, 39(11):2411–2420, 2001.

[24] T. Hara and W. J. Plant. Hydrodynamic modulation of short wind-wave spectra by long waves and its measurement using microwave backscatter. *J. Geophys. Res.*, 99(C5):9767–9784, 1994.

[25] W. Alpers and K. Hasselmann. The two-frequency microwave technique for measuring ocean-wave spectra from an airplane or statellite. *Boundary Layer Meteorol.*, 13:215–230, 1978.

[26] B. A. Hughes. The effect of internal waves on surface wind waves: Theoretical analysis. *J. Geophys. Res.*, 83 (C1):455–465, 1978.

[27] E. A. Caponi, D. R. Crawford, and H. C. Yuen. Modulation of radar backscatter from the ocean by a variable surface current. *J. Geophys. Res.*, 93(C10):12249–12263, 1988.

[28] T. Elfouhaily, D. R. Thompson, D. Vandemark, and B. Chapron. Higher-order hydrodynamic modulation: theory and applications for ocean waves. *Proc. R. Soc. Lond. A*, 457:2585–2608, 2001.

[29] B. J. West, K. Brueckner, and R. S. Janda. A numerical method for sea surface hydrodynamics. *J. Geophys. Res.*, 92:11803–11824, 1987.

[30] D. B. Creamer, F. Henyey, R. Schult, and J. Wright. Improved linear representation of ocean surface waves. *J. Fluid Mech.*, 205:135–161, 1989.

[31] C. L. Rino, T. L. Crystal, A. K. Koide, H. D. Ngo, and H. Guthart. Numerical simulation of backscatter from linear and nonlinear ocean surface realizations. *Radio Sci.*, 26(1):51–71, 1991.

[32] A. R. Hayslip, J. T. Johnson, and G. R. Baker. Further numerical studies of backscattering from time evolving non-linear sea surfaces. *IEEE Trans. Geosci. Remote Sens.*, 41(10):2287–2293, 2003.

[33] H. Masuko, K. Okamoto, M. Shimada, and S. Nima. Measurement of microwave backscattering signatures of the ocean surface using X band and K_a band airborne scatterometers. *J. Geophys. Res.*, 91(C11):13065–13083, 1986.

[34] W. C. Keller and W. J. Plant. Cross sections and modulation transfer functions at L and K_u bands measured during the tower ocean wave and radar dependence experiment. *J. Geophys. Res.*, 95(C9):16277–16289, 1990.

[35] D. Hauser, G. Caudal, and L. K. Shay. Behavior of the ocean radar cross-section at low incidence, observed in the vicinity of the Gulf stream. *IEEE Trans. Geosci. Remote Sens.*, 33(1):162–170, 1995.

[36] A. Schmidt, V. Wismann, R. Romesier, and W. Alpers. Simultaneous measurements of the ocean wave-radar modulation transfer function at L, C, and X bands from the research platform Nordsee. *J. Geophys. Res.*, 100(C5):8815–8827, 1995.

[37] V. Kudryavtsev, D. Hauser, G. Caudal, and B. Chapron. A semiempirical model of the normalized radar cross section of the sea surface, 2. radar modulation transfer function. *J. Geophys. Res.*, 108(C3):8055, doi:10.1029/2001JC001004, 2003.

[38] W. Alpers, D. B. Ross, and C. L. Rufenach. On the detectability of ocean surface waves by real and synthetic radar. *J. Geophys. Res.*, 86(C7):6481–6498, 1981.

[39] W. J. Plant. The modulation transfer function: concept and applications. In G. J. Komen and W. A. Oost, editors, *Radar Scattering from Modulated Wind Waves*, pages 155–172. Kluwer Academic, Norwell, Mass., 1989.

[40] R. Romeiser, A. Schmidt, and W. Alpers. A three-scale composite surface model for the ocean wave-radar modulation transfer function. *J. Geophys. Res.*, 99(C5):9785–9801, 1994.

[41] D. P. Kasilingam and O. H. Shemdin. The validity of the composite surface model and its application to the modulation of radar backscatter. *Int. J. Remote Sensing*, 13(11):2079–2104, 1992.

[42] W. C. Keller, W. J. Plant, Jr. R. A. Petitt, and E. A. Terray. Microwave backscatter from the sea: modulation of received power and Doppler bandwidth by long waves. *J. Geophys. Res*, 99(C5):9751–9766, 1994.

[43] G. Soriano, M. Joelson, and M. Sallard. Doppler spectra from a two-dimensional ocean surface at L-band. *IEEE Trans. Geosci. Remote Sens.*, 44(9):2430–2437, 2006.

[44] H. Dankert and W. Rosenthal. Ocean surface determination from X-band radar-image sequences. *J. Geophys. Res.*, 109(C04016):doi:10.1029/2003JC002130, 2004.

[45] J. C. Nieto Borge, G. R. Rodriguez, K. Hessner, and P. I. Gonzalez. Invreswion of marine radar images for surface wave analysis. *J. Atmos. Oceanic Tech.*, 21:1291–1300, 2004.

[46] D. A. Kapp and G. S. Brown. A new numerical method for rough-surface scattering calculations. *IEEE Trans. Antennas Propagat.*, 44(5):711–721, 1996.

[47] H. T. Chou and J. T. Johnson. A novel acceleration algorithm for the computing of scattering from rough surfaces with the forward-backward method. *Radio Sci.*, 33(5):1277–1287, 1998.

[48] K. Iizuka, A. P. Freundorfer, K. H. Wu, H. Mori, H. Ogura, and V. K. Nguyen. Step-frequency radar. *J. Appl. Phys.*, 56(9):2572–2583, 1984.

[49] Leung Tsang, Jin Au Kong, and Kung-Hau Ding. *Scattering of Electromagnetic Waves : Theories and Applications*. Wiley Interscience, New York, 2000.

[50] J. W. Wright. A new model for sea clutter. *IEEE Trans. Antennas Propagat.*, 16(2):217–223, 1968.

[51] G. R. Valenzuela. Theories for the interaction of electromagnetic and oceanic waves - a review. *Boundary Layer Meteorol.*, 13:61–85, 1978.

[52] J. T. Johnson, R. T. Shin, J. A. Kong, L. Tsang, and K. Pak. A numerical study of composite surface model for ocean backscattering. *IEEE Trans. Geosci. Remote Sens.*, 36(1):72–82, 1998.

[53] E. I. Thorsos and D. R. Jackson. The validity of the perturbation approximation for rough surface scattering using a Gaussian roughness spectrum. *J. Acoust. Soc. Am.*, 66(1):261–277, 1989.

[54] H. Kim. *Radar images studies of scattering from random rough surfaces*. PhD thesis, The Ohio State University, 2002.

[55] D. Holliday, Jr. L. L. DeRaad, and G. J. St-Cyr. Forward-backward: a new method for computing low-grazing angle scattering. *IEEE Trans. Antennas Propagat.*, 44(5):722–729, 1996.

[56] Leung Tsang, Jin Au Kong, Kung-Hau Ding, and Chi On Ao. *Scattering of Electromagnetic Waves : Numerical Simulations*. Wiley Interscience, New York, 2001.

[57] H. T. Chou and J. T. Johnson. Formulation of forward-backward method using novel spectral accleration for the modeling of scattering from impedance rough surfaces. *IEEE Trans. Geosci. Remote Sens.*, 38(1):605–607, 2000.

[58] A. Ishimaru and J. S. Chen. Scattering from very rough surfaces based on the modified second-order Kirchhoff approximation with angular and propagation shadowing. *J. Acoust. Soc. Am.*, 88(4):1877–1883, 1990.

[59] E. I. Thorsos. The validity of the kirchhoff approximation for rough surface scattering using a Gaussian roughness spectrum. *J. Acoust. Soc. Am.*, 83(1):78–92, 1988.

[60] G. D. Pan, R. Burkholder, J. T. Johnson, T. Toporkiv, and M. Sletten. Studies of ocean surface retrieval from simulated LGA radar. In *Proceedings of IEEE IGARSS06*, pages 1335–1337, July 31-Aug. 4 2006.

[61] J. V. Toporkov and M. A. Sletten. Numerical study of low grazing range-resolved radar backscatter from the sea surface. *DoD HPC Users Group Conference*, Nashville, TN, June, 2005.

[62] M. S. Longuet-Higgins and R. W. Stewart. Changes in the form of short gravity waves on long waves and tidal currents. *J. Fluid Mech.*, 8:565–583, 1960.

[63] M. S. Longuet-Higgins and R. W. Stewart. The changes in amplitude of short gravity waves on steady non-uniform currents. *J. Fluid Mech.*, 9:529–549, 1961.

[64] J. T. Johnson and Y. Y. Cai. A theoretical study of sea surface up/down wind brightness temperature differences. *IEEE Trans. Geosc. Rem. Sens.*, 40:66–78, 2002.

[65] D. G. Dommermuth and D. K. P. Yue. A high-order specrtal method for the study of nonlinear gravity waves. *J. Fluid Mech.*, 184:267–288, 1987.

[66] M. Tanaka. A method of studying nonlinear random field of surface gravity waves by direct numerical simulation. *Fluid Dynam. Res.*, 28:41–60, 2001.

[67] K. M. Berger, G. R. Baker, and J. T. Johnson. A comparison of non-linear water wave models. *Int. J. Comp. Fluid Dyn.*, 17:219–224, 2003.

[68] D. G. Dommermuth. The initialization of nonlinear waves using an adjustment scheme. *Wave Motion*, 32:307–317, 2000.

[69] G. B. Whitham. A note on group velocity. *J. Fluid Mech.*, 9:347–352, 1960.

[70] F. P. Bretherton and C. J. R. Garrett. Wavetrains in inhomogeneous moving media. *Proc. Roy. Soc. Lond. A*, 302:529–554, 1968.

[71] P. A. Hwang and O. H. Shemdin. Modulation of short waves by surface currents: a numerical solution. *J. Geophys. Res.*, 95 (C9):16,311–16,318, 1990.

[72] W. C. Keller and J. W. Wright. Microwave scattering and the straining of wind-generated waves. *Radio Sci.*, 10:139–147, 1975.

[73] W. J. Plant, W. C. Keller, and J. W. Wright. Modulation of coherent microwave backscatter by shoaling waves. *J. Geophys. Res.*, 83(C3):1347–1352, 1978.

[74] J. W. Wright, W. J. Plant, and W. C. Keller. Ocean wave-radar modulation transfer functions from the West Coast experiment. *J. Geophys. Res.*, 85(C9):4957–4966, 1980.

[75] F. Feindt, J. Schr$\acute{}$oter, and W. Alpers. Measurement of the ocean wave-radar modulation transfer function at 35 GHz from a sea-based platform in the North Sea. *J. Geophys. Res.*, 91(C11):13065–13083, 1986.

[76] D. Hauser and G. Caudal. Combination analysis of the radar cross-section modulation due to the long ocean wave around 14^0 and 34^0 incidence: Implication for the hydrodynamic modulation. *J. Geophys. Res.*, 101(C11):25833–25846, 1996.

[77] G. D. Pan and J. T. Johnson. A numerical study of the modulation of short sea waves by longer waves. *IEEE Trans. Geosci. Remote Sens.*, 44(10):2880–2889, 2006.

[78] J. V. Toporkov, R. T. Marchand, and G. S. Brown. On the discretization of the integral equation describing scattering by rough conducting surfaces. *IEEE Trans. Antennas Propagat.*, 46(1):150–161, 1998.

[79] R. T. Marchand and G. S. Brown. On the use of finite surfaces in the numerical prediction of rough surface scattering. *IEEE Trans. Antennas Propagat.*, 47(4):600–604, 1999.

[80] Leung Tsang and Jin Au Kong. *Scattering of Electromagnetic Waves : Advanced Topics*. Wiley Interscience, New York, 2001.

[81] V. W. Pidgeon. Doppler dependence of radar sea-return. *J. Geophys. Res.*, 73(4):1333–1341, 1968.

[82] G. R. Valenzuela and M. B. Laing. Study of Doppler spectra of radar sea echo. *J. Geophys. Res.*, 75(3):551–563, 1970.

[83] J. W. Wright and W. C. Keller. Doppler spectra in microwave scattering from wind waves. *Phys. Fluids*, 14(3):466–454, Mar. 1971.

[84] D. B. Trizna. A model for Doppler peak spectral shift for low grazing angle sea scatter. *IEEE J. Ocean. Engineer.*, 10(4):368–375, 1985.

[85] T. L. Smith. Doppler spectra of laboratory wind waves at low grazing angle. *Wave Random Media*, 10(1):33–41, 2000.

[86] D. R. Thompson. Calculation of microwave doppler spectra from the ocean surface with a time-dependent composite model. In G. Komen and W. Oost, editors, *Radar Scattering from Modulated Wind Waves*, pages 27–40. Kluwer Academic, Norwell, Mass., 1989.

[87] W. J. Plant and W. C. Keller. Evidence of Bragg scattering in microwave Doppler spectra of sea return. *J. Geophys. Res.*, 95(C9):16299–16310, 1990.

[88] O. M. Phillips. *The Dynamics of the Upper Ocean*. Cambridge University Press, London, second edition edition, 1977.

[89] C. L. Rino and H. D. Ngo. Numerical simulation of low-grazing-angle ocean microwave backscattering and its relation to sea spikes. *IEEE Trans. Antennas Propagat.*, 46(1):133–141, 1998.

[90] W. Choi and D. R. Lyzenga. Surface waves interacting with a slowly varying currents induced by nonlinear internal waves. 2004.

[91] N. E. Huang, D. T. Chen, and C. C. Tung. Interactions between steady non-uniform currents and gravity waves with applications for current measurements. *J. Phys. Oceanogr.*, 2:420–431, 1972.

[92] W. E. Boyce and R. C. DiPrima. *Elementary Differential Equations and Boundary Value Problems*. John Wiley and Sons, Inc, New York, 7th edition edition, 2001.